

AD-A052 883

PRATT AND WHITNEY AIRCRAFT GROUP WEST PALM BEACH FL  
INFLUENCE OF SUBSURFACE DEFECTS ON FATIGUE PROPERTIES OF TITANIUM--ETC(U)

F33615-75-C-5138

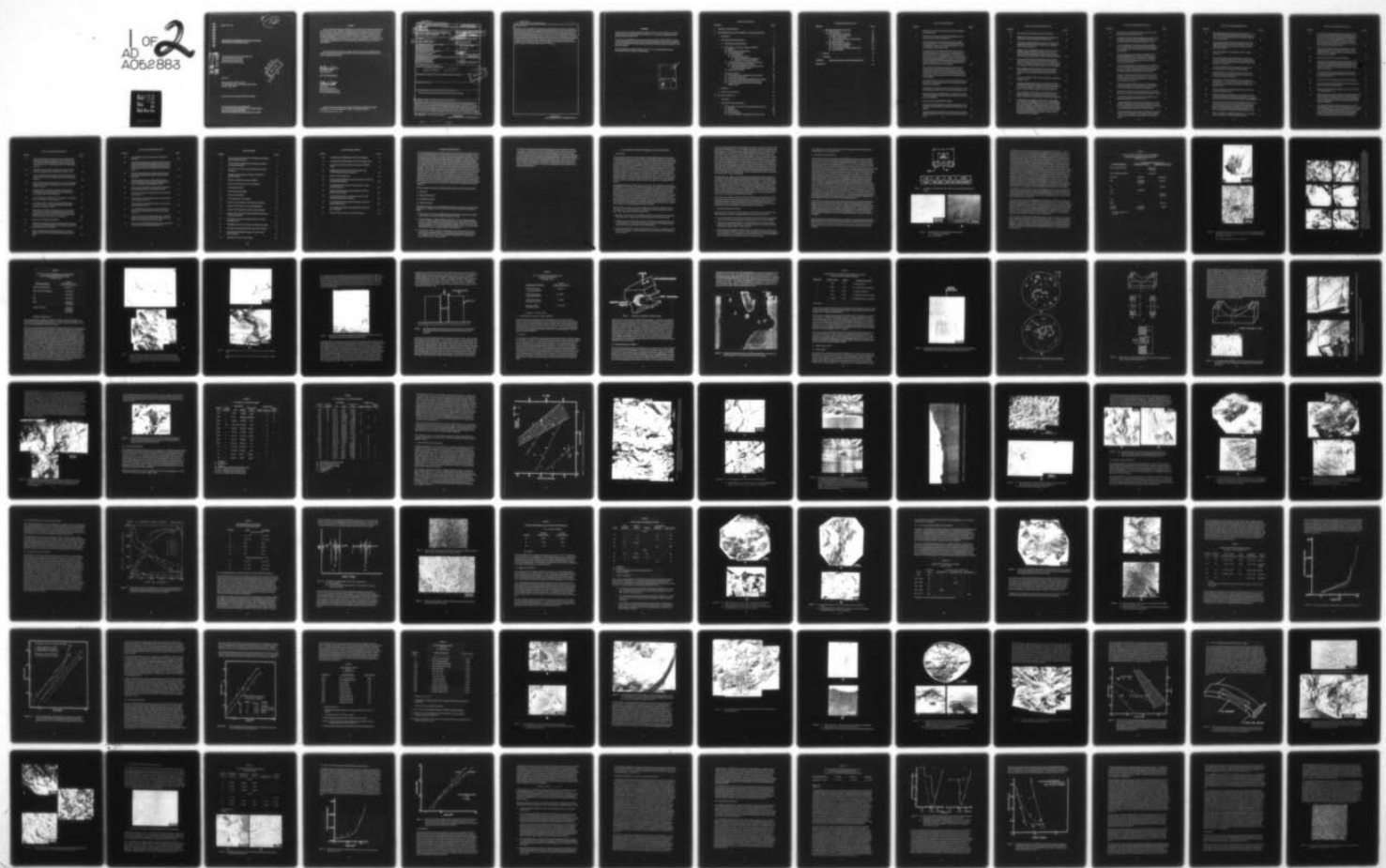
UNCLASSIFIED

PWA-FR-8666

AFML-TR-77-112

NL

1 OF 2  
AD-A052 883



1 OF 2  
AD  
A052883



AD A 052883

AFML-TR-77-112

✓12

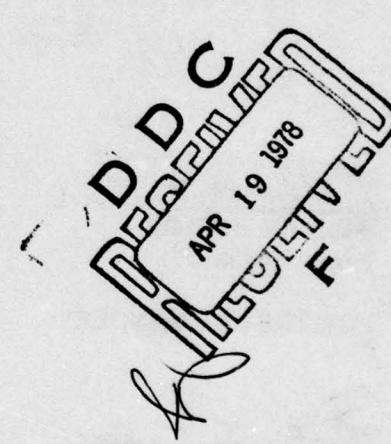
**INFLUENCE OF SUBSURFACE DEFECTS ON FATIGUE  
PROPERTIES OF TITANIUM ALLOYS**

AD No. 1  
DDC FILE COPY

UNITED TECHNOLOGIES CORPORATION  
Pratt & Whitney Aircraft Group  
Government Products Division  
West Palm Beach, Florida 33402

July 1977

Technical Report AFML-TR-77-112  
Final Technical Report for the Period 1 March 1975  
Through 1 March 1977



Approved for public release; distribution unlimited.

AIR FORCE MATERIALS LABORATORY  
AIR FORCE WRIGHT AERONAUTICAL LABORATORIES  
AIR FORCE SYSTEMS COMMAND  
WRIGHT-PATTERSON AIR FORCE BASE, OHIO 45433

## NOTICE

When Government drawings, specifications, or other data are used for any purpose other than in connection with a definitely related government procurement operation, the United States Government thereby incurs no responsibility nor any obligation whatsoever; and the fact that the government may have formulated, furnished, or in any way supplied the said drawings, specifications, or other data, is not to be regarded by implication or otherwise as in any manner licensing the holder or any other person or corporation, or conveying any rights or permission to manufacture, use, or sell any patented invention that may in any way be related thereto.

This report has been reviewed by the Information Office (OI) and is releasable to the National Technical Information Service (NTIS). At NTIS, it will be available to the general public, including foreign nations.

*William R Kerr*  
WILLIAM R. KERR  
Project Engineer

FOR THE COMMANDER

*Nathan G. Tupper*  
NATHAN G. TUPPER  
Acting Chief  
Structural Metals Branch  
Metals and Ceramics Division  
Air Force Materials Laboratory

Copies of this report should not be returned unless return is required by security considerations, contractual obligations, or notice on a specific document.

UNCLASSIFIED

~~SECURITY CLASSIFICATION OF THIS PAGE (When Data Entered)~~

19) REPORT DOCUMENTATION PAGE		READ INSTRUCTIONS BEFORE COMPLETING FORM
1. REPORT NUMBER AFML-TR-77-112	2. GOVT ACCESSION NO.	3. RECIPIENT'S CATALOG NUMBER
4. TITLE INFLUENCE OF SUBSURFACE DEFECTS ON FATIGUE PROPERTIES OF TITANIUM ALLOYS.		5. TYPE OF REPORT & PERIOD COVERED Final March 1975 - 1 March 1977
6. AUTHOR(s) M. J. Blackburn C. C. Law		7. CONTROLLING ORG. REPORT NUMBER PWA-FR-8666
8. PERFORMING ORGANIZATION NAME AND ADDRESS United Technologies Corporation Pratt & Whitney Aircraft Group Government Products Division West Palm Beach, Florida 33402		10. PROGRAM ELEMENT, PROJECT, TASK AREA & WORK UNIT NUMBERS Project 2306/P4
11. CONTROLLING OFFICE NAME AND ADDRESS Air Force Materials Laboratory/LLS Air Force Systems Command Wright-Patterson Air Force Base, Ohio 45433		12. REPORT DATE July 1977
14. MONITORING AGENCY NAME & ADDRESS (if different from Controlling Office) Air Force Plant Representative Office Pratt & Whitney Aircraft Group Government Products Division West Palm Beach, Florida 33402		13. NUMBER OF PAGES 144
16. DISTRIBUTION STATEMENT (of this Report) Approved for public release; distribution unlimited.		15. SECURITY CLASS. (of this report) Unclassified
17. DISTRIBUTION STATEMENT (of the abstract entered in Block 20, if different from Report)		15a. DECLASSIFICATION/DOWNGRADING SCHEDULE <i>D D C APR 19 1978</i>
18. SUPPLEMENTARY NOTES		
19. KEY WORDS (Continue on reverse side if necessary and identify by block number) Titanium Alloys, Fatigue, Defects, Subsurface Cracks, Residue Stress, Surface Finish		
20. ABSTRACT (Continue on reverse side if necessary and identify by block number) A program was conducted to evaluate the influence of two specific defects on the low cycle fatigue properties of selected alpha:beta titanium alloys. The formation of subsurface fatigue cracks and subsequent propagation to produce failure can lead to a characteristic fracture topography which has been designed a 'cleavage rosette'. This type of failure was first recognized in the alloy Ti-6Al-5Zr-0.5Mo-0.25 Si (IMI 685) beta processed to give a coarse acicular structure, in this case a very large fatigue debit is observed. The fatigue properties of IMI 685 determined under a range of stress amplitudes and frequencies are presented together with the results of detailed analysis of the chemistry of crack origins and fracture topography. Experiments to simulate rosette type failures by the introduction of artificial		

**DD FORM 1 JAN 73 1473 EDITION OF 1 NOV 65 IS OBSOLETE**

**UNCLASSIFIED**

**SECURITY CLASSIFICATION OF THIS PAGE (When Data Entered)**

**UNCLASSIFIED**

**SECURITY CLASSIFICATION OF THIS PAGE(When Data Entered)**

**20. Abstract (Cont'd)**

subsurface nucleation sites in IMI 685 and other alloys are described. Although some features of a rosette fracture could be reproduced, the magnitude of the fatigue debit was not. Models to account for the kinetic features of cracking in IMI 685 are proposed and compared with the experimental results. The second type of defect studied was a local structural heterogeneity, known as "beta fleck", that can occur in incorrectly processed alpha:beta titanium alloys. The periodic chemical fluctuation responsible for regions of beta structure in an alpha:beta processed Ti-6Al-4V alloy are documented. Fatigue testing, under both stress and strain control, have established that property-debits associated with beta flecks are only observed in specimens with surface residual stresses. The magnitude of this debit is dependent upon the specific test conditions. Differences in behavior between flecked and normal alpha:beta material are traced to the stability of surface stresses during cycling, stresses declining more rapidly in the flecked material. Explanations for these differences are presented and discussed.



**UNCLASSIFIED**

**SECURITY CLASSIFICATION OF THIS PAGE(When Data Entered)**

## FOREWORD

This final report covers work performed on Contract F33615-75-C-5138 Project No. 3306/P4, in the period from 1st March 1975 to 1st February 1977. This report was submitted by the authors for approval in May 1976.

The work was accomplished by the Commercial Products Division of Pratt & Whitney Aircraft Group, East Hartford, Connecticut under the technical direction of Mr. W. R. Kerr (AFML/LLS) of the Air Force Materials Laboratory, Metals and Ceramics Division, Wright Patterson Air Force Base, Ohio, 45443.

Dr. M. J. Blackburn was Program Manager and Dr. C. C. Law, the Responsible Engineer. The assistance of Mr. F. Nardozzi is acknowledged.

ACCESSION for	
NTIS	<input checked="" type="checkbox"/> Section
DDC	<input type="checkbox"/> Section
MANUFACTURER	<input type="checkbox"/>
ISI	<input type="checkbox"/>
PM	
DISTRIBUTION/AVAILABILITY CODES	
A1	SPECIAL

## TABLE OF CONTENTS

SECTION	PAGE
<b>I. GENERAL INTRODUCTION</b>	<b>1</b>
<b>II. THE SUBSURFACE DEFECT PROBLEM - CLEAVAGE ROSETTES</b>	<b>3</b>
1. Introduction	3
2. Experimental Methods and Results	4
a. Initial Studies of Seeded Defects	5
b. Characterization, Testing and Analysis of IMI 685	16
(1) Material	16
(2) NDI Characterization of Defects	17
(3) Fatigue Testing at 70°F	19
(a) Radial Direction	19
(b) Circumferential Direction	26
1) Rosette Failures (Defective Material)	29
2) Fractures in Defect-Free Material	36
(4) Chemical Measurements of a Rosette Defect Origin	39
(a) Secondary ion Microprobe Results	39
(b) Optical Metallography, Auger Spectroscopy and Electron Microprobe Analysis	41
(5) Fatigue Testing at 400°F	44
c. Ancillary Experiments	45
(1) Crack Nucleation and Propagation Rates in IMI 685	48
(2) Seeded Defects in IMI 685	54
(3) A Defect-Containing Specimen Machined from a Forging	65
(4) Dwell Debits in Other Alpha:Beta Titanium Alloys	68
(5) Crack Growth Measurements in Other Alpha:Beta Titanium Alloys	70
3. Discussion	71
4. Summary and Conclusions	84
<b>III. BETA-FLECK DEFECTS</b>	<b>87</b>
1. Introduction	87
2. Experimental Methods and Results	88
a. Characterization of Ti-6Al-4V Containing Beta-Fleck Defects	88
(1) Materials	88
(2) Microstructure	88
(3) Chemical Analysis	93
(4) Thermomechanical Processing/Heat Treatment Studies	94

## TABLE OF CONTENTS (Cont'd)

SECTION	PAGE
b. Mechanical Properties Characterization	99
(1) Tensile Properties	99
(2) Strain-Controlled LCF Properties	101
(a) Effect of Surface Preparation	102
(b) Effect of Strain Range	104
(c) Cyclic Relaxation of Surface Residual Stress	106
(d) Crack Nucleation	109
(3) Stress-Controlled LCF Properties	111
(a) Effect of Surface Preparation	111
(b) Effect of Stress Amplitude	113
(c) Cyclic Relaxation of Surface Residual Stress	113
(d) Crack Nucleation	118
3. Discussion	120
4. Conclusions	127
<b>APPENDIX</b>	<b>SURFACE RESIDUAL STRESS DETERMINATION</b>
<b>REFERENCES</b>	<b>128</b>
	129

## LIST OF ILLUSTRATIONS

FIGURE		PAGE
1	Dimension of LCF specimens fabricated from the second IMI 685 forging section.	6
2	Microstructures of the seeded Ti-6Al-4V specimens (a) in the first and second sets, (b) in the third set.	6
3	(a) General appearance of the fracture surface of a hydride-seeded specimen (No. 16). Note the circumferential shear lip. The subsurface nucleation site could not be located. (b) Typical topography of the fracture surface.	9
4	Scanning electron micrographs of the fracture surface of the Ti-6Al-4V specimen No. 10 (pore only). The microstructure is given in Figure 2(a). (a) General appearance of the entire fracture surface. Note the circumferential shear lip and the five subsurface nucleation sites facets B, D, E, F and G. Facet B is shown in greater detail in (b), while the typical striation observed at its periphery is illustrated in (c). The striations observed at the periphery of facet D is shown in (d), (e) and (f).	10
5	Scanning electron fractographs of hydride-seeded Ti-6Al-4V with acicular microstructure shown in Figure 2(b). (a) Subsurface fracture initiated at the seeded pore (partially exposed) indicated by an arrow. (b) Fracture initiated at the seeded pore near the surface. Striations observed on facets A and B are illustrated in Figure 6.	12
6	(a) Striations observed on facet A of the fracture surface shown in Figure 5(a). (b) Striations observed on facet B of the fracture surface shown in Figure 5(b).	13
7	Appearance of the region adjacent to the NaCl-seeded pore. Note the reacted layer around the tip of the pore (hardness indentation).	14
8	Experimental setup for trapping argon in a pore between two rods which were subsequently diffusion bonded together and machined into a LCF specimen.	15
9	Schematic of the machined IMI 685 forging.	17
10	Ultrasonic C-span recording from an IMI 685 forging section. The probe was oriented parallel to the circumferential direction of the forging.	18
11	Microstructure and cracks observed at the defect-prone area of the IMI 685 forging which had 62 stress cycles before retirement from service.	20

LIST OF ILLUSTRATIONS (CONT'D)

FIGURE		PAGE
12	X-ray pole figures (a) (0002) pole and (b) (1010) pole.	21
13	Dimensions of (a) three-point bend specimen (b) tension LCF specimen No. 2 and (c) tension LCF specimen No. 4	22
14	(a) Schematic diagram showing the locations of cracking in the IMI 685 bend specimen after LCF testing and (b) appearance of the fracture at location A.	23
15	Scanning electron micrographs showing the appearance of the subsurface crack nucleation site indicated in Figure 14b (a) shows the cliff-like topography and fatigue striations around the nucleation site, (b) shows the nucleation site in greater detail.	24
16	Scanning electron micrographs illustrating the general appearance of the fracture surface in the IMI 685 LCF tension specimen No. 2. Striations on regions C and E can be traced to an origin at region D. Arrows indicate directions of crack propagation.	25
17	Fatigue striations observed on facet E of the fracture surface shown in Figure 16. Note the gradual decrease in striation spacing as the crack propagated across this facet from left to right.	26
18	S-N curves of IMI 685 at 70°F, the sources of data are indicated in Tables 5 and 6.	30
19	Scanning electron fractograph of the rosette-fracture observed on IMI 685 specimen No. 4. Details of the 'fish eye' fracture origin are shown in Figure 20. Striations have been observed on facets A, B and C. Those on Facet A are shown in Figure 23.	31
20	(a) The topography of the 'fish eye' crack nucleation site. (b) Detailed appearance of the central pore and its surrounding. Note the presence of the "brittle-type" striations on the 'fish eye'.	32
21	Scanning electron micrographs of the 'fish eye' fracture origin in specimen No. 4 illustrating the origin of the "brittle-type striation". (a) Showing the "brittle-type" striations on the 'fish eye' and the microstructure of a longitudinal section near the central pore and (b) longitudinal section closer to the central pore, etched to reveal the microstructure on the fracture surface. A comparison of (a) and (b) shows that the striations are located at the interfaces between the platelets.	33

## LIST OF ILLUSTRATIONS (CONT'D)

FIGURE		PAGE
22	Microstructure at a longitudinal section through the central pore (location indicated by the arrow).	34
23	(a) Replica showing fine fatigue striations between facet A and the 'fish eye' on the fracture surface illustrated in Figure 19, (b) SEM micrograph showing fatigue striations on facet A.	35
24	(a) General appearance of the fracture surface of specimen No. 25. (b) The fracture origin which is located between the two fanshaped facets, showing the small pore and the brittle-type striations.	36
25	(a) General appearance of the fracture of specimen No. 47. The fatigue origin consists of a facet located at the edge of a step on the fracture surface. (b) Details of the fatigue origin. Small central pores characteristic of the rosette-type fracture were not observed.	37
26	(a) The general appearance of the fracture surface of specimen No. 45. The surface crack origin is indicated by an arrow. Note the absence of large cleavage-like facets at the fracture origin. (b) Fatigue striations observed near the fracture origin.	38
27	Change in intensities of several elements as a function of sputtering time. Determination of compositions at the 'fish eye' fracture origin and the bulk commenced after steady levels of major elements were observed.	40
28	Auger electron spectrographs at the 'fish eye' fatigue origin. (a) before sputtering. (b) after sputtering, note the decrease in C, O and S which are common surface contaminants.	42
29	Microstructure near the expected rosette defect site in an IMI 685 specimen which had been isothermally compressed at 1830°F.	43
30	The microstructure shown in Figure 29 after additional recrystallization treatment at 1830°F for 1 hour.	43
31	(a) General appearance of the fracture of specimen No. 9 tested at 400°F. The apparent fracture origin is indicated by an arrow. (b) A longitudinal section along the line indicated in (a), showing the prior beta grain size adjacent to the fracture surface.	46
32	(a) General appearance of the fracture of specimen No. 44 tested at 400°F. (b) A longitudinal section along the line indicated in (a), showing the prior beta grain size adjacent to the fracture surface.	47

LIST OF ILLUSTRATIONS (CONT'D)

FIGURE		PAGE
33	The general appearance of the fracture of specimen No. 9. The stress had been incrementally increased four times before fracture. No crack-front marking due to the uploading is apparent on the fracture surface.	49
34	(a) General appearance of the fracture near the rosette crack origin observed in specimen No. 20. (b) Details of the rosette crack origin showing the characteristic central pore and the brittle-type striations.	50
35	Surface crack length, $2a$ versus number of cycles for specimen No. 45.	52
36	(a) Crack propagation results as determined by measurement of a surface crack on a smooth ( $K_t=1$ ) LCF specimen (curve D) compared with those determined from fracture mechanics specimens (curve A, B and C).	53
36	(b) Crack propagation results as determined by fatigue striation measurement on smooth ( $K_t=1$ ) LCF specimens.	55
37	(a) Microstructure of the second and third sets of specimens. (b) Microstructure of the third set of specimens after a slower cool from the solution temperature.	58
38	The appearance of the fracture surface of the nitrided-seeded specimen No. 41. The microstructure is given in Figure 37a. Fracture initiated at the seeded pore which can be located at the upper left corner.	59
39	Fracture appearance of the dwell-tested specimen (#38) which contains a nitride-seeded pore.	60
40	(a) Microstructure of a longitudinal section through the nitride-seeded pore (indicated by an arrow) in specimen No. 38. (b) Microstructure of the nitride-seeded pore shown in higher magnification.	61
41	(a) General fracture appearance of the dwell-tested specimen (No. 31) which contains a clean pore. The pore (indicated by the upper arrow) is partially exposed and is located at the overload failed region. (b) The clean pore shown in higher magnification. (c) The fracture origin which is indicated by the lower arrow in (a).	62
42	Fracture appearance of the high frequency-tested (12 cpm) specimen (No. 39) which contained a nitride-seeded pore.	63

LIST OF ILLUSTRATIONS (CONT'D)

FIGURE		PAGE
43	The LCF lives of seeded IMI 685 specimens relative to those of the dwell-tested (12 cph) specimens containing rosette defects (curve A) and defect-free specimens (curve B); those of the defect-free or rosette-containing specimens tested at 12 cpm are given by the scatterband D. The data points from specimens seeded with hydride are indicated by H and those from specimens seeded with nitride by N.	64
44	The shape and relative orientation of the fatigue specimen machined from the Ti-6Al-2Sn-4Zr-2Mo flat disk. A defect had been located at the gage section of the specimen by the ultrasonic C-scan technique.	65
45	Microstructure of the Ti-6Al-2Sn-4Zr-2Mo disk.	66
46	Scanning electron micrograph of the fracture surface around the fatigue crack origin in the specimen machined from a defective Ti-6Al-2Sn-4Zr-2Mo flat disk (see Figure 44). The nucleation site which is shown in greater detail in Figure 47(a) indicated by an arrow.	66
47	(a) Details of the crack nucleation site shown in Figure 46. Typical appearance of fatigue striations on fracture surfaces are shown in (b) and (c).	67
48	Microstructure of the beta-heat treated Ti-6Al-2Sn-4Zr-2Mo.	68
49	Microstructure of Ti-11 (a) shows the large prior beta grains and (b) shows the spheroidized beta phase.	69
50	Surface crack length, $2a$ versus number of cycles for Ti-6Al-2Sn-4 Zr-2Mo specimen No. 10.	70
51	Results of surface crack measurements on beta-heat treated Ti-6Al-2Sn-4Zr-2Mo and STA treated Ti-6Al-4V LCF test specimens plotted in terms of $da/dn$ versus $\Delta K$ . The fatigue crack propagation rates determined from fracture mechanics specimens are indicated by solid lines.	71
52	(a) Crack growth behavior inferred from striation observation on IMI 685 Specimen No. 2 (Curve 2E) and Specimen No. 4 (Curve 4E). (b) Idealized representations of results shown in (a). Curve AE represents an initially constant rate of crack propagation until a more rapid crack mode (Curve E) becomes available. Curve B represents an average of Curves 2E and 4E in (a).	76

LIST OF ILLUSTRATIONS (CONT'D)

FIGURE	PAGE	
53	Calculated fracture lives as function of the maximum stresses assuming an initial penny-shaped flaw of 0.03" diameter. Curves A and B are obtained, respectively, from Curves AE and BE shown in Figure 52b. A combination of Curves A and B results in Curve C.	77
54	Formation of a shear crack in a beta-colony structure. (Taken from the unpublished work of Roberson, et al, ARL, 1972).	80
55	The macrostructure and microstructure of the longitudinal mid-section of the Ti-6Al-4V bar (TMCA material) in the as-received condition.	89
56	The macrostructure and microstructure of the Ti-6Al-4V forging (P&WA material) after a heat treatment of 1750°F/1 hour AC + 1300°F/2 hours AC.	90
57	Scanning electron micrographs showing the morphologies of the beta-phase in the center of the Ti-6Al-4V bar at (a) a beta-fleck location and (b) a normal location.	95
58	(a) 51 V image of a normal area, (b) 51 V image of a beta-flecked area (c) 56 Fe image of a beta-flecked area.	97
59	The microstructure of a center specimen isothermally forged at 1675°F to a strain of 130%. (a) before and (b) after heat treatment for one hour at 1780°F.	99
60	Orientations of the half bolt hole specimens (a) and tensile and LCF specimens (c) relative to the transverse slices cut from the longitudinal halves of a Ti-6Al-4V bar. The dimensions of these specimens are given in (b), (d) and (e), respectively.	100
61	Dimensions of the MiniKrouse specimen.	102
62	Fatigue crack initiation lives of normal and beta-flecked Ti-6Al-4V as a function of surface preparation. The specimens were tested in strain-controlled LCF at 0.9% strain.	105
63	Surface residual stresses at various distances from the fracture surfaces of half bolt hole specimens with and without beta-fleck defects.	107

## LIST OF ILLUSTRATIONS (CONT'D)

FIGURE		PAGE
64	Cyclic relaxation of surface residual stress in MiniKrouse specimens.	109
65	Photomicrographs taken from a replica showing the crack nucleation sites in half bolt hole specimens, (a) at the interface between the acicular alpha and the aged martensite and (b) at the interface between the primary alpha and the aged martensite.	110
66	Photomicrographs taken from a replica showing a crack nucleated in a normal region rather than at the adjacent beta-fleck defect.	110
67	Photomicrograph taken from a replica showing crack nucleation at slip bands normal to the acicular alpha phase, at a prior beta boundary and at alpha-beta interfaces.	111
68	Effect of surface preparation on fracture life of normal and beta-flecked specimens in stress-controlled LCF tests.	112
69	S-N Curves for normal and beta-flecked specimens with stress-relieved surfaces.	113
70	Cyclic relaxation of surface residual stress in normal and beta-flecked specimens at $R = -0.6$ .	115
71	Cyclic relaxation of surface residual stress in normal and beta-flecked specimens at $R = 0.1$ .	116
72	X-ray diffraction peak profiles of (a) beta-flecked specimen (b) normal specimen after various numbers of stress cycles at $R = -0.6$ .	117
73	Crack nucleation site in a beta-flecked specimen. (a) general appearance of the fracture surface, arrow indicates the crack origin. (b) microstructure at the fracture origin.	119
74	S-N Curves of (a) alpha-beta finish forged, (b) beta finish forged Ti-6Al-4V with various surface finishes (Ref. 28).	124

## LIST OF TABLES

TABLE		PAGE
1	70°F LCF Lives of Seeded Ti-6Al-4V Specimens with Alpha: Beta Forged Microstructure	8
2	70° LCF Lives of Seeded Ti-6Al-4V Specimens with Beta-Annealed Microstructure	11
3	70° LCF Lives of Ti-6Al-2Sn-4Zr-2Mo Specimens Seeded with Argon	16
4	Ultrasonic C-Scan Results on a Section of the IMI 685 Machined Forging	19
5	Results of 70°F Dwell LCF Tests of IMI 685	27
6	Results of 70°F Nondwell LCF Tests of IMI 685	28
7	Ion Microprobe Results	41
8	Electron Microprobe Results	44
9	400°F LCF Test Results	45
10	70°F Uploading LCF Test Results	48
11	Results of Crack Nucleation and Propagation in IMI 685	51
12	Results of 70°F Dwell LCF Tests of Seeded IMI 685	56
13	Results of 70°F Nondwell LCF Tests of Seeded IMI 685	57
14	Results of LCF Tests of Ti-6Al-2Sn-4Zr-2Mo with Beta Heat Treated Microstructure	69
15	Calculated Fracture Lives of IMI 685 Using Various Crack Propagation Laws	75
16	Metallurgical Parameters in the Ti-6Al-4V Billet and Forging	91
17	Quantitative Metallographic Results of the Ti-6Al-4V Billet	92
18	Quantitative Metallographic Results at the Center of the Ti-6Al-4V Billet	92
19	Microhardness of the Ti-6Al-4V Billet	92

### LIST OF TABLES (CONT'D)

TABLE		PAGE
20	Composition of the Alpha Phase in the Ti-6Al-4V Billet	93
21	Composition of the Beta Phase in the Ti-6Al-4V Billet Center	96
22	Secondary Ion Microprobe Results on the Ti-6Al-4V Billet Center	96
23	Metallurgical Parameters of the Ti-6Al-4V Billet Center After One Hour at Various Temperatures	98
24	Results of 70°F Tensile Tests	101
25	Effect of Surface Preparation on Crack Nucleation in Ti-6Al-4V Half Bolt Hole Specimens	103
26	Crack Initiation Life in Beta Heat Treated Ti-6Al-4V Half Bolt Hole Specimens	104
27	Effects of Strain Range on Crack Nucleation in Ti-6Al-4V Half Bolt Hole Specimens	106
28	Surface Residual Stresses in As-Machined Ti-6Al-4V Half Bolt Hole Specimens After Fracture	107
29	Cyclic Relaxation of Surface Residual Stresses in Ti-6Al-4V Mini-Krouse Specimens	108
30	Cyclic Relaxation of Surface Residual Stresses in Ti-6Al-4V $K_t = 1$ Specimens	114
31	Results of 70°F LCF Tests of Ti-6Al-4V Specimens	118

## I. GENERAL INTRODUCTION

Few manufacturing processes are perfect and errors, minor changes in a processing cycle, etc., can lead to defective regions in a product which may influence service performance. Such defects can take many forms, for example: voids, chemical segregation, inclusions, etc., and can influence both mechanical and physical properties. However, it is clear that one of the main problems encountered in service have been in the degradation of fatigue properties. Over the past decades the demands of high technology areas such as the aerospace industry have required that such defects be eliminated from components and the advances in process and quality control, NDI, etc., have proved in general very successful in improving product integrity. Titanium alloys have formed part of such programs and the service record of these materials has been excellent indicating that the techniques for excluding defects has been, on the whole, very successful. However, occasional problems have been encountered especially when the defects occur on a small scale and are difficult to detect by NDI techniques. It would be fair to state that solutions to such problems have been found relatively soon after identification but the reasons behind the modification of properties produced by such defects are less well understood. Description of the types of defects that have been encountered is given below. This has been used to establish an experimental and analytical program designed to gain insight into the nature and effect of two specific defects on subsequent mechanical properties.

The type of defects encountered in titanium alloys depends on several factors including:

- 1) Alloy Type
- 2) Melting/Casting Process
- 3) Fabrication Techniques
- 4) Joining Techniques

If discussion is restricted to wrought, alpha:beta type alloys, the types of defects (other than obvious cracks, forging laps, etc.) that have been found in such products can be listed as follows:

- 1) Clean porosity or voids not associated with alloy segregation but resulting from solidification defects and incomplete healing during ingot conversion.
- 2) Chemical segregation of alpha stabilizing elements (Al, O) or beta stabilizing elements Fe, Mo, V). These segregates may contain a void and, due to the reactivity of titanium, almost always have a reacted layer surrounding the segregate. Other less common types of alloy segregation are: (a) contaminated sponge inclusions carried over from the initial ingot stage and (b) other metallic inclusions of tramp elements.
- 3) A third type of "defect" has also been detected in recent years which also has a pronounced effect on fatigue properties. This microstructural anomaly consists of elongated "spaghetti" alpha, which is not associated with segregation but is attributed to poor control of ingot conversion practice.

The detection of these defects is strongly dependent upon size and distribution position in the product. Ultrasonic inspection, blue etch anodize, eddy current and macroetching are capable of detecting defects if they are sufficiently large and, for some techniques, occur on the surface (which is usually the location of fatigue crack nucleation). Obviously, the most dangerous forms of defects are small subsurface defects, a type dramatically highlighted by recent experience in beta processed IMI 685 fan disks. A second type of defect that has caused concern is the local chemical and microstructural defect known as beta-fleck. The present investigation was undertaken to obtain insight into the nature and effects of these two types of defects. The report of the findings of these studies will be divided into separate sections.

## II. THE SUBSURFACE DEFECT PROBLEM - CLEAVAGE ROSETTES

### 1. Introduction

Several examples of premature fatigue failures in wrought titanium alloys have been traced to small subsurface initiation sites. The details of these initiation regions seem to depend upon the alloy and also the processing cycle. However, in all cases the growth of cracks into the surrounding material has led to a reduction in fatigue life. The best documented example of this type of behavior is in the alloy IMI 685 (Ti-6Al-5Zr-0.5Mo-0.25Si) worked and heat treated to a coarse acicular structure.<sup>(1)</sup> Subsequent fatigue cycling of this material under a square wave cycle with hold times under load of several minutes duration led to very rapid initiation and growth of cracks. The fracture surfaces of the fatigue failures were complex but usually contained a very small pore at the origin and a large area of cleavage-like failure around this origin. It was this cleavage area that gave rise to the term "cleavage rosette". A relatively well defined ring often surrounds the pore and the term "fish-eye" is often used to describe this feature. It is obvious that if such rapid crack extension from a very small pore occurs to a crack size measured in tenths of an inch, it can lead to a very dangerous service situation.

An apparently similar type of failure has been observed in a part manufactured from Ti-6Al-2Sn-4Zr-2Mo.<sup>(2)</sup> In this case, the material was processed in the alpha-beta phase field which resulted in an equiaxed microstructure. The central defect was found to be a pore, in this case considerably larger than those typically observed in the IMI 685 example cited above, again the central flaw was surrounded by a well marked but smaller cleavage area. This in turn is bounded by an area of normal fatigue with the characteristic striated structure. Again by counting these striations and comparing with the total cycles, the conclusion is reached that the cleavage rosette forms rapidly in relatively few cycles. Although a fatigue debit was associated with the defect it was of a much smaller magnitude than the IMI 685 case. Several other examples of morphologically similar failures relating to embedded flaws have occurred, in many cases from contaminated regions within the material.

These and other observations were used to formulate an experimental program to evaluate in detail the effect of various parameters on fatigue life and resultant fatigue fracture features. Three basic premises behind the program were:

- 1) Subsurface "cleavage rosette" type failures could occur in all alpha:beta alloys, independent of structure. A fatigue debit was always associated with a subsurface origin.
- 2) In most (or all) cases contamination of the crack origin site was responsible for the ease of crack nucleation. As in several cases little or no evidence of such damaging contaminants had been found, these effects were considered subtle.
- 3) Although rapid nucleation could occur a second major anomaly was considered to be the rate of crack progression. This also appeared to be more rapid than could be predicted from known rates.

It now seems clear that the first two hypotheses are not correct. Recently it has been established that subsurface initiation can occur in alpha:beta titanium alloys with no apparent structural anomalies. (3, 4) Such failures also exhibit a cleavage-like facet at the origin with much of the failure surface taken up in "normal" fatigue before overload fracture occurs. This type of failure has been observed predominantly in high life ( $N_f \sim 10^5$  cycles) specimens, and does not seem to be associated with any fatigue debit. In other words, the lives of specimens showing subsurface nucleation are equal to those in which initiation occurs on the surface. There is a strong indication that the care exercised in the test set-up strongly influences the location of the fatigue origin, very carefully aligned specimens tend to show subsurface nucleation. The second point has been disproved as a result of investigations on IMI 685 by Eylon and Hall (5) who identified a reduction of fatigue life under square wave or dwell test conditions. This dwell debit is clearly not associated with material defects such as flaws or holes although it seems most unlikely that any compositional abnormalities can contribute to it as it appears to be a general effect. (Thus if compositional effects were responsible they should be detectable in bulk analyses).

We shall examine the validity of the third hypothesis in subsequent sections of this report. It will suffice to note at this stage that cleavage appearing failures are often observed in titanium alloys and it is also assumed that such fracture occurs rapidly. A cleavage appearance may or may not be associated with an abnormal failure nor indicate very rapid crack progression. For example, Yuen et.al (6) have carefully documented failure surfaces observed on crack growth specimens of Ti-6Al-4V. It was shown that cleavage failures occurred at  $\Delta K$  levels  $< 12$  ksi $\sqrt{\text{in}}$  independent of R level. Blackburn et.al (7) shows that cleavage failures can occur under stress corrosion conditions at rates between  $10^{-7}$  and  $10^1$  in/sec. The basic points are that cleavage failures need not indicate any distress nor that rapid separation has occurred. This is not the case for IMI 685 as we shall see.

This program was undertaken to study the effect of contaminated subsurface flaws on LCF behavior of alpha:beta and wear-alpha titanium alloys. Concurrently the LCF behavior and fractographic features of specimens machined from a defective IMI 685 forging were examined in some detail. Hopefully, the results of these two studies would converge and provide insight into the basic mechanism of cleavage rosette type of fracture.

## 2. Experimental Methods and Results

The basic plan at the inception of this program was to conduct a three-part experiment and analytical program. These three program segments can be summarized as follows:

- 1) Construct defects in selected alpha:beta titanium alloys seeded with various contaminants and conduct a fatigue screening program to determine effects on cyclic life capability.
- 2) Expand on the then available data base of the alloy IMI 685 with reference to fatigue properties and fracture characteristics. One critical experiment was to isolate and chemically analyze a fatigue origin in a rosette fracture.
- 3) By analyzing and comparing the results obtained, in the first two parts of the study, definitive experiments would be designed to provide insight into the kinetics and mechanisms of the fatigue processes. Emphasis was to be placed on IMI 685 but the behavior pattern was to be related to the more general framework of alpha:beta alloys.

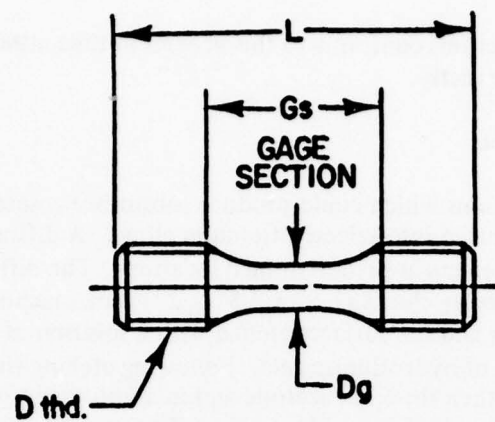
The arrangement of subsequent sections conforms to this general outline although the proposed sequence was not followed exactly.

#### A. Initial Studies of Seeded Defects

In an attempt to synthesize conditions which could produce subsurface rosette-type failures various seeded defects were introduced into selected titanium alloys. A diffusion bonding technique was used to introduce defects at predetermined locations. The diffusion bonding procedure was as follows. Rectangular blocks (1.5" x 2.3" x 3") were machined to a surface finish of better than 8 microinches and the surfaces etched with a solution of 50 ml of lactic acid, 30 ml of nitric acid and 2 ml of hydrofluoric acid. Following etching the blocks were cleaned ultrasonically in trichlorethylene, then rinsed in acetone and in absolute methanol and dried with a spray of freon. Pyramid-shaped hardness indentations of various sizes (simulated pores) were introduced into one of the cleaned surfaces in a regular grid pattern. To simulate contaminated pores, powder particles of various chemicals were carefully seeded into selected hardness indentations. The two blocks were then diffusion bonded together at an elevated temperature under a vacuum of  $10^{-5}$  torr. After diffusion bonding, specimens of the type shown in Figure 1 were machined from the bonded block such that gage sections included one of the defects. (Specimens fabricated from the same bonded block will be referred to as a set.) To reduce the probability of surface crack initiation during LCF testing, approximately 0.003" was removed from the gage section of specimens by electropolishing and followed by vapor blasting. The latter process introduces a small compressive residual stress on the surface by impingement of a jet of high velocity alumina-water slurry. Several bonding conditions were used, depending on the materials selected for study. The specimen preparation techniques described above were initially developed for Ti-6Al-4V. The specific bonding conditions and the LCF results are presented below. Subsequently the same method was used to fabricate IMI 685 specimens the results of these tests are given in Section II.2c(2).

The Ti-6Al-4V alloy used in this study was obtained in the form of an alpha:beta processed forging. Two sets of specimens were produced. One set with an indentation size of 0.01" diagonal and the second set with a size of 0.03" diagonal. Contaminants introduced into the cavities were  $TiO_2$ , TiN,  $Ti_3Al$ , Al,  $MgCl_2$  and hydrided Ti-6Al-4V. These additions were selected as being typical contaminants that could be introduced into titanium alloys during the melting and processing cycle. The diffusion bonding cycle was 1750°F at 500 psi for four hours, these conditions retained the equiaxed alpha:beta grain configuration present in the forging.

The microstructure of bonded material is shown in Figure 2a. Specimens sectioned from the diffusion bonded blocks were tested at room temperature in air under a cyclic stress of 0-120 ksi at a frequency of 1 cycle/minute (square wave). To provide a baseline, specimens fabricated from the forging were given an equivalent thermal cycle and tested under equivalent conditions.



L ref.	Gs	Dg	D thd.
2.000	.960-.980	.249-.251	.500-20UNJF

Figure 1 Dimension of LCF Specimens Fabricated from the Second IMI 685 forging Section

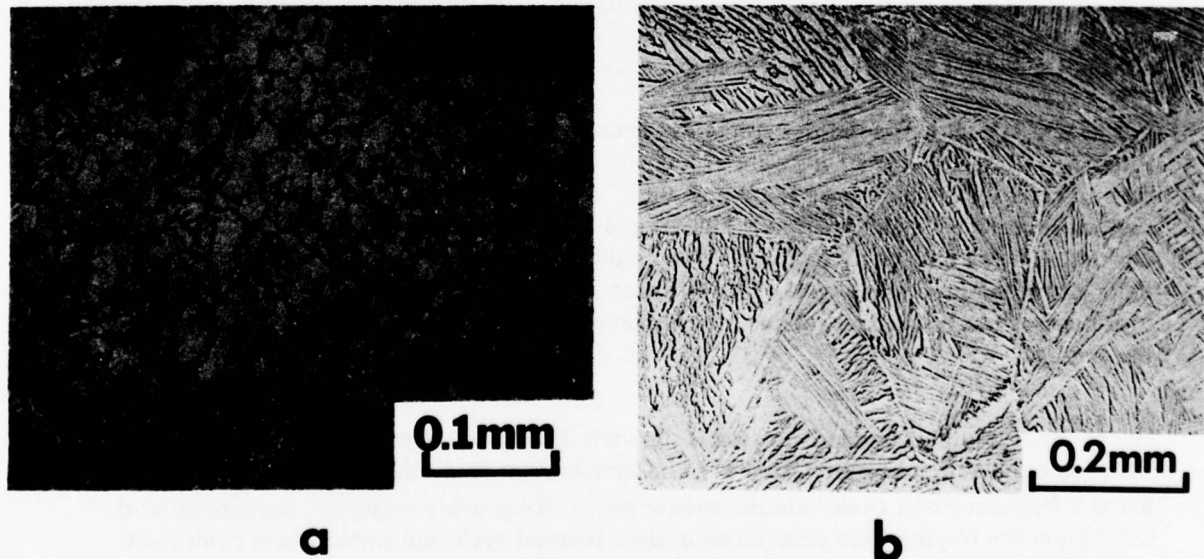


Figure 2 Microstructures of the Seeded Ti-6Al-4V Specimens  
 (a) in the first and second sets  
 (b) in the third set

The fatigue test results for the first two sets of specimens are listed in Table 1. It can be seen that for the first set of specimens neither the clean 0.010" indentation nor the contaminated indentations had any influence on fatigue life. For the second set, the size of the hardness indentation was increased to 0.03" diagonal, the effects of contaminants are much more obvious. Specimens containing seeded contaminants had considerably shorter LCF lives than those without. The most potent contaminant used appears to be the Ti-6Al-4V hydride, with chloride and nitride inclusions showing about a factor of ten reduction in life compared with the baseline specimen. Macroscopically, the fracture surfaces of the majority of the Ti-6Al-4V specimens in the first two sets are highly irregular, indicating that failure did not occur across the diffusion bond interface. In most cases, a continuous shear lip could be found around the specimen indicating subsurface crack nucleation. Partly because of the irregularities of the fracture surface, the hardness indentations were located in only 25% of the specimens tested. In cases where relatively large debits are observed, e.g., specimens # 15 and 16, the fracture appearance seems to indicate a general embrittlement which may have contributed to the difficulty in locating the fracture origin. The fracture surface of the hydride-containing specimen (#16) is shown in Figure 3 and appears more typical of an overload failure than fatigue. A remarkable fracture was observed in specimen #10 which contained a clean pore and exhibited the longest fatigue life. Cracks nucleated at subsurface origins and propagated at apparently the same average rate which resulted in the formation of five equi-diameter facets, labelled B to G in Figure 4.

The seeded pore is located at the center of facet B (Figure 4b). As shown in Figure 4b the major portion of the fatigue surface had a cleavage-like appearance. Striations, which only occurred infrequently, tended to be very fine and ill-defined (Figure 4c to f). The fracture surface appearance of this specimen was duplicated in all others with the exception of the very low life specimens noted above.

The third set of specimens were diffusion-bonded at 1650°F under 800 psi for 4 hours followed by a beta heat treatment of 2000°F for 1 hour and furnace cool. A slightly different diffusion bonding condition was used in this set in an attempt to reduce the amount of plastic distortion of the blocks during bonding. The indentation size for this set of specimens was selected as 0.03" based on the results obtained from the first two specimen sets. The microstructure of the material after the diffusion bonding and heat treatment cycle is shown in Figure 2b. As the lives exhibited by the first two sets were relatively low the fatigue test conditions were changed to 0-110 Ksi, 1 cpm for the third set.

The LCF results of the third set of specimens are given in Table 2, from which it can be seen that the hardness impression alone reduces life by a factor of five. Among the contaminants used A1, TiN, NaCl and hydride, only TiN and NaCl appear to have an additional effect on fatigue life. A further reduction of life by a factor of about three is observed for these contaminants. However, the hydride used for this group of specimens had a hydrogen content of 0.35% while those used previously have a hydrogen content of 1.2% which may have affected the results.

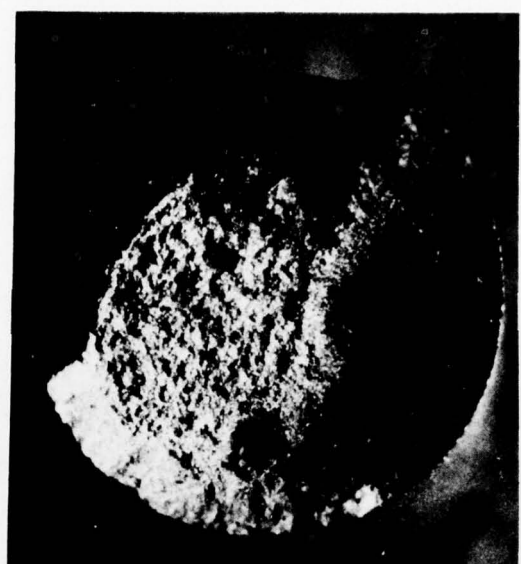
TABLE 1

70°F LCF LIVES OF SEEDED Ti-6Al-4V SPECIMENS  
 ALPHA-BETA FORGED MICROSTRUCTURE  
 0-120 KSI, 1 cpm

<u>Seeded Contaminants</u>	<u>Cycles to Failure (Specimen No.)</u>	
	<u>First Set (0.01" Pore)</u>	<u>Second Set (0.03" Pore)</u>
None, Control Specimen	---	2,100 (#17) 3,250 (#19)
None, Diffusion Bond Only	---	2,350 (#11)
None, Pore	2,910 (#1)	6,890 (#10)
TiO <sub>2</sub>	3,200 (#3) 2,240 (#8)	1,440 (#12)
Al	---	930 (#9)
Ti <sub>3</sub> Al	4,040 (#5)	---
TiN	---	410 (#14) 280 (#13)
NaCl	---	---
MgCl <sub>2</sub>	---	210 (#15)
Ti-6Al-4V	2,560 (#6)	50 (#16)
Hydride*	2,070 (#7)	

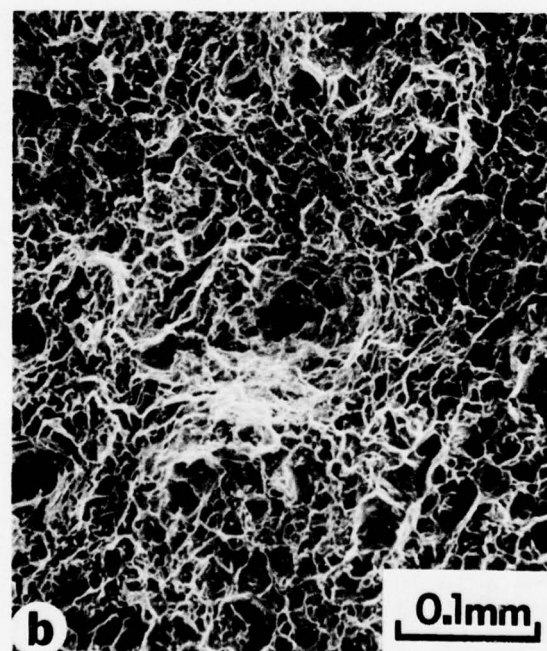
\* Hydrogen content 1.2%

--- No Test



a

2.0mm

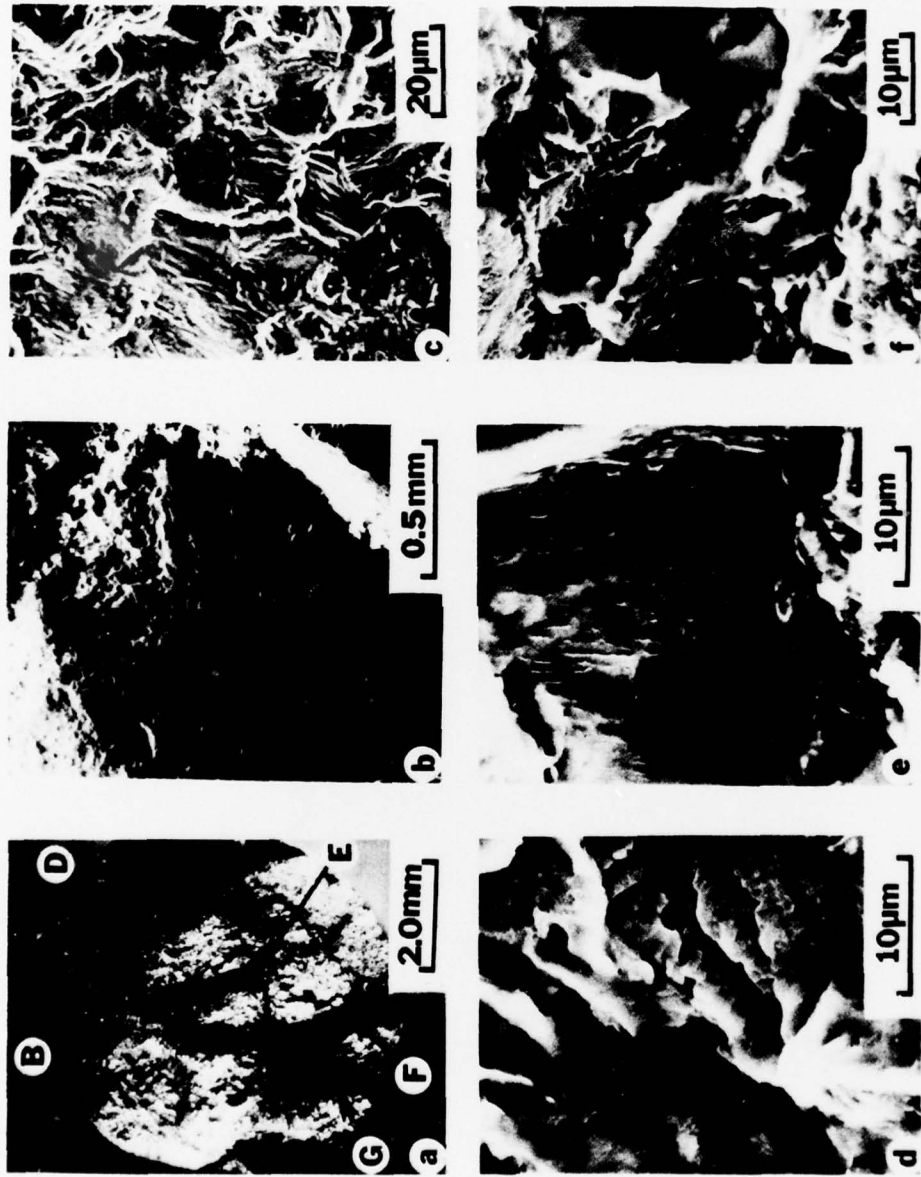


b

0.1mm

**Figure 3** (a) General Appearance of the Fracture Surface of a Hydride-Seeded Specimen (No. 16). Note the circumferential shear lip. The subsurface nucleation site could not be located.

(b) Typical Topography of the Fracture Surface



Scanning Electron Micrographs of the Fracture Surface of the Ti-6Al-4V Specimen No. 10 (Pore Only). The microstructure is given in Figure 2(a). (a) General appearance of the entire fracture surface. Note the circumferential shear lip and the five subsurface nucleation sites facets B, D, E, F and G. Facet B is shown in greater detail in (b), while the typical striation observed at its periphery is illustrated in (c). The striations observed in (c) are shown in (d), (e) and (f).

Figure 4

TABLE 2

**70°F LCF LIVES OF SEEDED Ti-6Al-4V SPECIMENS  
BETA-ANNEALED MICROSTRUCTURE  
0-110 KSI, 1 cpm**

<u>Seeded Contaminant</u>	<u>Cycles to Failure (Specimen No.)</u>
None, Control Specimen	26,230 (J-11)
None, Pore (0.03" Diagonal)	5,870 (#26)
Al	6,360 (#23)
TiN	2,430 (#22)
NaCl	2,460 (#24) 2,690 (#25)
Ti-6Al-4V Hydride*	6,660 (#21) 6,660 (#27) 14,260 (#28)

\*Hydrogen content 0.35%

The scanning electron fractography showed that the fatigue fracture was initiated at the seeded defects in all specimens with possibly one exception, specimen #24, NaCl contaminant, in which the seeded defect could not be located.

There was no evidence that specimens separated along the diffusion bond. The fractographic features in all these specimens were very similar. A typical scanning electron fractograph of a subsurface initiated and propagated fatigue crack is shown in Figure 5a, that of a near-surface initiated fracture is shown in Figure 5b. Both of these specimens were seeded with hydride and have equivalent fatigue lives. In Figure 5a the fatigue origin (hardness indentation) which is partially exposed can be observed at the center of the micrograph. A comparison of Figures 5a and b shows that the topography of the fatigue propagated region appears to be rougher than that of the surface or near-surface initiated fracture. Another common difference in the fractographic features between surface and subsurface nucleated cracks is in the appearance of the striations. The striations in the latter case tend to be wavy and ill-defined. This difference has already been illustrated in Figure 4 for the case of an equiaxed alpha:beta microstructure. Similar difference can also be observed in the present case of an acicular microstructure as shown in Figures 6a and b which illustrate the striations observed on facet A of Figures 5a and facet B of Figure 5b, respectively. Superficially the fracture appearance resembled those observed in IMI 685 which are described in Section II.2.b(3). The surface roughness was smaller in the case of Ti-6Al-4V but this can be related to the scale of the microstructure in relation to IMI 685, in Ti-6Al-4V the beta grain size and colony diamensions were smaller, as can be seen by comparing Figures 2b and 11.

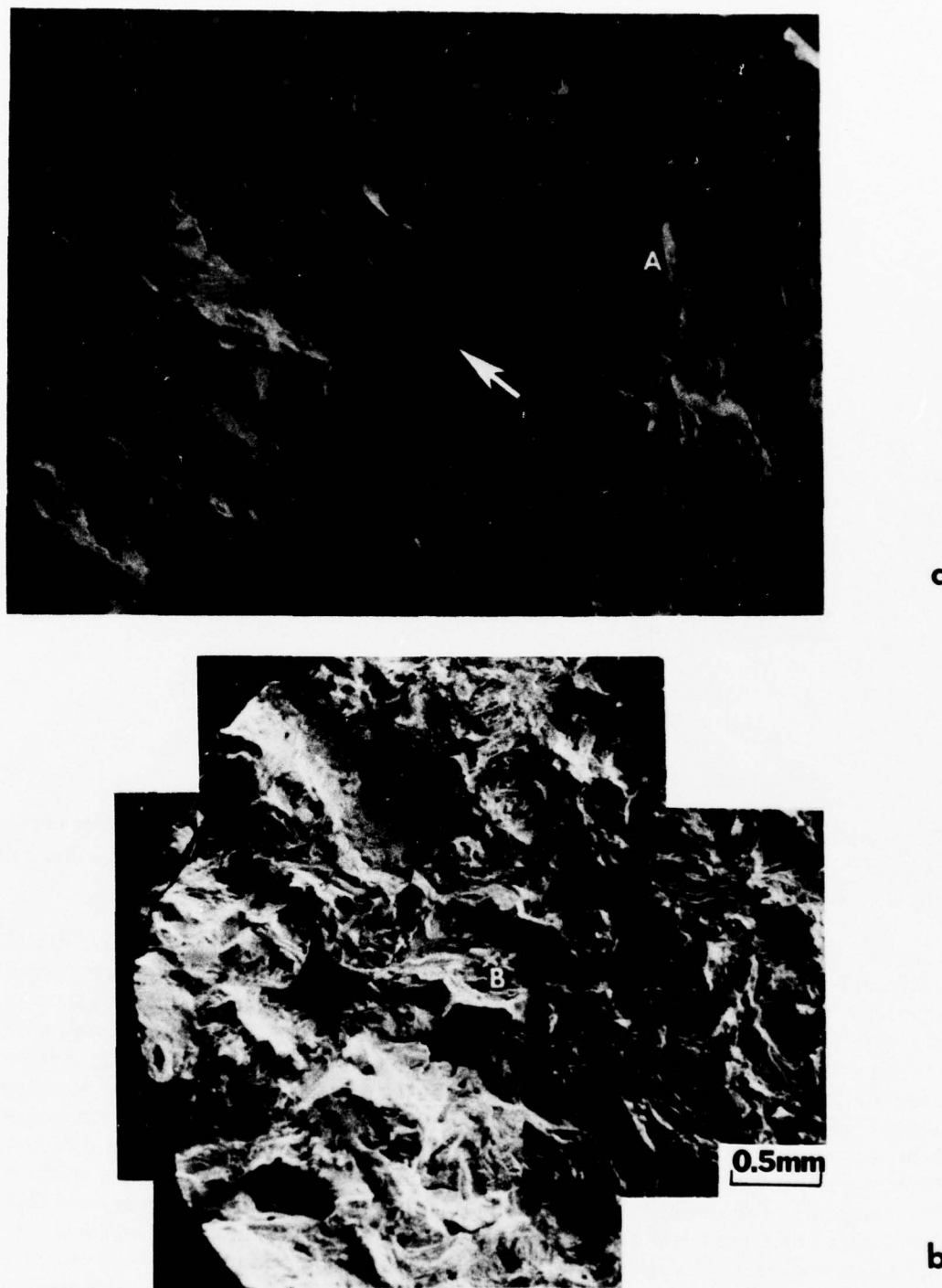
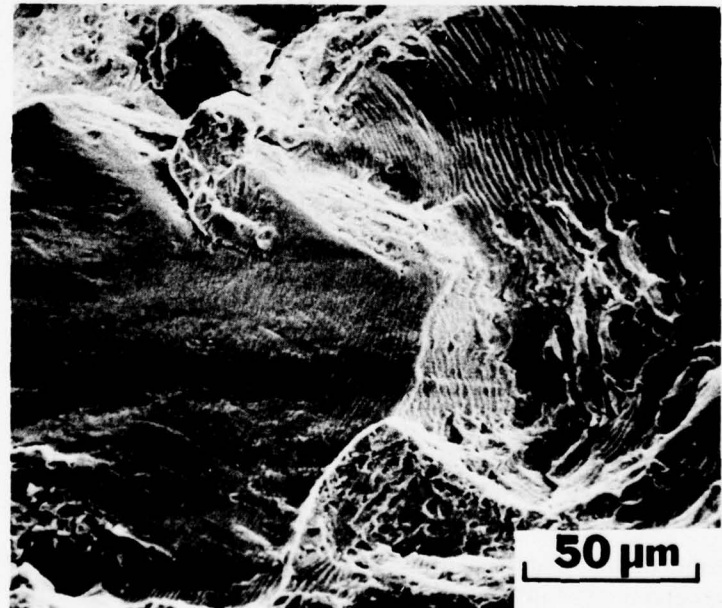


Figure 5 Scanning Electron Fractographs of Hydride-Seeded Ti-6Al-4V with Acicular Microstructure shown in Figure 2(b). (a) Subsurface fracture initiated at the seeded pore (partially exposed) indicated by an arrow. (b) Fracture initiated at the seeded pore near the surface. Striations observed on facets A and B are illustrated in Figure 6.



**a**



**b**

**Figure 6** (a) Striations Observed on Facet A of the Fracture Surface Shown in Figure 5(a).  
(b) Striations observed on Facet B of the Fracture Surface Shown in Figure 5(b).

In the case of one of the contaminants which produced the greatest reduction in fatigue life, NaCl, evidence of a reaction layer around the hardness impression was detected. Figure 7 shows the structure at the edge of an indentation in this specimen in which this reaction layer can be seen. Such an interaction layer produces an increase in the effective size of the flaw and as discussed below probably accounts for the lower life of these two specimens. In the case of the TiN-seeded specimen which also showed a large life reduction, no evidence of such a reaction layer was found.



Figure 7 Appearance of the Region Adjacent to the NaCl-seeded Pore. Note the reacted layer around the tip of the pore (hardness indentation).

Another possible contaminant that could be introduced into titanium alloys during processing is the inert gas argon. The introduction of argon into an artificial cavity in a controlled manner using diffusion bonding methods is a difficult problem. Unless extreme care is taken argon can be trapped over much of the bond area which can result in poor adhesion and consequently low properties. In the series of experiments described below the alloy Ti-6Al-2Sn-4Zr-2Mo (Ti-6-2-4-2) was used. The scheme illustrated in Figure 8 was employed to fabricate specimens with cavities containing argon. Sections of the dimension shown in Figure 1 were machined from bar stock, 0.5" in diameter. One of the rods was machined to a hemispherical shape radius 0.41" at one end, which was in contact with a small cavity in the end of the other rod. The two rods were assembled into an alumina die in an argon atmosphere, the load applied and the temperature increased. The plastic deformation in the contact surfaces helps to seal

the argon in the pore while the curvature limits the argon trapped at the interface. Ideally, the argon should be evacuated as soon as the pore has been sealed. Since the condition for the adequate sealing could not be readily determined, argon was evacuated at two arbitrarily selected temperatures, either 200°F or 800°F. Two diffusion bonding conditions were used, 1750°F under 500 psi for 4 hours and 1850°F under 560 psi for 4 hours. To produce an acicular microstructure, the bonded rods were given a beta heat treatment of 2000°F for 1 hour in vacuum followed by furnace cooling. Specimens prepared from the bonded sections were tested at 0-110 Kpsi, 1 cpm.

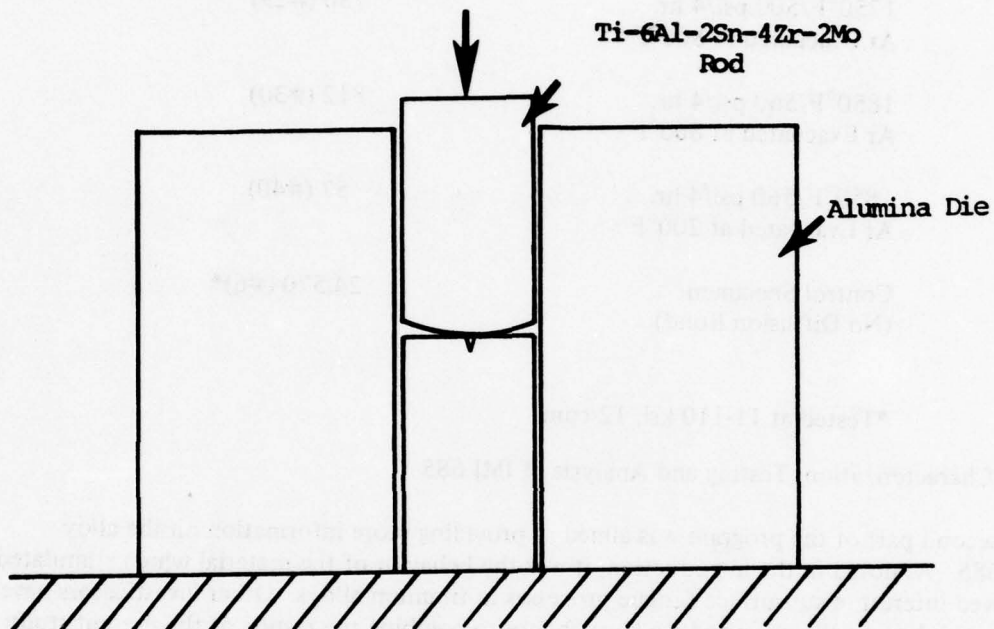


Figure 8 Experimental Setup for Trapping Argon in a Pore Between Two Rods Which Were Subsequently Diffusion Bonded Together and Machined into a LCF Specimen

The LCF lives of Ti-6Al-2Sn-4Zr-2Mo seeded with argon are shown in Table 3 which also lists the diffusion bonding conditions used. The fractographic features of the first specimen tested (#29) consist of a central region where the argon pore is located and a peripheral region, both of which show evidence of good bonding. Between these two regions is an area on which the markings on the original surface are clearly visible. The formation of this apparently unbonded region was due to incomplete removal of argon during diffusion bonding. An improved bond was produced in the third specimen (#40) when argon was evacuated at about 200°F. However, unbonded regions were still evident on the fracture surfaces indicating the inherent difficulty of completely removing the argon once introduced. This specimen also exhibited the lowest life of the three specimens tested which complicates the assessment of these results.

TABLE 3

**70°F LCF LIVES OF Ti-6Al-2Sn-4Zr-2Mo  
SEEDED WITH ARGON  
0-110 KSI, 1 cpm**

Diffusion Bond Conditions	Cycles to Failure (Specimen No.)
1750°F/500 psi/4 hr. Ar Evacuated at 800°F	730 (#29)
1850°F/560 psi/4 hr. Ar Evacuated at 800°F	812 (#30)
1850°F/560 psi/4 hr. Ar Evacuated at 200°F	57 (#40)
Control Specimen (No Diffusion Bond)	24,570 (#6)*

\*Tested at 11-110 ksi, 12 cpm

b. Characterization, Testing and Analysis of IMI 685

The second part of the program was aimed at providing more information on the alloy IMI 685. As noted in the introduction, it was the behavior of the material which stimulated renewed interest in subsurface fatigue processes in titanium alloys. Other investigators have generated data on the alloy and we have chosen to combine the results of the present study with the earlier information in parts of the following section. As most results are consistent, this serves to provide a reasonably complete description of the behavior pattern of IMI 685 under cyclic stress conditions.

(1) Material

Two sections of a circular IMI 685 machined forgings were provided to Pratt & Whitney Aircraft by the AFML for this study. The billet had been beta-blocked and alpha:beta finished followed by a beta-anneal at 1922°F, oil quench and stress relief at 1076°F. Because of the size and shape of the forged preform this heat treatment resulted in a considerable microstructure variation within the forging and also tensile residual stress of 15-20 ksi in the rear surface of the disk section machined from it<sup>(8)</sup>. The microstructures and room temperature tensile properties at various locations in this material have been reported by Eylon and Hall<sup>(5)</sup>. The two sections were cut from a machined forging which was retired from service after 62 stress cycles when several cracks were observed at the rear surface. The maximum stress during service has been estimated to be about 90 ksi. A schematic representation of the machined forging is shown in Figure 9 which also identifies the directions cited in the following paragraph.

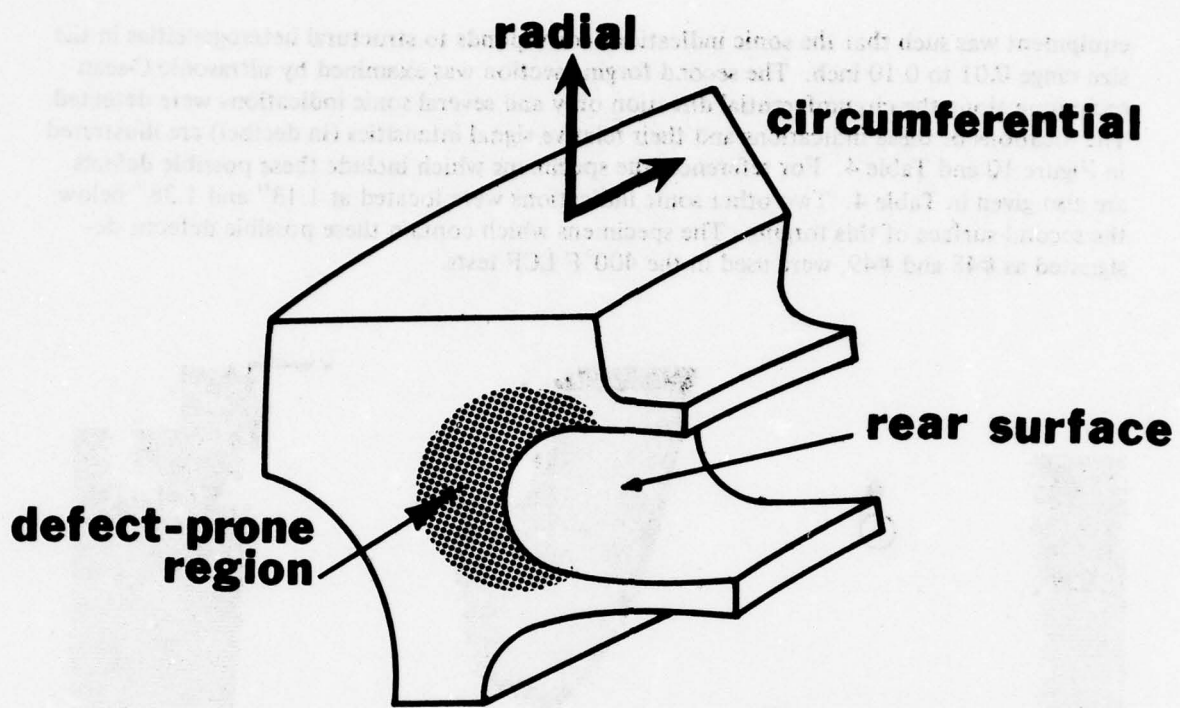


Figure 9 Schematic of the Machined IMI 685 Forging

The first section was received at the beginning of this program. At that time it was assumed that the defects were spherically symmetric and therefore independent of the orientation of the specimen relative to the forging. The main purpose of the preliminary experiments was to define a simple specimen geometry and a testing procedure such that the defects could be exposed for subsequent studies. Specimens with different orientations and geometries were prepared and tested. As will be described, results from specimens machined from the first section indicated that the initial assumption on defect orientation was incorrect. The characteristic features of a rosette failure were only observed in specimens cut in the circumferential direction. Consequently, all the specimens from the second section, which was provided to P&WA after the first year of the contract, were machined with their longitudinal axes parallel to the circumferential direction of the disk. Most of the data in this report were obtained from the second section.

## (2) NDI Characterization of Defects

The first section had three defective areas marked on the rear surface of the forging. Materials cut at these locations were investigated by nondestructive techniques using x-ray radiography and ultrasonic C-scan techniques prior to machining into specimens. Analysis was conducted parallel to the radial and the circumferential directions. The x-ray radiographs gave no definitive indication of the presence of cracks or other structural heterogeneities. Sonic indications were obtained only when the probe scanned on a surface normal to the circumferential direction of the forging suggesting a planar nature for the defects. The sensitivity of the ultrasonic

equipment was such that the sonic indications corresponds to structural heterogeneities in the size range 0.01 to 0.10 inch. The second forging section was examined by ultrasonic C-scan technique along the circumferential direction only and several sonic indications were detected. The locations of these indications and their relative signal intensities (in decibel) are illustrated in Figure 10 and Table 4. For reference, the specimens which include these possible defects are also given in Table 4. Two other sonic indications were located at 1.13" and 1.38" below the second surface of this forging. The specimens which contain these possible defects, designated as #48 and #49, were used in the 400°F LCF tests.

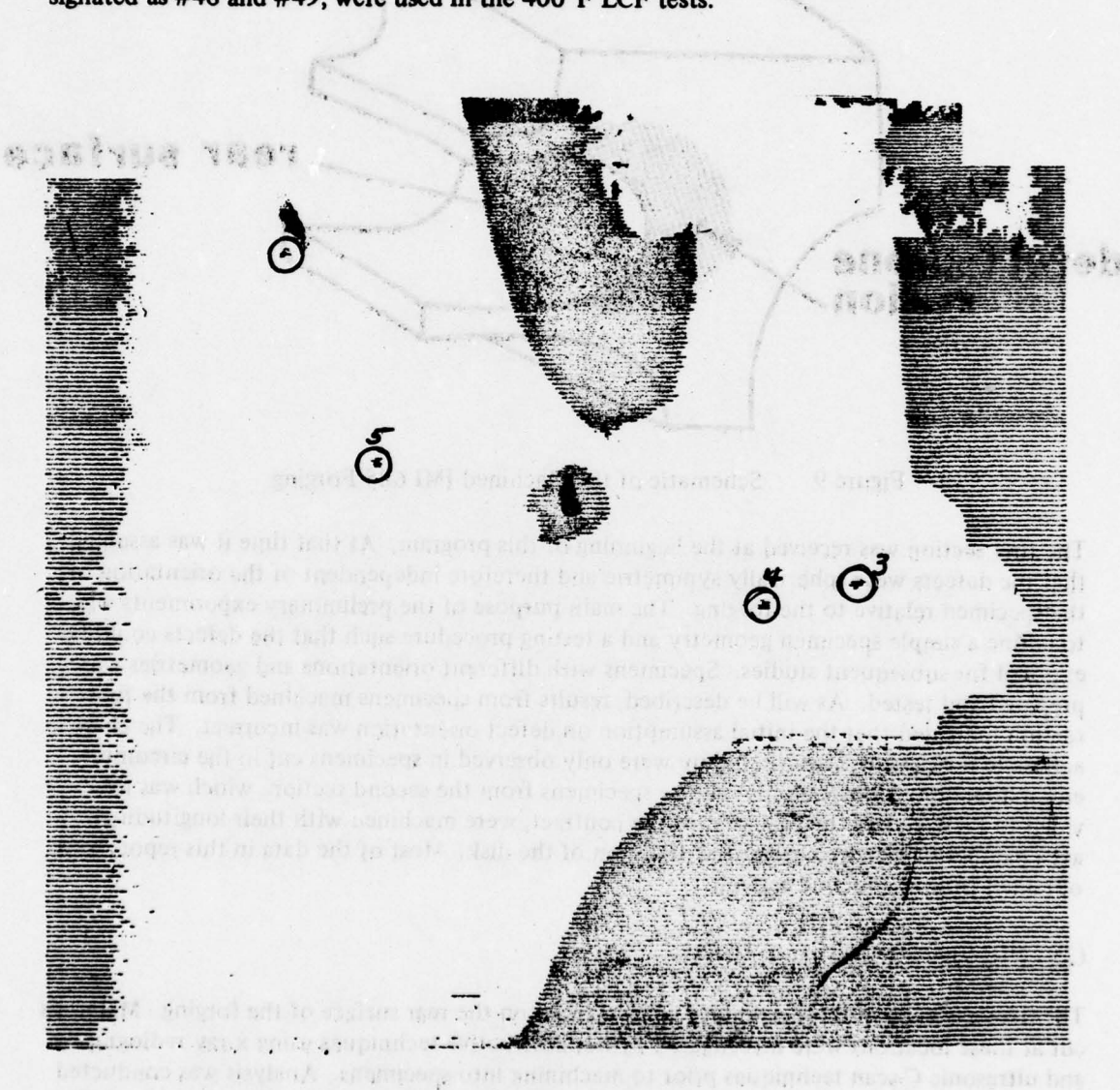


Figure 10 Ultrasonic C-Scan Recording from an IMI 685 Forging Section. The probe was oriented parallel to the circumferential direction of the forging.

TABLE 4  
ULTRASONIC C-SCAN RESULTS ON SURFACE A OF THE  
SECOND IMI 685 FORGING SECTION

<u>Defect No.*</u>	<u>Signal Strength</u>	<u>Depth</u>	<u>Specimen No. and Test</u>
1	2 dB	0.75"	20, Uploading LCF
2	12 dB	1.25"	22, 70°F Dwell Test 30-100 Ksi
3	2 dB	0.50"	No Specimen Machined
4	1 dB	0.88"	23, 400°F Dwell Test 30-100 Ksi
5	1.5 dB	0.75"	21, 400°F Dwell Test 30-100 Ksi

\*See Figure 10

An important question in the analysis of the LCF behavior of this forging is the specific nature of these sonic indications. During specimen fabrication, to locate one such indication within the gage section, several cracks were exposed.

These cracks were oriented at small angles to the radial direction of the forging and ranged in size from 0.02" to 0.04" and are illustrated in Figure 11. Thus it is implied that several, if not all indications are cracks. As the forging had received a total of 62 LCF cycles before it was received at P&WA we can estimate the average cracking rate to form the sonic indications (cracks). These cracking rates range between  $3 \times 10^{-4}$  to  $6 \times 10^{-4}$  inch/cycle for the crack lengths cited above. It is also possible that other indications could represent grains or groups of grains in a specific orientation favorable for attenuation of the beam since this material has large prior beta grains averaging  $\sim 0.06"$  in diameter.

To determine whether any preferred orientation was present in the material arising from the thermo-mechanical history, x-ray pole figures were determined from material taken at the defect-prone region of the forging. The area scanned by this x-ray beam was 0.5 inch square. The plane of examination was normal to the circumferential direction of the forging. Pole figures for the (0002) and (1010) planes are given in Figures 12(a) and (b) respectively, showing that the grains are oriented relatively randomly.

### (3) Fatigue Testing at 70°F

#### (a) Radial Direction

Three specimens were machined from the first forging section to include a defect within their gage section. The three-point bend specimen (#1) shown in Figure 13a and the tension specimen (#2) shown in Figure 13b were machined with longitudinal axes parallel to the radial direction of the forging. Specimen #4 shown in Figure 13c was fabricated by a diffusion bonding method which is described below and was constructed so that the tension axis was parallel to the circumferential direction. The specimens were electropolished prior to testing.

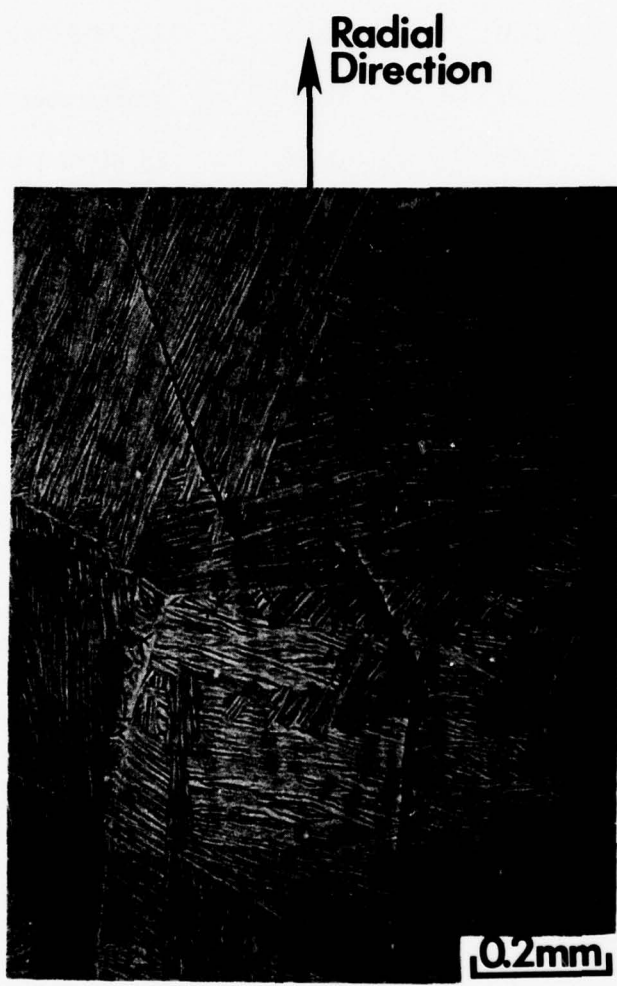


**Figure 11** Microstructure and Cracks Observed at the Defect-Prone Area of the IMI 685 Forging Which had 62 Stress Cycles Before Retirement From Service

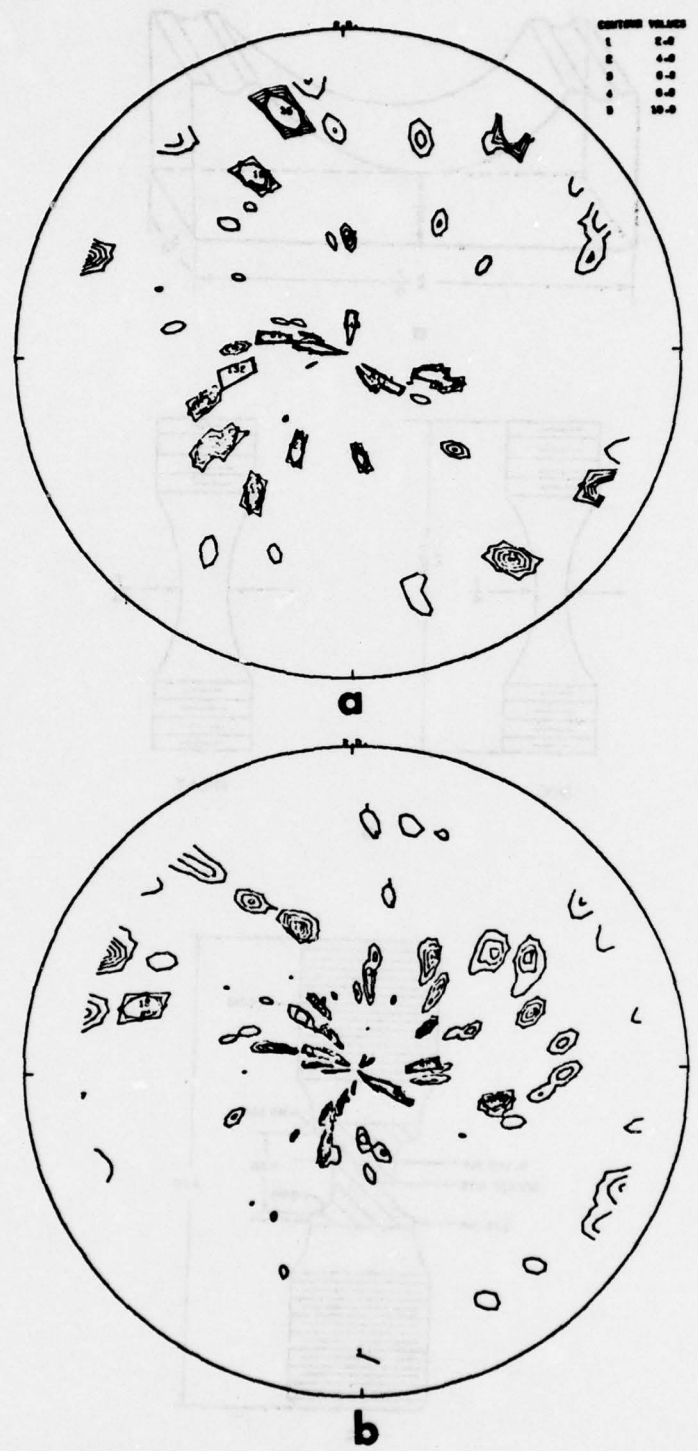
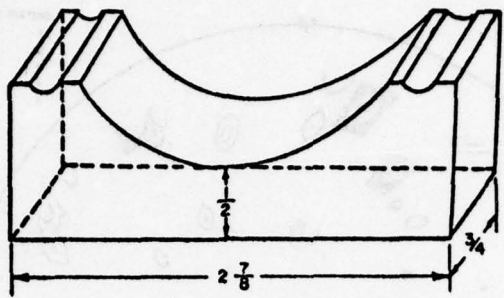
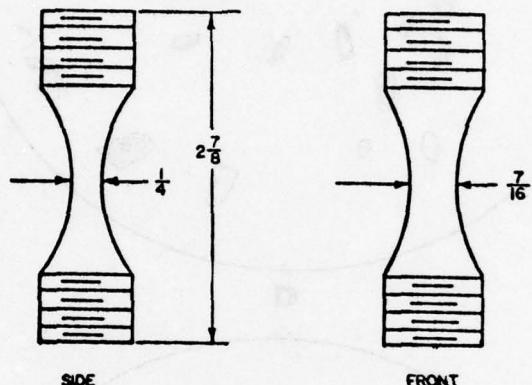


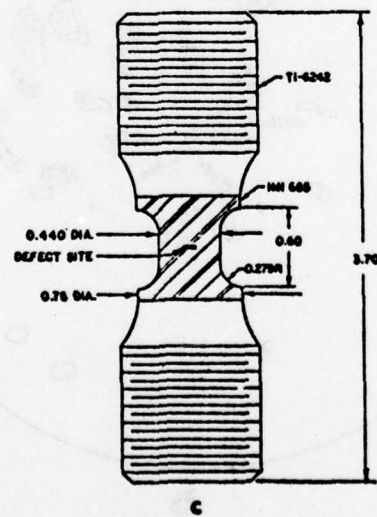
Figure 12 X-ray Pole Figures (a) (0002) Pole and (b) (1010) Pole



a



b



c

Figure 13 Dimensions of (a) Three-Point Bend Specimen (b) Tension LCF Specimen No. 2 and (c) Tension LCF Specimen No. 4

Optical examination of the surface of the bend specimen prior to testing revealed no surface cracks. Testing was performed by bending under a stress range of 0-95 ksi which was monitored by a strain gage. A rectangular wave form was used with a hold time of 10 minutes at maximum stress. In order to accelerate failure the stress was increased when a crack had formed which intersected the specimen surface. The specimen failed after 1840 cycles. Two cracks had formed during the test and their locations are indicated in Figure 14a. The general appearance of the fracture surface of the major crack is shown in Figure 14b which also indicates the general position of the fracture origin. Scanning electron fractography revealed that the crack origin was slightly subsurface as shown in Figure 15 which also illustrates the cleavage-like topography adjacent to the origin. No material discontinuities such as pores were formed at the initiation site. The second crack (B) was also exposed by sectioning and the fracture surface was found to be very similar to that of the major crack. Again no features typical of a rosette failure origin were found in this crack. These bend tests were an attempt to provide a rosette failure for analysis as quickly as possible. It is obvious that such specimens are not suitable for studying subsurface failures so all further testing was performed on specimens loaded in tension.

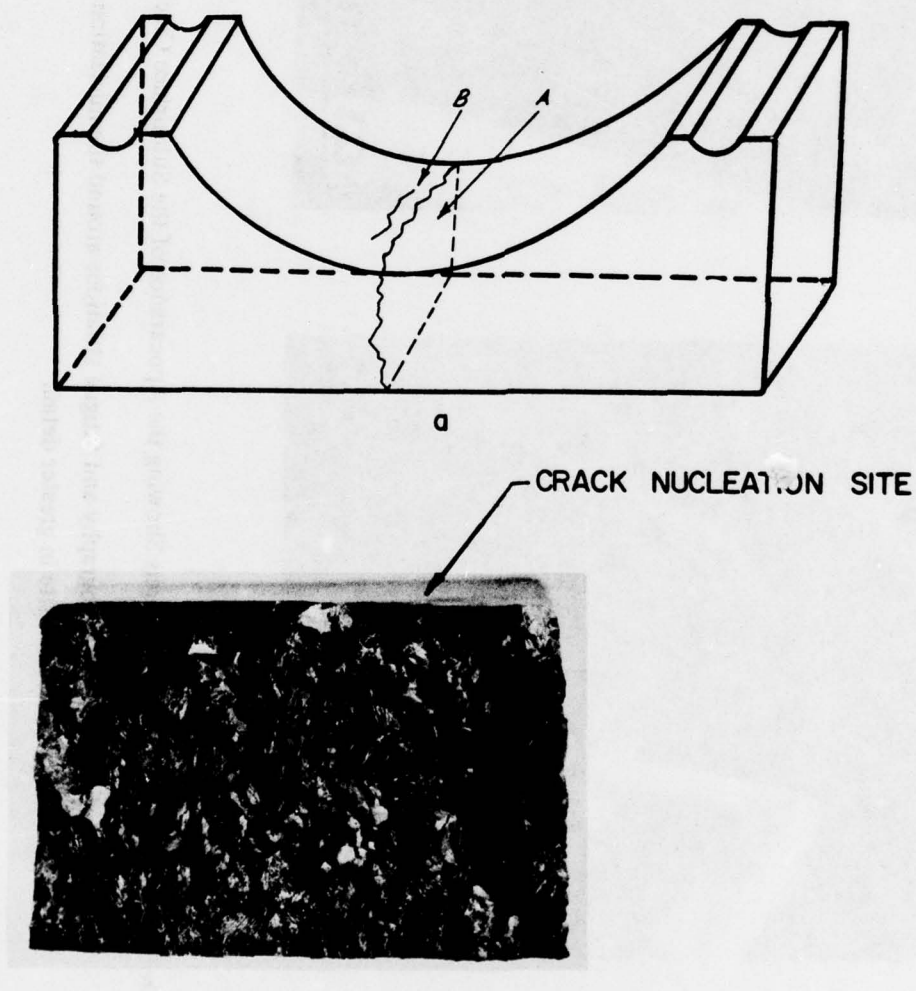


Figure 14 (a) Schematic Diagram Showing the Locations of Cracking in the IMI 685 Bend Specimen after LCF Testing and (b) Appearance of the Fracture at Location A

Figure 14 shows a general view of subsurface crack nucleation site in the upper surface of the specimen. A fatigue crack has been initiated at the top of the specimen and has propagated downwards. A scale bar is shown in the bottom left corner.

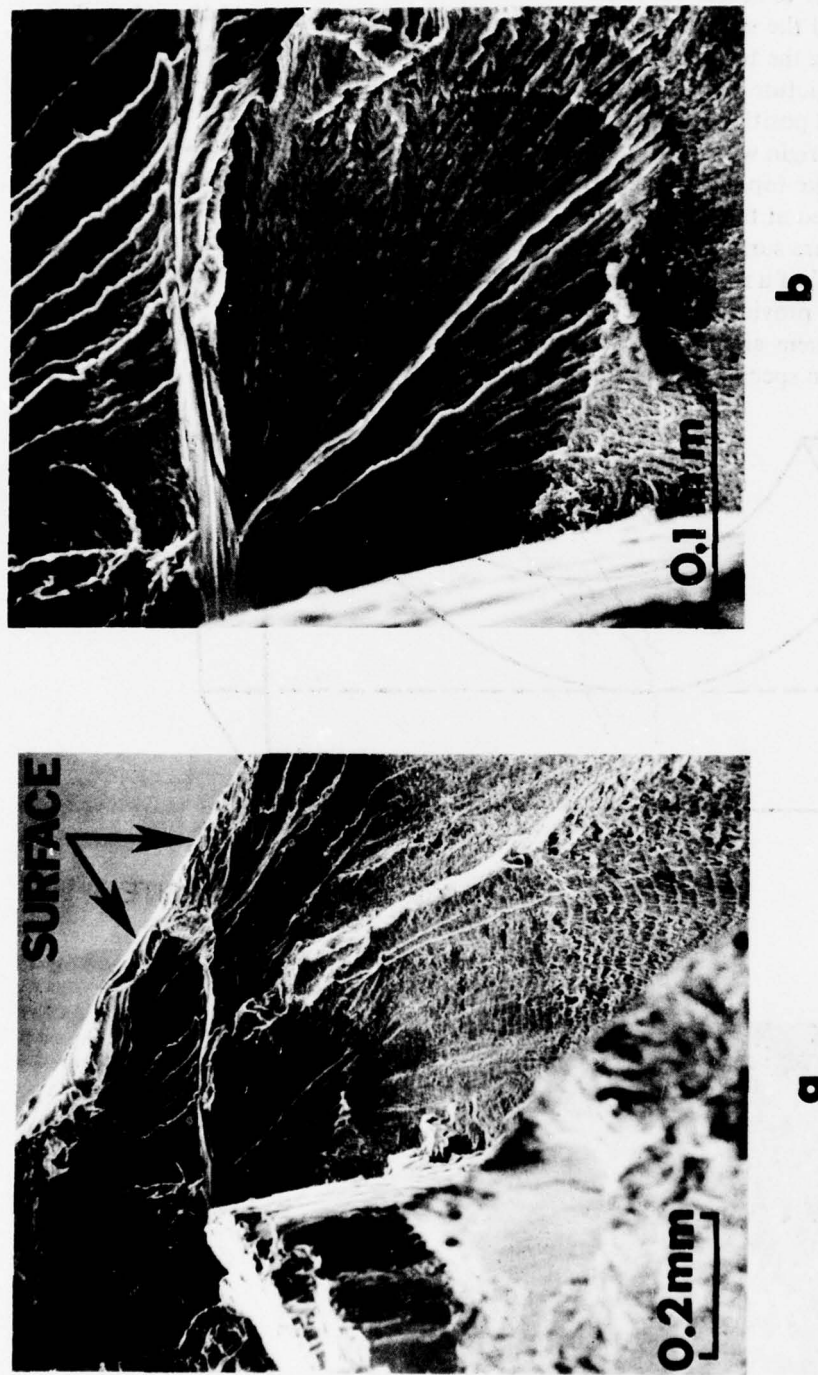


Figure 15 Scanning Electron Micrographs Showing the Appearance of the Subsurface Crack Nucleation Site Indicated in Figure 14b.

- shows the cliff-like topography and fatigue striations around the nucleation site.
- shows the nucleation site in greater detail.

The LCF tension specimen (#2) was tested at a stress range of 5-100 ksi with a dwell of 10 minutes at maximum load, i.e., at a cyclic frequency of about 6 cycles per hour. Fracture occurred after 292 cycles. As will be shown this is obviously well below the fatigue capability of this alloy in a defect-free condition. Several cracks were observed on the surface of this specimen after machining and it was anticipated that these may have influenced the failure of the specimen. A careful comparison of the gage surface before and after fracture indicated that none of the pre-existing cracks had propagated. The fracture surface is shown in Figure 16 and again the general cleavage-like appearance is evident. The curvatures of "river markings" and the fatigue striations observed at the edge of region D and at regions E and C indicated that the fracture origin was located at region D. Small pores characteristics of the rosette origins were not observed although brittle-type striations were present in region D. As will be described later, this type of markings is typically observed near the origin of rosette failure. Although the major fraction of the fatigue surface was cleavage-like, isolated patches of striations were observed.



Figure 16 Scanning Electron Micrographs Illustrating the General Appearance of the Fracture Surface in the IMI 685 LCF Tension Specimen No. 2. Striations on regions C and E can be traced to an origin at region D. Arrows indicate directions of crack propagation.

An interesting observation of the striations on facet E is shown in Figure 17 from which it can be seen that the striation spacings decrease from left to right indicating that the crack slowed down during propagation across this facet. The implication of this observation will be discussed later.

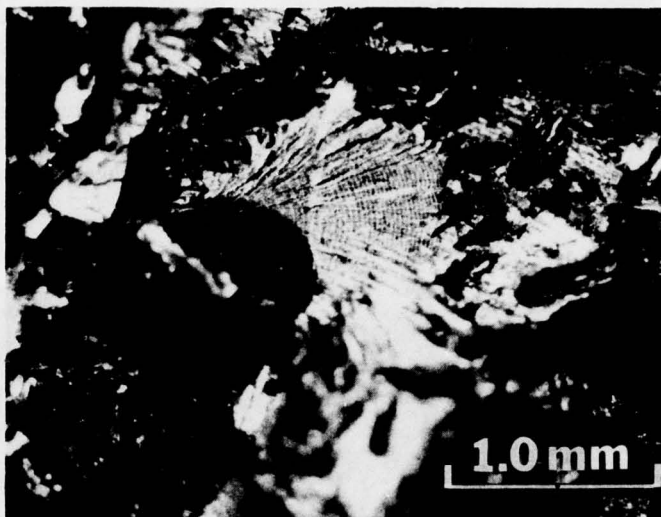


Figure 17 Fatigue Striations Observed on Facet E of the Fracture Surface Shown in Figure 16. Note the gradual decrease in striation spacing as the crack propagated across this facet from left to right.

#### (b) Circumferential Direction

Due to the lack of sufficient material from the first forging section, specimen #4 was fabricated by diffusion bonding Ti-6Al-2Sn-4Zr-2Mo threaded pull-bars to the defect-containing section as shown in Figure 13c. The bonding was carried out at 1750°F under 500 psi for 4 hours at a vacuum of  $10^{-5}$  torr. It was considered that this treatment would also relieve any residual stress present in the material. Specimens from the second forging section were fabricated with their gage length containing sonic-indicated defects (See Table 4). Other specimens were prepared from areas without sonic indications. Most of the specimens were located near the rear surface of the forging. The dimensions of all the specimens fabricated from the second forging section are given in Figure 1. Specimens were tested with as-machined surfaces. The specific test conditions used will be given below.

Results of tests in the present study are combined with results of other investigators in Tables 5 and 6 which also list the location of fatigue origins.

TABLE 5

## 70°F DWELL LCF TESTS OF IMI 685

Specimen No.	C-Scan Indication	Stress Range		Fracture Life Cycles	Initiation Site		
		Ksi	MN/m <sup>2</sup>		Surface	Subsurface	Rosette Defect
4(a)	I	5-100	345-689	1,600		X	X
20(a)	I	29-97	200-668	600-2600		X	X
22(a)	I	30-100	207-689	1,736		X	X
47(a)	NI	35.6-118.5	245-816	552		X	
15(b)	*	30-100	207-689	42,892		X	
16(b)	*	33-110	227-758	207		X	X
17(b)	*	33-110	227-758	8,702		X	
18(b)	*	36-120	248-827	790		X	
19(b)	*	36-120	248-827	217		X	
(c)	*	33.6-95.2	232-656	752		X	
(c)	*	33.6-95.2	232-656	878		X	
(d)	*	0-116.5	0-803	19,000	*	*	*
(d)	*	0-130.6	0-900	1,300	*	*	*

I Indication

NI No indication

\* No data

(a) Present Work, 5-minute dwell at maximum load

(b) Ref. 5, 5-minute dwell at maximum load

(c) Ref. 9, 10-minute dwell at maximum load

(d) Ref. 12, 2-minute dwell at maximum load

TABLE 6  
70°F NON-DWELL LCF TESTS OF IMI 685

Specimen No.	C-Scan Indication	Stress Range		Fracture Life Cycles	Initiation Site		Rosette Defect
		Ksi	MN/m <sup>2</sup>		Surface	Subsurface	
6(a)	NI	0-110	0-758	22,556		X	
7(a)	NI	0-110	0-758	33,949	X		
24(a)	NI	36-126	248-868	10,640	X		
25(a)	NI	36-126	248-868	860		X	X
45(a)	NI	36-120	248-827	25,000	X		
1(b)	*	33-110	227-758	24,464	X		X
2(b)	*	33-110	227-758	102,473	X		
3(b)	*	36-120	248-827	37,958		X	
4(b)	*	36-120	248-827	29,845		X	
5(b)	*	36-120	248-827	34,215	X		
6(b)	*	36-120	248-827	39,523	X		
11(b)	*	39-130	269-896	6,244		X	X
12(b)	*	39-130	269-896	10,559		X	
13(b)	*	40.5-135	279-931	4,705		X	
14(b)	*	40.5-135	279-931	3,099		X	
(d)	*	0-102.3	0-705	150,000+	*	*	*
(d)	*	0-108.9	0-750	50,000	*	*	*
(d)	*	0-112.5	0-775	25,000	*	*	*
(d)	*	0-116.5	0-803	52,000	*	*	*
(d)	*	0-119.7	0-825	22,000	*	*	*
(d)	*	0-123.4	0-850	19,000	*	*	*
(d)	*	0-132.1	0-910	5,500	*	*	*

(a) Present Work, 12 cycles per minute

(b) Ref. 5, 20 cycles per minute

(d) Ref. 10, 10 cycles per minute

+ Test Discontinued

NI No Indication

\* No Data

These results can be used to establish the S-N curves as shown in Figure 18. Although some data scatter is apparent the data, with only one exception, falls into four groups, which are as follows. Group A includes all results of specimens which were tested under a dwell cycle and in which post-test analysis revealed a cleavage rosette including a "fish-eye". Group B and C are two sets of results which combine specimens tested under dwell cycles of 5 minutes and 2 minutes respectively, but which did not contain any known pre-existing defect. Subsequent fracture analysis indicated that subsurface origins occurred in all specimens of Group B and the failure mode was cleavage-like but no "fish eye" was present at the origin. The fourth group of specimens labeled D includes the results for specimens cycled at a fast rate and thus could be taken to represent the "normal" fatigue capability. Note that this population includes three data points generated by Eylon and Hall<sup>(5)</sup> in which "fish-eyes" were detected. The one exception to the above general behavior pattern is a test performed in the present study on a predetermined defect-containing specimen tested at a frequency of 12 cpm. In this test, failure occurred at a low life from a subsurface (rosette-type) origin, as described in more detail below.

Several trends can be discerned in Figure 18. Curve A and Curve B tend to converge at high stresses and at lower stresses Curves B, C and D tend to merge. Thus the relative fatigue debits of the Curves A, B and C with respect to D are stress sensitive. At a stress of about 115 ksi, the rosette debit is over two orders of magnitude with reference to the normal fatigue capability while the 5 minute-dwell debit is about one order of magnitude.

The fractographic features of specimens tested either with or without a dwell will now be described. Their results will be used later in an attempt to account for the observed behavior pattern in IMI 685.

#### 1) Rosette Failures (Defective Material)

The general appearance of a dwell-tested fracture, as exemplified by Specimen #4, is shown in Figure 19. The fracture origin is located near the center of this Figure and is shown in greater detail in Figure 20. The fatigue crack initiated at a macroscopically flat facet about 0.033" diameter which is inclined at a small angle to the stress axis. Near the center of this facet is a pore about 0.0002" long. A "river" pattern is observed to originate from this pore, and markings, termed "brittle-type" striations in earlier reports, were observed on this facet. Figure 21 shows the microstructure at the fracture origin before (a) and after (b) chemical etching. As illustrated in these scanning electron micrographs the "brittle-type" striations mark the positions of interfaces between the alpha platelets which contain a thin lamellar of the beta phase. The microstructure of a longitudinal section through the fracture origin is shown in Figure 22. The location of the pore is indicated by an arrow. No microstructural anomaly at the fatigue origin is apparent.

The topography surrounding the "fish eye" is highly irregular and consists of cleavage-like facets. Fatigue striations were observed on a small number of facets labelled A, B, and C in Figure 19. Those observed on facet A are shown in Figure 23. The measured striation spacings on these facets will be presented later with reference to other crack growth data (Section II.2.c(1)). The dimensions of all the facets are about the same as those of the acicular alpha colonies in this material. The crack grew to a diameter of approximately 0.3 inch before overload failure occurred. It is clear that the crack front at the onset of unstable fracture was rather irregular as areas of overload failure were intermixed with cleavage and striated facets at the periphery of the crack.

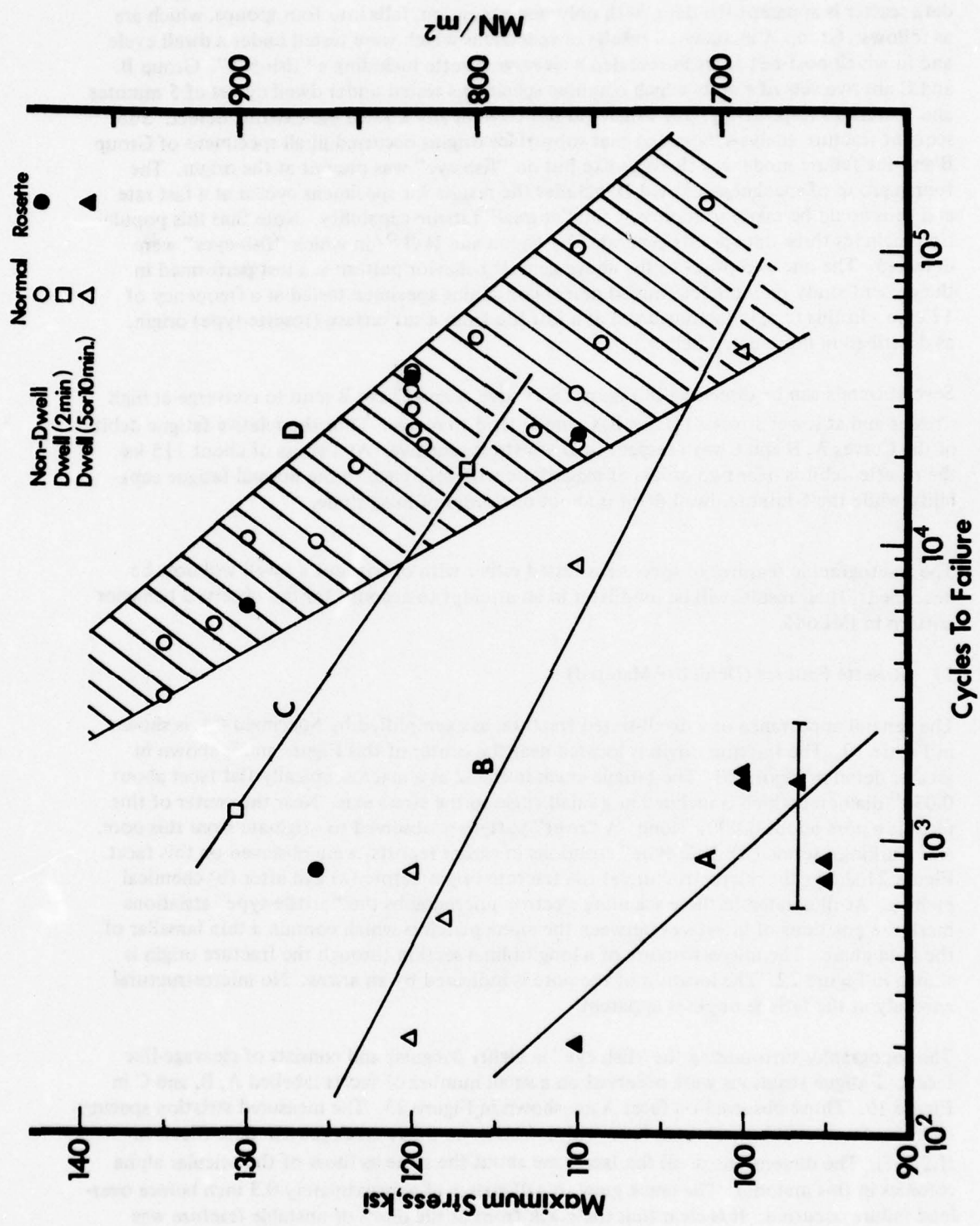
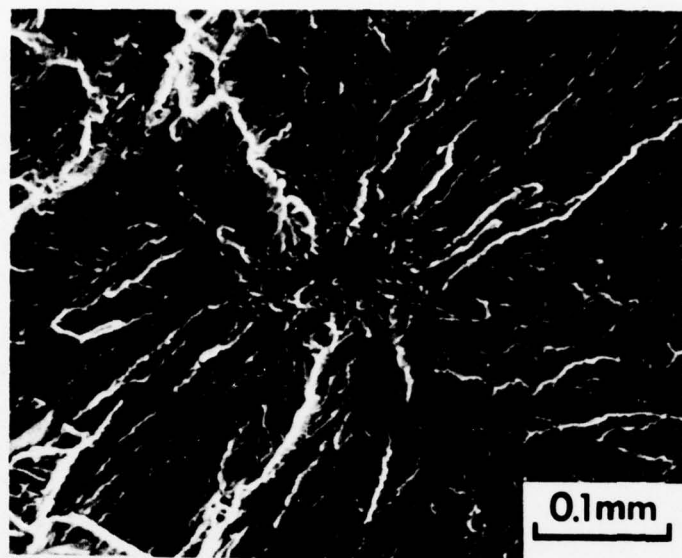


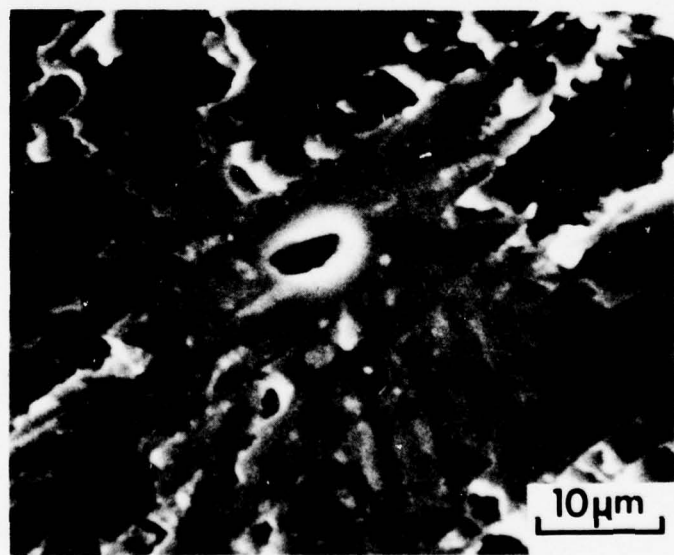
Figure 18 S-N Curves of IMI 685 at 70°F, the Sources of Data Are Indicated in Tables 5 and 6.



Figure 19 Scanning Electron Fractograph of the Rosette-Fracture Observed on IMI 685 Specimen No. 4. Details of the 'fish eye' fracture origin are shown in Figure 20. Striations have been observed on facets A, B and C. Those on facet A are shown in Figure 23.



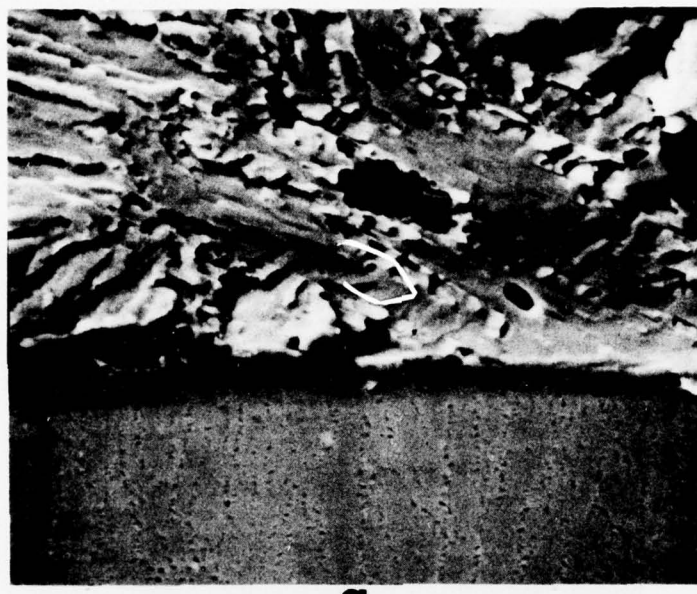
a



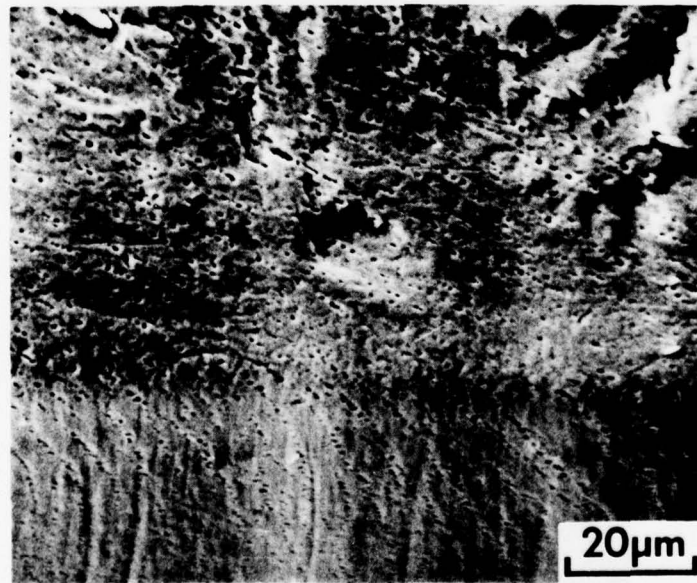
b

Figure 20 (a) The Topography of the 'fish eye' Crack Nucleation Site

(b) Detailed Appearance of the Central Pore and its Surrounding. Note the presence of the "brittle-type" striations on the 'fish eye'.



a



b

**Figure 21** Scanning Electron Micrographs of the ‘fish eye’ Fracture Origin in Specimen No. 4 Illustrating the Origin of the “brittle-type striations”.  
(a) Showing the ‘brittle-type’ striations on the ‘fish eye’ and the microstructure of a longitudinal section near the central pore and (b) longitudinal section closer to the central pore, etched to reveal the microstructure on the fracture surface. A comparison of (a) and (b) shows that the striations are located at the interface between the  $\alpha$  platelets.

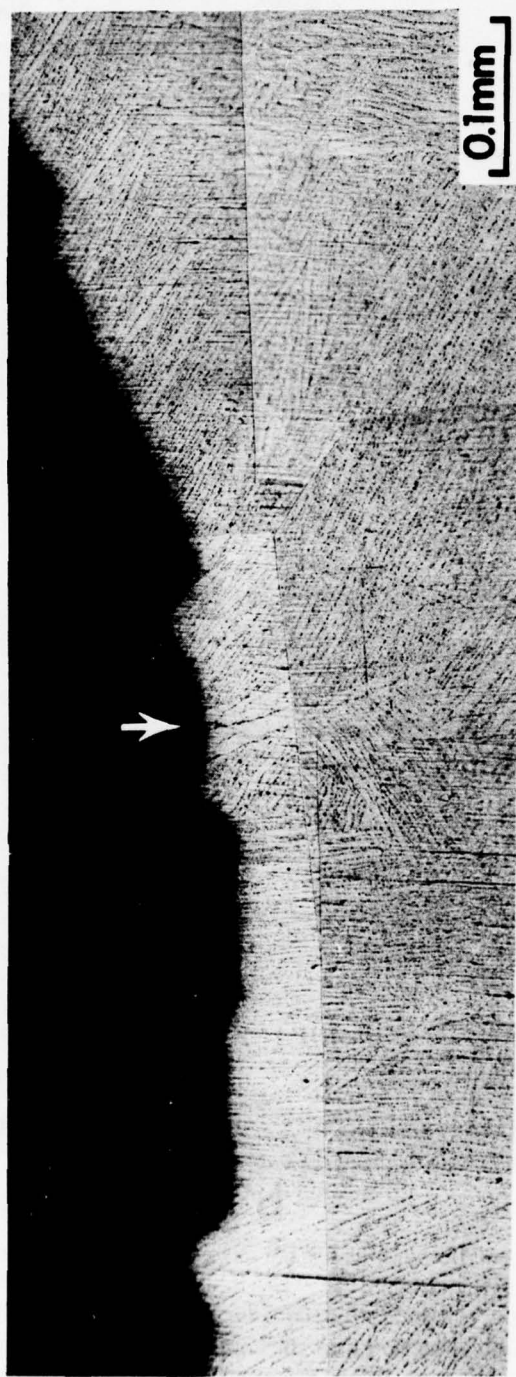


Figure 22 Microstructure at a Longitudinal Section Through the Central Pore (Location Indicated by the Arrow)

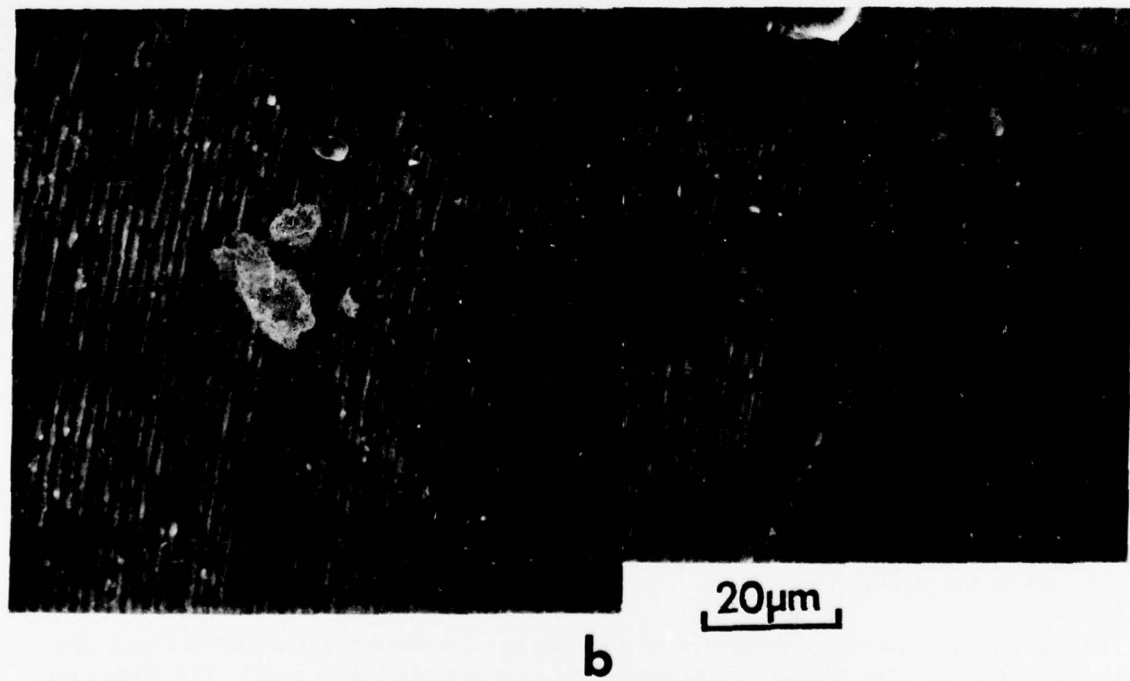
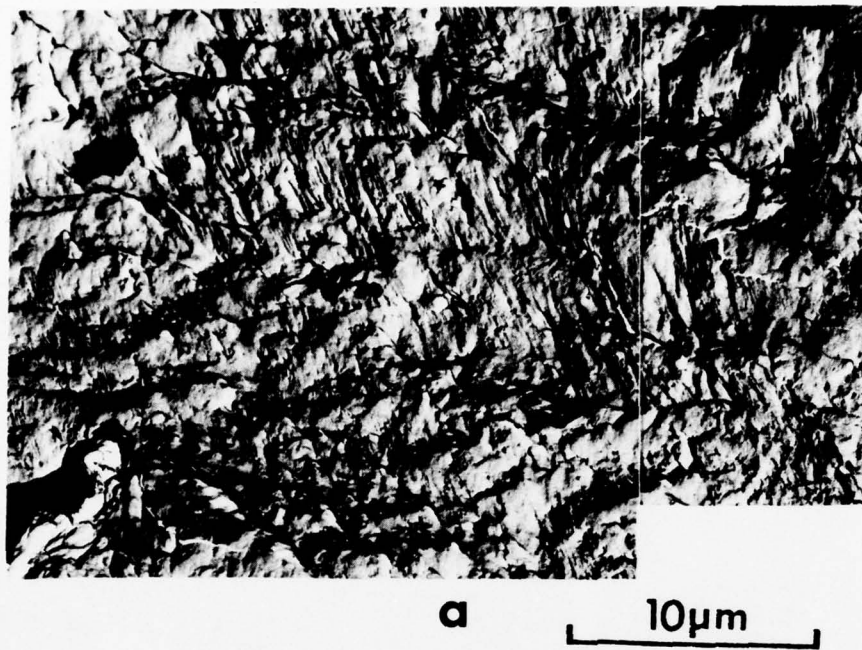


Figure 23 (a) Replica Showing Fine Fatigue Striations Between Facet A and the 'Fish Eye' on the Fracture Surface Illustrated in Figure 19.  
(b) SEM Showing Fatigue Striations on Facet A.

The general appearance of a nondwell-tested fracture surface is illustrated in Figure 24a for specimens #25 which failed after 860 cycles, 12 cpm. The fracture origin exhibits two fan-shaped facets located toward the edge of the specimen. A small pore 0.0003" long was observed in an area between the two facets, "brittle-type" striations are also present in this area (Figure 24b). Fatigue striations were observed in isolated areas surrounding these two facets. Results of the striations spacing measurements will also be presented in Section II.2.c(1).

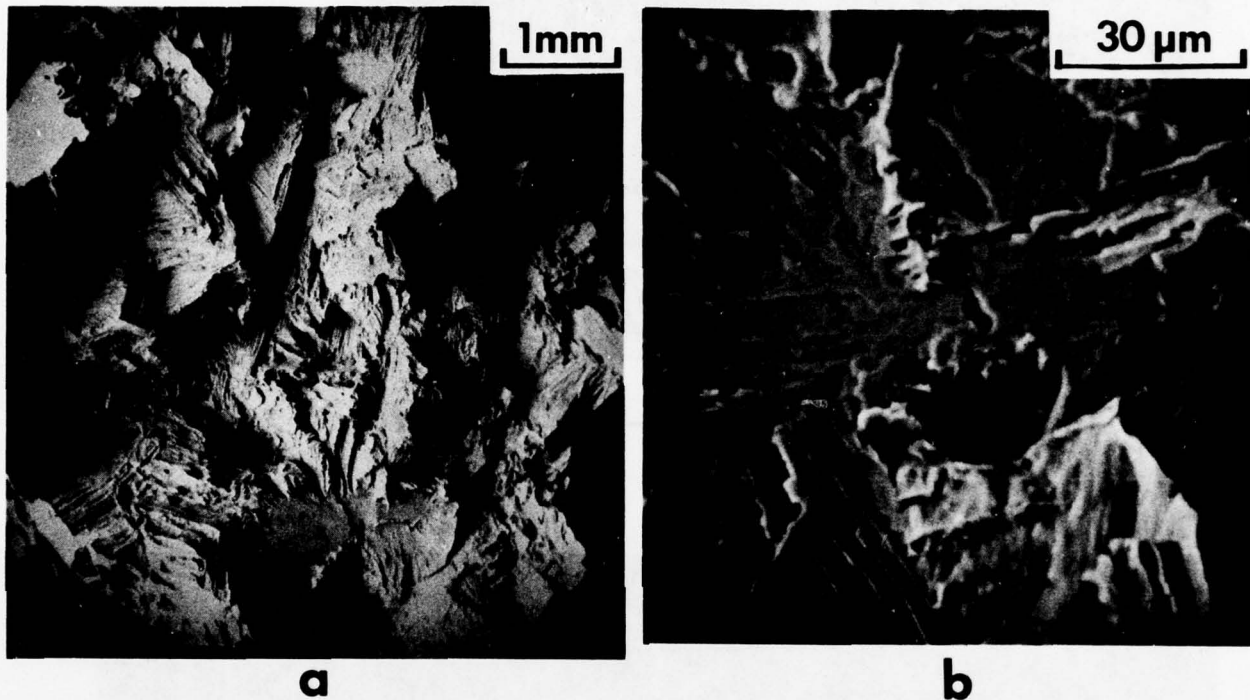
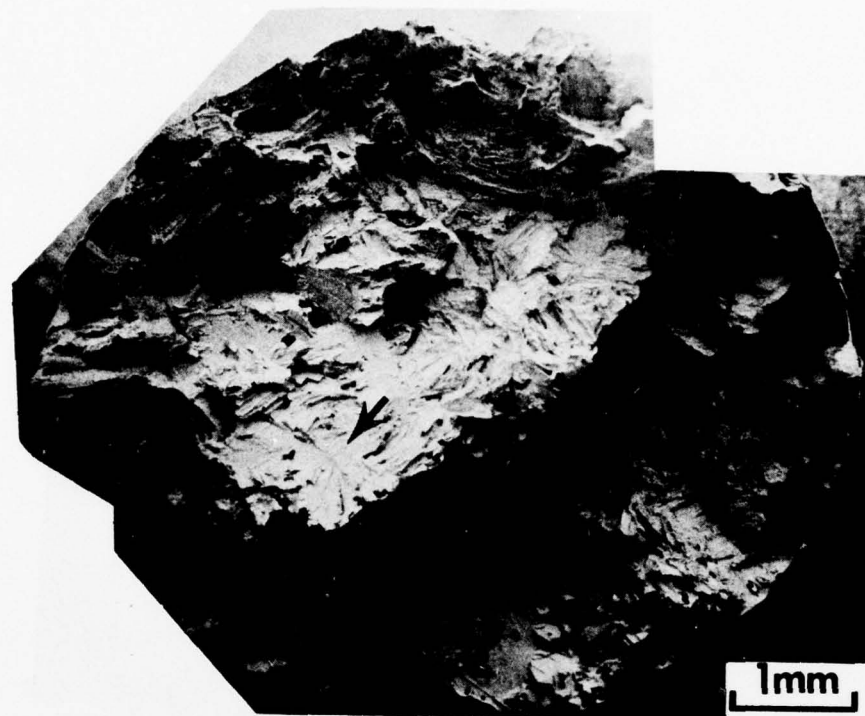


Figure 24 (a) General Appearance of the Fracture Surface of Specimen No. 25.  
(b) The Fracture Origin which is Located Between the Two Fan-Shaped Facets, showing the Small pore and the Brittle-Type Striations.

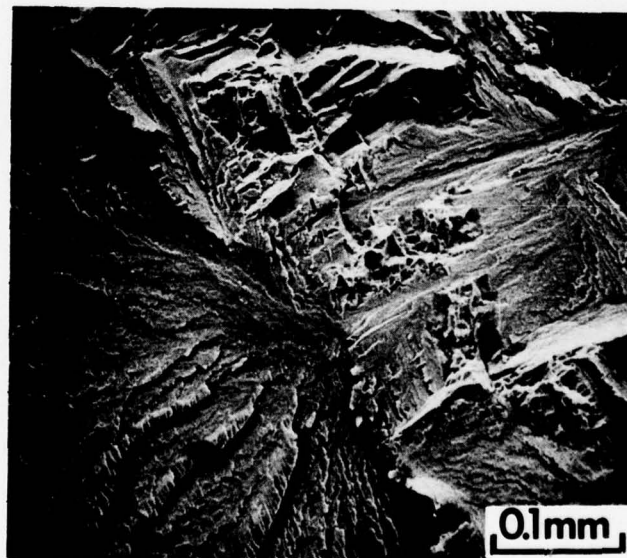
## (2) Fractures in Defect-Free Material

The general appearance of a dwell-tested fracture which does not involve a rosette defect is shown in Figure 25a for specimen #47. The fracture surface contains a macroscopic step, the fracture origin is located by an arrow near the edge of the upper step. It consists of a small facet and is marked by a "river" pattern as shown in Figure 25b. The appearance is similar to that of a rosette failure except that the small central pore is absent. No fatigue striations were observed on this fracture surface.

The general appearance of a normal fracture surface in a nondwell test is shown in Figure 26a for specimen #45. The location of the surface origin is indicated by an arrow. It is interesting to note the absence of a relatively large facet at the origin as those shown in previous fractures. The fatigue-propagation region around the fracture origin is relatively flat and contains cleavage-like facets on which fatigue striations were observed as shown in Figure 26b.



a



b

**Figure 25** (a) General Appearance of the Fracture of Specimen No. 47. The fatigue origin consists of a facet located at the edge of a step on the fracture surface.  
(b) Details of the Fatigue Origin. Small central pores characteristic of the rosette-type fracture were not observed.

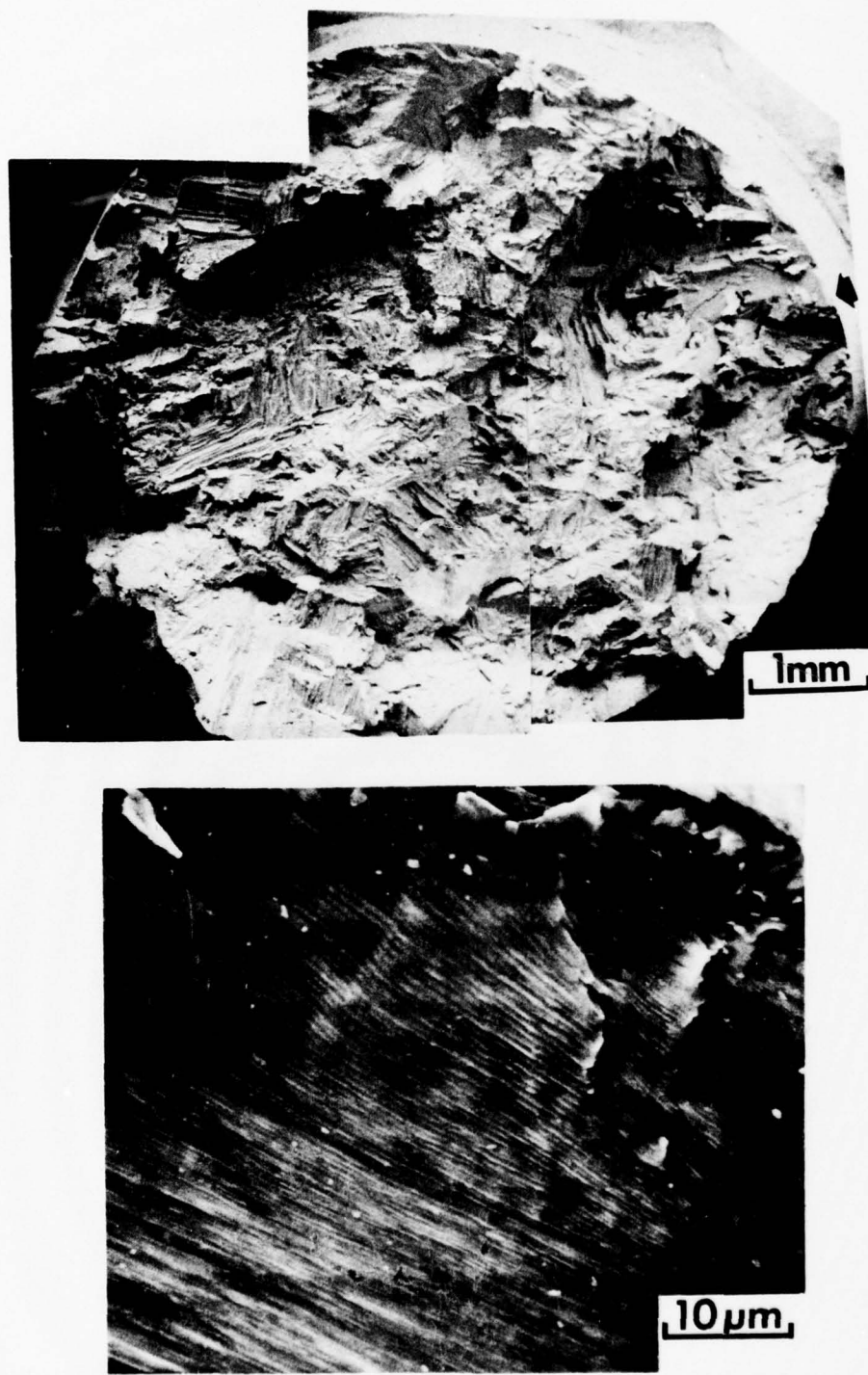


Figure 26 (a) The General Appearance of the Fracture Surface of Specimen No. 45. The surface crack origin is indicated by an arrow. Note the absence of large cleavage-like facets at the fracture origin.  
(b) Fatigue Striations Observed Near the Fracture Origin.

#### (4) Chemical Measurements of a Rosette Defect Origin

The contents of interstitials H, N and O determined from material located at the defect-prone area of the IMI685 forging are 48, 40 and 1138 ppm, respectively. These interstitial contents are within the specification for this material. The chemical analysis of Al, Zr, Mo, Si and C have been given by Eylon and Hall<sup>(5)</sup>. The bulk composition appears to be within normal specification limits. Two different techniques for analyzing local chemistry near rosette have been attempted. The techniques and the results obtained are given below.

The simplest method was to produce rosette-type of failure and then to directly analyze the defect location. Thus, one half of the "fish-eye" fracture origin of specimen #4 (Figures 19 and 20) was analyzed by Auger electron spectroscopy. The other half of the fracture was sectioned longitudinally through the central pore in the "fish-eye" and mounted for metallographic and electron microprobe examination by wave length dispersive technique. After the Auger and the electron microprobe examinations, the fracture surface and longitudinal section were studied by secondary ion microprobe technique using a  $^{32}\text{O}^+$  primary beam.

##### (a) Secondary Ion Microprobe Results

Determination of local chemistry on the fracture surface was found to be rather difficult even though the fracture origin (fish eye) is relatively flat. The low sputtered ion yield prevented meaningful ion image from being obtained. In addition, the non-reflectivity and varying focal depth also prevented exact correlations with scanning electron micrographs of the regions from which the secondary ions were generated. Consequently, data were obtained from the longitudinal section of the fracture only. These data were recorded after the contaminated surface layer was sputtered away. The relative changes in concentrations of several elements during sputtering are shown in Figure 27 which was obtained near the fracture origin. The relatively high initial concentrations of Na, Si and C are due to surface contamination. These decreased as steady stable levels of major constituents Ti and Al were approached. Current data taken after sputtering for one to two hours were reduced to the concentration listed in Table 7. These results may be compared meaningfully on a relative basis, but have known errors in an absolute sense. For instance, it has been established in previous studies that the data reduction scheme used produces high results for aluminum. On a relative basis, Table 6 indicates that the most significant difference between the fracture origin and the bulk is in the N contents, which is slightly over four times higher at the origin. Contrary to popular speculation, the H content at the origin was found to be lower than that in the bulk by a factor of two. Other differences are small but tend to indicate that the fracture origin is lower in alpha-stabilizing elements Al and C and higher beta stabilizing elements Fe and B.

## IMI-4 CROSS-SECTION (ORIGIN)

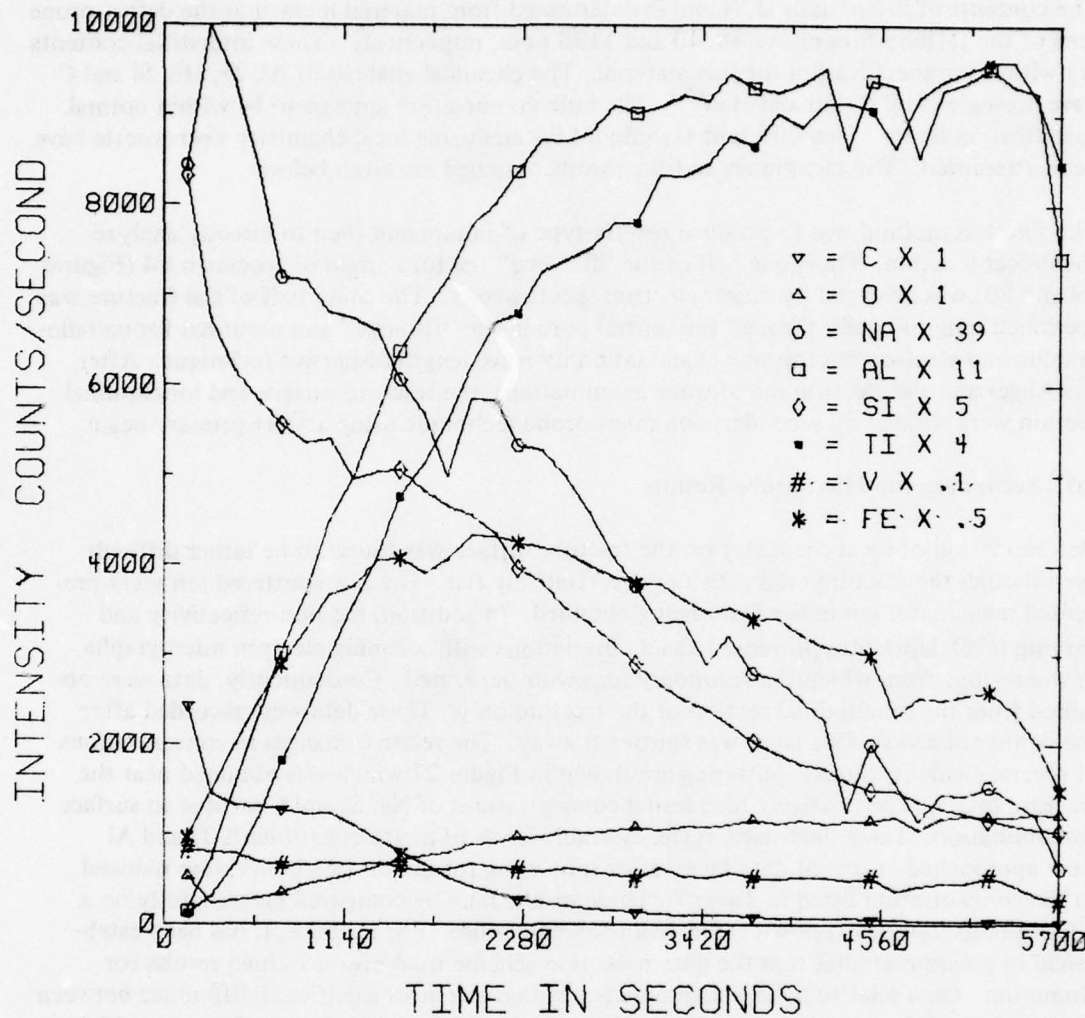


Figure 27 Change in Intensities of Several Elements as a Function of Sputtering Time. Determination of compositions at the 'fish eye' fracture origin and the bulk commenced after steady levels of major elements were observed.

**TABLE 7**  
**ION MICROPROBE ANALYSES OF**  
**ROSETTE FRACTURE IN IMI 685**

<u>Element</u>	<u>Bulk</u> (Atomic Percent)	<u>Near Origin</u>
Li	$3.6 \times 10^{-4}$	$3.0 \times 10^{-4}$
B	$1.46 \times 10^{-2}$	$2.55 \times 10^{-2}$
C	0.89	0.54
Al	30.91	23.49
Si	1.51	1.55
Fe	0.23	0.28
(Relative Ion Intensities Ti = 1.0)		
H	$2.5 \times 10^{-4}$	$1.1 \times 10^{-4}$
N	$2.7 \times 10^{-6}$	$11.2 \times 10^{-6}$
Cl	$7.7 \times 10^{-6}$	$10.7 \times 10^{-6}$

(b) Optical Metallography, Auger Spectroscopy and Electron Microprobe Analysis

Optical metallography (See Figure 22) revealed no microstructural anomaly at the "fish-eye" and electron microprobe results showed no detectable difference in chemistry at the fracture origin. However, the sensitivity of the electron microprobe technique for detecting interstitials is known to be poor, especially at low concentrations. Some of the results of the Auger electron spectroscopy (AES) are shown in Figure 28 which were obtained at the fracture origin before (Figure 28a) and after sputtering (Figure 28b). It can be seen that the sputtering reduced the concentrations of S, C and O which are common surface contaminants. The nitrogen peak coincides with one of the Ti peaks and therefore its concentration cannot be readily determined. No significant difference was observed between the AES results at the fracture origin and bulk material.

The second, more indirect, technique was based on the assumption that the defect contains either alpha or beta stabilizing contaminants of such concentrations that would result in observable local change in beta transus temperature. With an appropriate thermomechanical processing it was considered possible that a defect could be distinguished by microstructural variation. In order to produce a worked structure a compression specimen was fabricated with a C-scan identified defect located approximately at its center. The specimen was then isothermally compressed at 1830°F to 87% reduction in height, using boron

nitride as a lubricant. The compressed specimen was then polished to the expected defect locations. The transverse metallographic section was examined optically. This section was then heat-treated in vacuum at 1830°F for one hour and the heat-treated microstructure was studied optically and by wave-length dispersive electron microprobe technique.

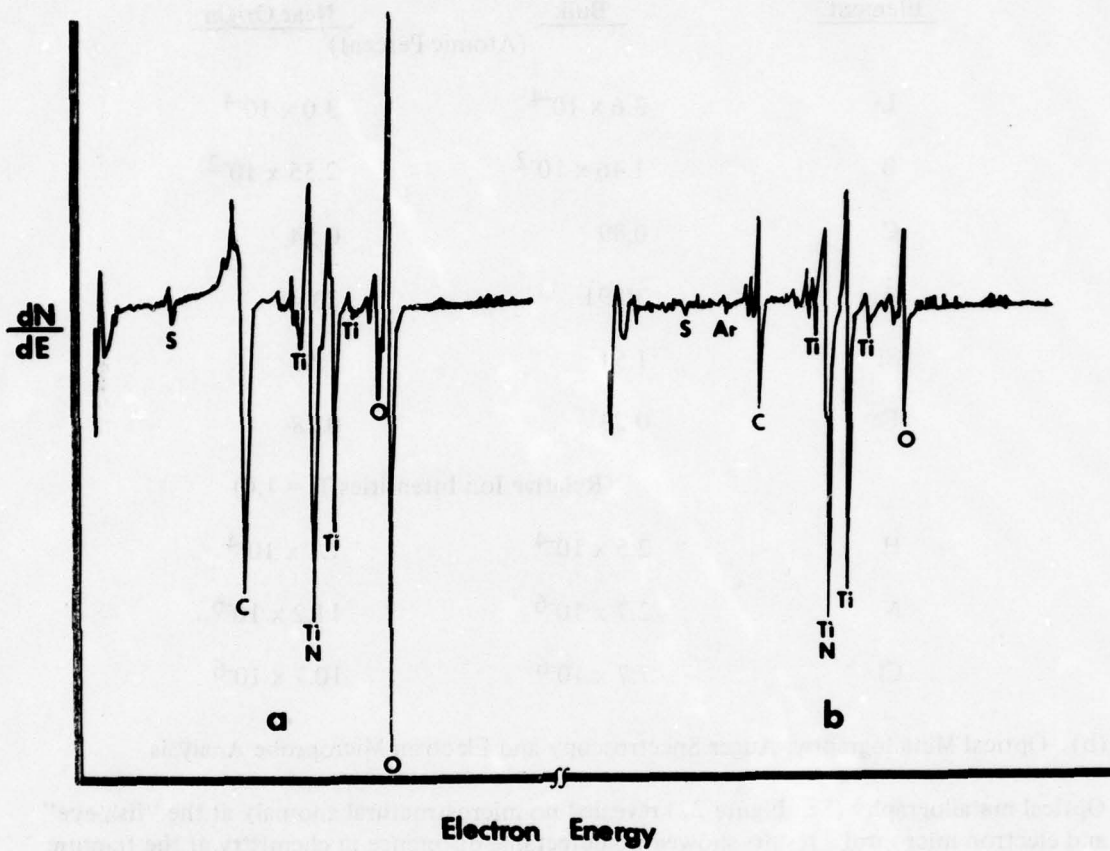
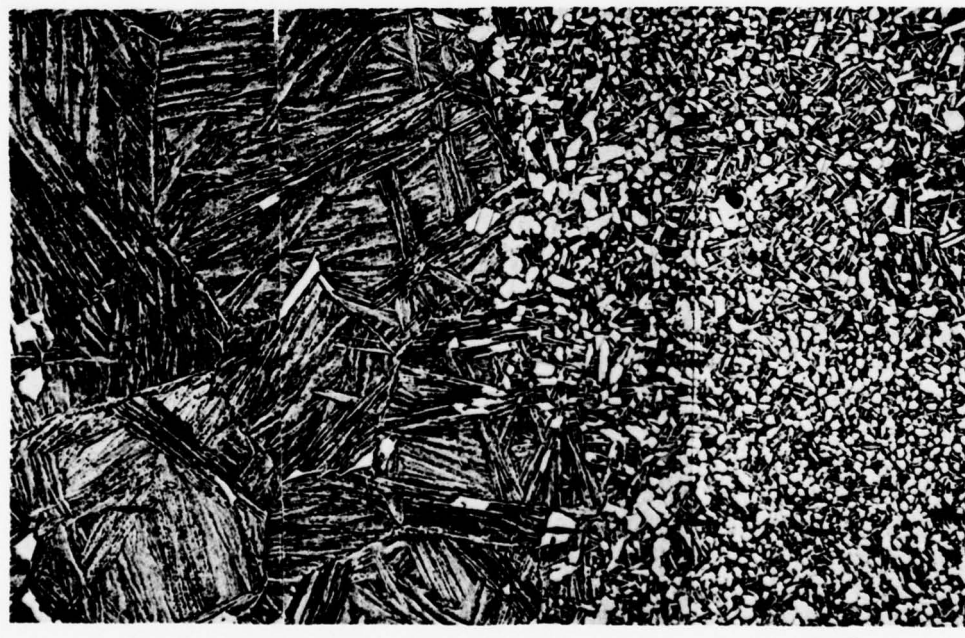


Figure 28 Auger Electron Spectrographs at the 'fish eye' Fatigue Origin  
 (a) Before sputtering  
 (b) After sputtering, note the decrease in C, O and S which are common surface contaminants.

The microstructure of the defect-containing specimen after isothermal compression at 1830°F to 87% reduction in height is shown in Figure 29. Recrystallization has occurred heterogeneously throughout the sample, and revealed no clear-cut memo structural differences at the expected defect site. Although additional recrystallization occurred when the compressed specimen was heat-treated at 1830°F for one hour, many localized areas remained unrecrystallized. The microstructure after the heat treatment is reminiscent of beta flecked material described in the second section of this report. The results of the electron microprobe analysis of the recrystallized and unrecrystallized regions (Figure 30) are shown in Table 8.



Figure 29 Microstructure Near the Expected Rosette Defect Site in an IMI 685 Specimen Which had been Isothermally compressed at 1830°F.



0.2 mm

Figure 30 The Microstructure Shown in Figure 29 After Additional Recrystallization Treatment at 1830°F for 1 Hour.

TABLE 8  
ELECTRON MICROPROBE ANALYSES OF FORGED IMI 685

Element	No. of Counts in 100 Sec.	
	Equiaxed Microstructure*	Acicular Microstructure*
Al	39920	36470
Zr	2420	2410
Mo	693	721

\*See Figure 30

The data represent relative compositions averaged over an area of  $10^{-4}$  cm<sup>2</sup>. Although the differences between the recrystallized and unrecrystallized regions are small, a definite trend can be detected. The unrecrystallized region shows higher concentrations of the beta stabilizing element Mo and lower concentrations of the alpha stabilizing elements Al and Zr than the recrystallized region. Unfortunately this experiment did not provide any additional information on the chemistry of a rosette-type defect.

#### (5) Fatigue Testing at 400°F

Seven specimens were LCF tested at 400°F at a stress range of 30-100 ksi using either a dwell cycle (12 cph) or a non-dwell cycle (12 cpm). The results are summarized in Table 9. All four specimens that had sonic indications in their gage sections failed with very low cyclic lives at either test frequency. Based on the one defect-free specimen that was dwell tested, it appears that the dwell debit is smaller at 400°F than that observed in 70°F tests.

All short life specimens failed from subsurface origins which did not appear to show the characteristic features of a rosette-type failures observed in room temperature tests. A typical fracture for a defect-containing specimen is shown in Figure 31a in which the apparent fatigue origin is indicated by an arrow. It can be seen that the scale of the cleavage facets are much larger than those observed in tests at 70°F. A longitudinal section of the fracture surface, shown in Figure 31b, shows that the cracks cut across several colonies within a prior beta grain. In fact the facet size appears to be set by the latter microstructural dimension.

In contrast, cracks in specimens that failed with long lives were surface nucleated. Figure 32a shows the general fracture appearance. It can be seen that the facets are smaller than that of the defect-containing specimen. The smaller facet size appears to correlate with the dimensions of alpha colonies and prior beta grain shown in Figure 32b.

**TABLE 9**  
**IMI 685 400°F, 30-100 KSI LCF TESTS**

S/N <sup>o</sup>	C-Scan Indication	Cycles to Failure	Surface	Initiation Site	
				Subsurface	Rosette Defect
12 cph					
21	I	6		Yes	No
23	I	39		Yes	No
43	NI	4,462+			
48	I	1		Yes	No
12 cpm					
10	NI	7,510	Yes		No
44	NI	48,160	Yes		No
49	I	1		Yes	No

I Indication

NI No indication

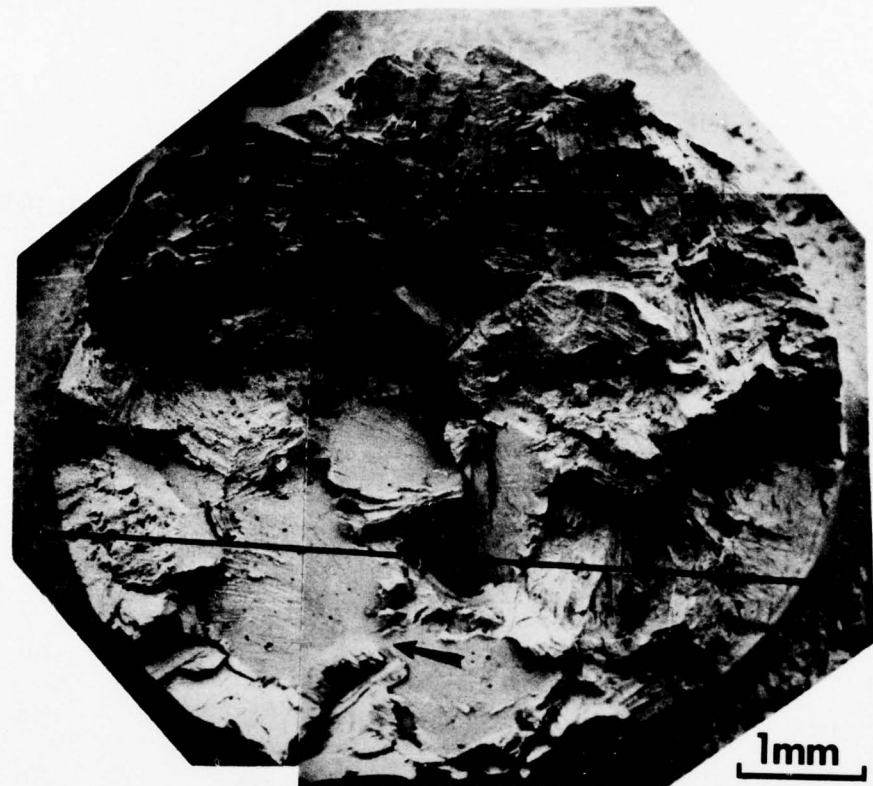
+ Test discontinued after 4,462 cycles with no failure

o Specimen Number

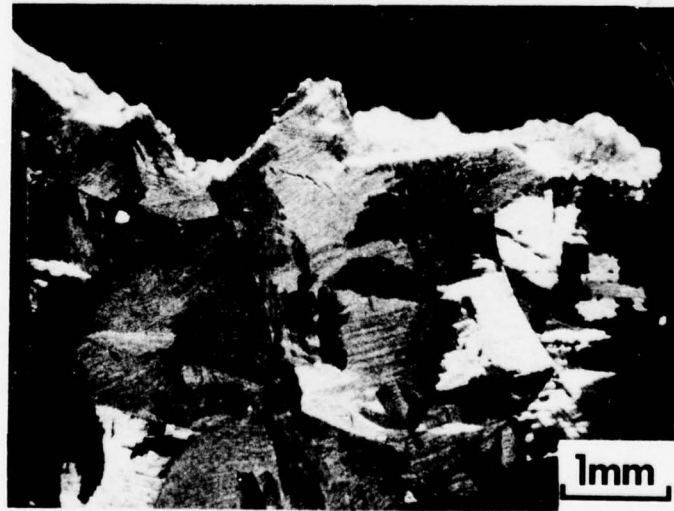
#### c. Ancillary Experiments

It was clear from the experiments described in the previous sections that the 70°F fatigue results obtained on IMI 685 were very similar to those observed by Eylon and Hall<sup>(5)</sup>. However several areas pertinent to providing an explanation of this behavior pattern required clarification. These areas can be divided into three groups as follows:

- 1) Cracking rates that occurred in IMI 685 under dwell test conditions could be very high. These rates needed to be determined and compared with data from other tests and behavior in other alloys.
- 2) The relationship between the seeded defects experiments on Ti-6Al-4V, the higher nitrogen content at a rosette origin and the rosette failure in IMI 685 required elucidation.
- 3) It was unclear if the remarkable fatigue characteristics observed in IMI 685 were unique or if they occurred in other alpha:beta titanium alloys. Cracking behavior from naturally occurring flaws and also dwell-testing effects in non-defective material were areas of interest.

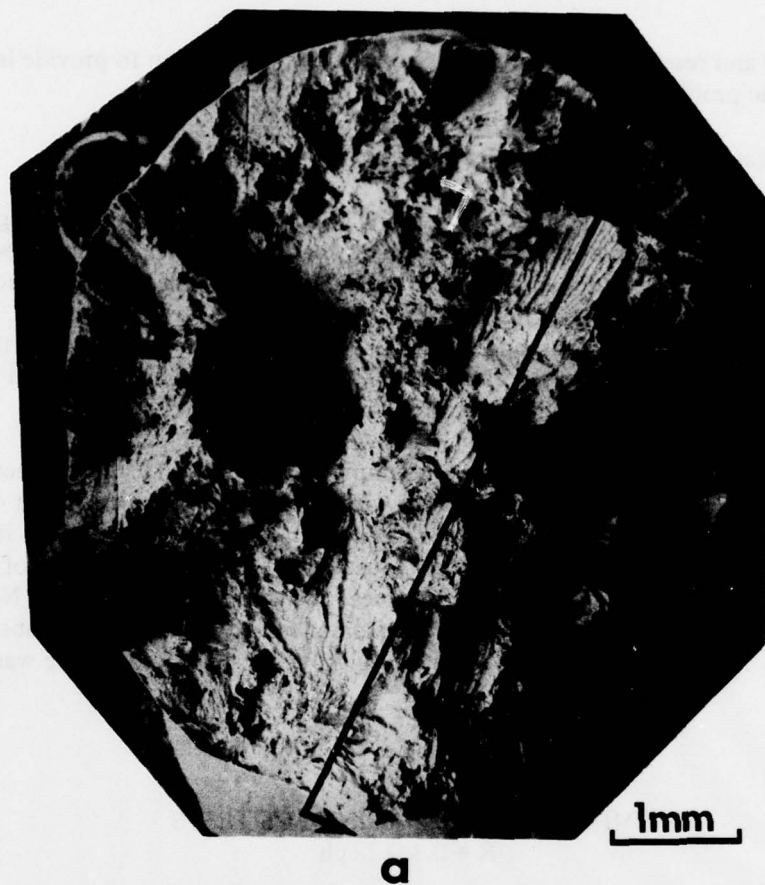


a



b

Figure 31 (a) General Appearance of the Fracture of Specimen No. 49 Tested at 400°F. The apparent fracture origin is indicated by an arrow.  
(b) A Longitudinal Section Along the Line Indicated in (a), Showing the prior  $\beta$  grain size adjacent to the fracture surface.



a



b

Figure 32 (a) General Appearance of the Fracture of Specimen No. 44 Tested at 400°F.  
(b) A Longitudinal Section Along the Line Indicated in (a), Showing the Prior  $\beta$  Grain Size Adjacent to the Fracture Surface.

The experiments and results described in this Section were undertaken to provide insight into these specific problems.

(1) Crack Nucleation and Propagation Rates in IMI 685

Two methods were employed to obtain information on the nucleation and cracking behavior of IMI 685. In the first group of experiments defective and defect-free specimens were subjected to fatigue cycling under an increasing load. Specifically the stress on specimens was increased 10% after 1000 cycles imposed at a frequency of 12 cycles per hour. The initial maximum stress level was 80 ksi and a R value of 0.3 was used. It was hoped that at such stress increase the position of the crack front would be marked and thus both the onset of cracking and local (average) cracking rates could be determined.

The results of these uploading experiments are summarized in Table 10. The defect-free specimen (#9) failed after four stress increments with a cumulative fracture life of 4,500 cycles. The general appearance of the fracture is shown in Figure 33, from which it can be seen that fatigue initiated at a subsurface origin located at the upper left quarter of the figure. The appearance of the fracture surface is typical of dwell-tested specimens. Neither crack-front marking resulting from stress increments nor fatigue striations were observed. Results from the second specimen were equivalent although a slightly lower life was observed.

TABLE 10  
IMI 685 70°F UPLOADING LCF TESTS  
R = 0.3, 12 cph

Cycles	Max. Stress (Ksi)	Cumulative Fracture Life (Cycles)		
		Specimen No. 9	Specimen No. 20	Specimen No. 26
1 - 1000	80	*	*	*
1001 - 2000	88	*	*	*
2001 - 3000	97	*	2600	*
3001 - 4000	107	*		*
4001 - 5200	117	4900		*
5201 - 6260	120			6260

\*No failure occurred after 1000 cycles at the stress indicated.

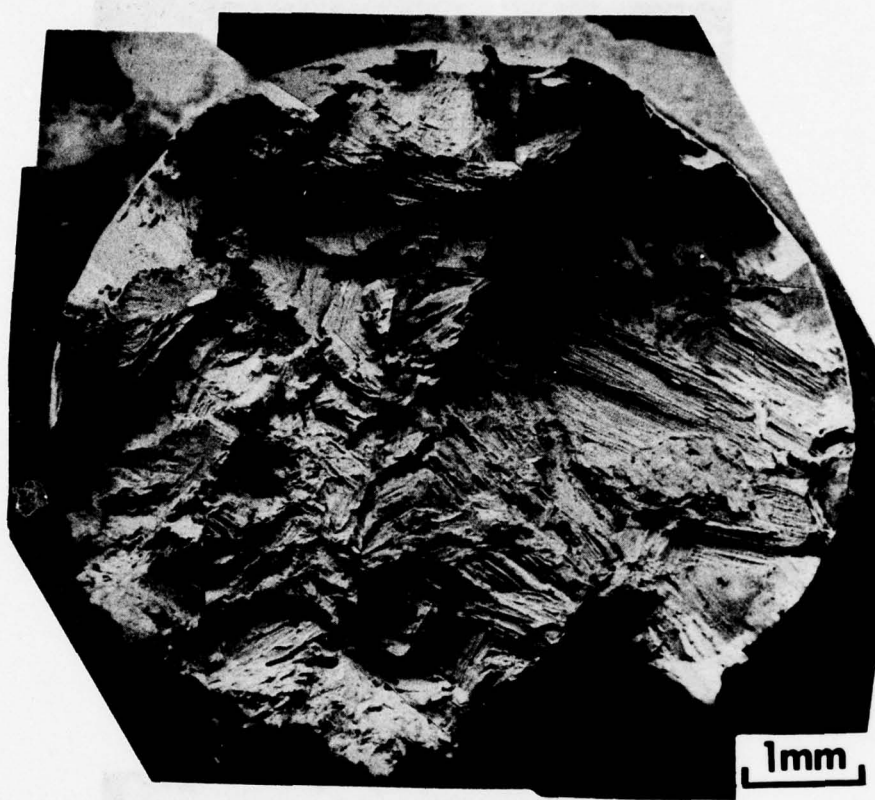
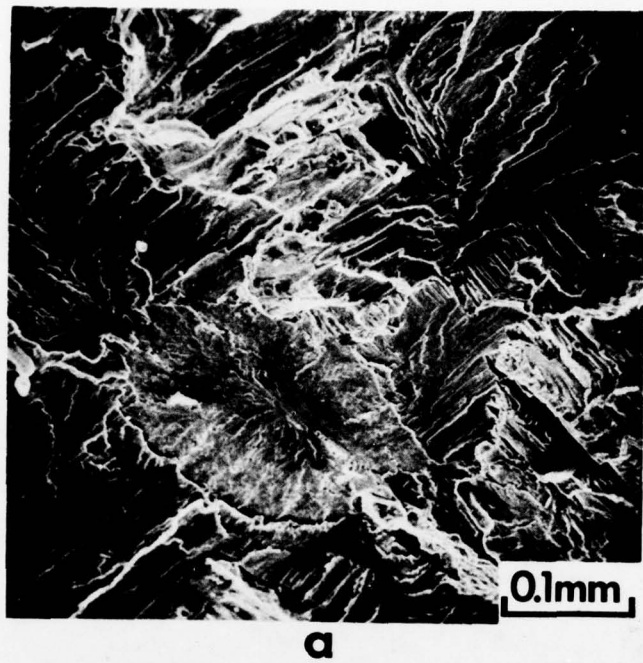


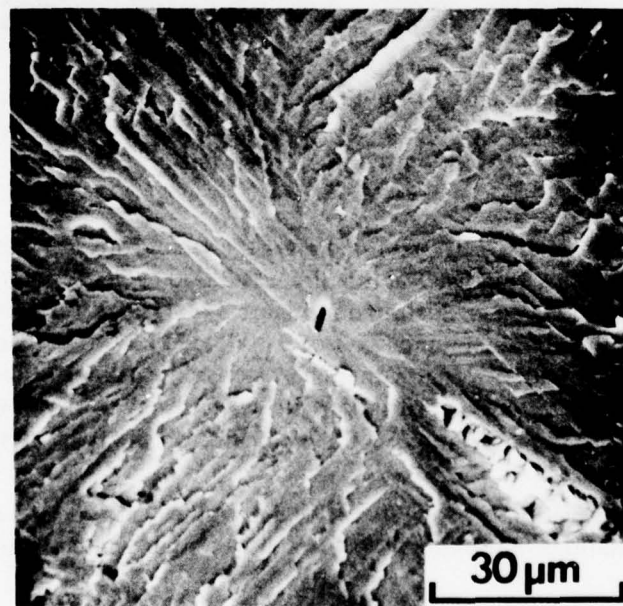
**Figure 33** The General Appearance of the Fracture of Specimen No. 9. The stress had been incrementally increased four times before fraction. No crack-front marking due to the uploading is apparent on the fracture surface.

The defect containing specimen (#20) fractured after the second stress increment at a maximum stress of 97 ksi. The cumulative fracture life was 2,600 cycles. Fracture initiated at a subsurface rosette defect which is illustrated in Figure 34. The fracture origin consists of an elliptical facet with major and minor axes of 0.009" and 0.006". Near the center of this facet is a small pore 0.00016" long. Other characteristic features of the rosette fracture, "river pattern" and "brittle-type" striations are again observed. However, neither crack-front markings nor fatigue striations could be located on the fracture surfaces.

Although the crack propagation rates could not be determined from results of any of the above tests, fatigue striations observed in dwell-tested will be presented later.



a



b

Figure 34 (a) General Appearance of the Fracture Near the Rosette Crack Origin Observed in Specimen No. 20.  
(b) Details of the Rosette Crack Origin Showing the Characteristic Central Pore and the Brittle-Type Striations.

In the second technique which is applicable to surface cracks only, nucleation was monitored by zyglo inspection and the crack propagation was recorded by surface replication. Using this technique crack nucleation and propagation has been studied at maximum stresses of 120 ksi and 126 ksi at 12 cpm. The nucleation of a crack in a dwell test was also monitored in this test, a maximum stress of 120 ksi was used. One of the interesting effects of test frequency on fatigue crack nucleation is already obvious from Table 5 in which it can be seen that the fracture origins of all dwell-tested specimens are invariably subsurface. This leads to major problems in assessing crack growth characteristics of dwell-tested specimens. The fatigue origins in the 12 cpm tests can be either surface nucleated or subsurface nucleated. The results of surface inspection methods of crack monitoring are summarized in Table 11 and will now be described in detail.

TABLE 11

CRACK NUCLEATION AND PROPAGATION  
IMI 685 70°F LCF TESTS R = 0.3

Specimen No.	Max. Stress (Ksi)	Cycles to Crack Indication (Frequency)	Crack Size (in.)	Propagation Life (Frequency)	Fracture Origin
24	126	10,470 (12 cpm)	0.032	170 (12 cpm)	Surface
25	126	840 (12 cpm)	0.016	20 (12 cph)	Subsurface Rosette
45	120	8,500 (12 cpm)	1 pp	16,500 (12 cpm)	Surface
46	120	24,000 (12 cpm)	3 pp*	131 (12 cph)	Subsurface
47	118.5	---	---	552 (12 cph)	Subsurface

--- No data

\* No correlation of these 'pin-point' cracks (crack lengths of 0.005" to 0.015") to the final fracture.

In the initial test a specimen (#24) was tested at a maximum stress of 126 ksi, R = 0.3 and 12 cpm. After the initial 9670 cycles no crack was detected but at the next inspection interval (10,400 cycles) a crack 0.032" in length was found. This crack propagated to fracture after 170 additional cycles and before the next surface replica was due. Thus it is clear that a major portion of the fracture life was spent in nucleating a crack although the exact nucleation event was not measured. Fatigue striations were observed on the fracture surface of this specimen and details of the measurements made will be given below.

A second specimen (#45) was tested at a stress range of 36 to 120 ksi and at a frequency of 12 cpm. A "pin-point" crack was detected after 8,500 cycles and the fracture life of the specimen was 25,000 cycles. The rate of propagation of the surface crack, as determined from surface replicas taken during the test, are given in Figure 35. From the slope of the crack length versus cycle plot and the corresponding  $\Delta K$  values computed using the semi-circular crack approximation, curve D in Figure 36a is obtained. For comparison, the crack propagation data obtained by Rolls Royce (8) (Curves A and B) and by the Metcut (6) (Curve C) are also shown.

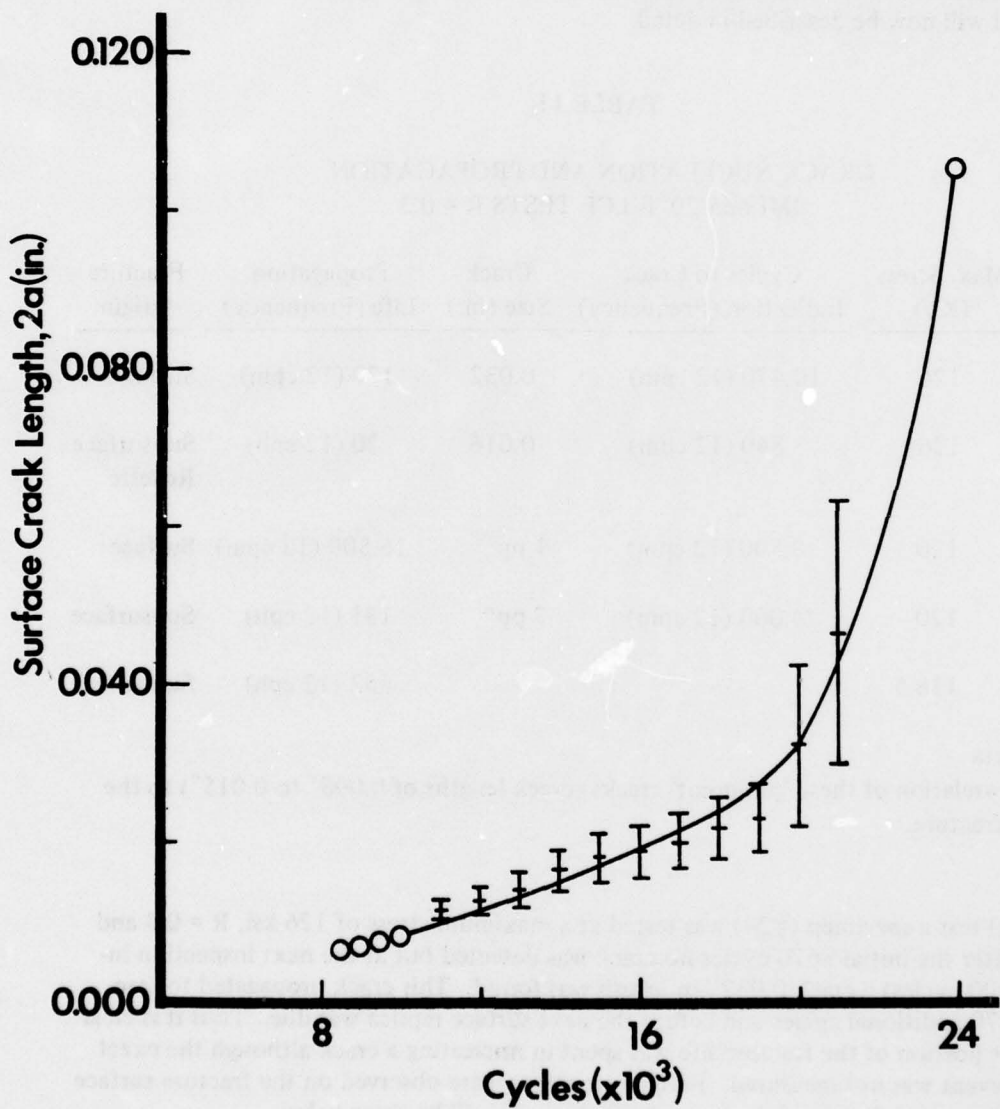


Figure 35 Surface Crack Length,  $2a$  Versus Number of Cycles for Specimen No. 45

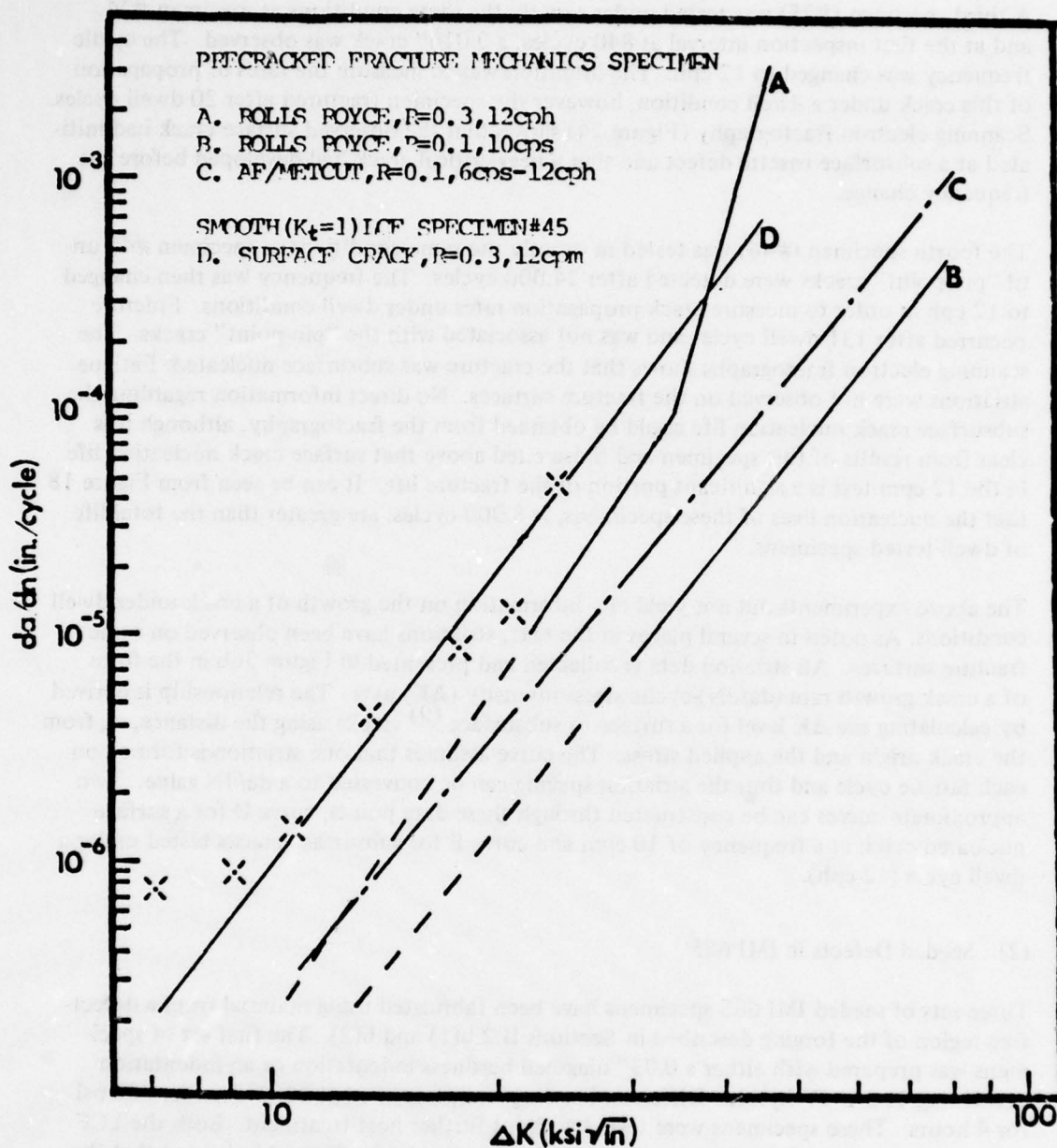


Figure 36(a) Crack Propagation Results as Determined by Measurement of a Surface Crack on a Smooth ( $K_t=1$ ) LCF Specimen (Curve D) Compared With Those Determined From Fracture Mechanics Specimens (Curve A, B, and C).

A third specimen (#25) was tested under exactly the same conditions as specimen #24 and at the first inspection interval at 840 cycles, a 0.016" crack was observed. The cyclic frequency was changed to 12 cph. The intention was to measure the rates of propagation of this crack under a dwell condition, however the specimen fractured after 20 dwell cycles. Scanning electron fractography (Figure 24) shows that the observed surface crack had initiated at a subsurface rosette defect and that a near-critical crack had developed before the frequency change.

The fourth specimen (#46) was tested in exactly the same conditions as specimen #45 until "pin-point" cracks were detected after 24,000 cycles. The frequency was then changed to 12 cph in order to measure crack propagation rates under dwell conditions. Fracture occurred after 131 dwell cycles and was not associated with the "pin-point" cracks. The scanning electron fractographs shows that the fracture was subsurface nucleated. Fatigue striations were not observed on the fracture surfaces. No direct information regarding the subsurface crack nucleation life could be obtained from the fractography, although it is clear from results of this specimen and those cited above that surface crack nucleation life in the 12 cpm test is a significant portion of the fracture life. It can be seen from Figure 18 that the nucleation lives of these specimens, > 8,000 cycles, are greater than the total life of dwell-tested specimens.

The above experiments did not yield any information on the growth of a crack under dwell conditions. As noted in several places in the text, striations have been observed on some fracture surfaces. All striation data is collected and presented in Figure 36b in the form of a crack growth rate ( $da/dN$ )-cyclic stress intensity ( $\Delta K$ ) plot. The relationship is derived by calculating the  $\Delta K$  level for a surface or subsurface<sup>(9)</sup> cracks using the distance,  $a$ , from the crack origin and the applied stress. The curve assumes that one striation is formed on each fatigue cycle and thus the striation spacing can be converted to a  $da/dN$  value. Two approximate curves can be constructed through these data points, curve D for a surface nucleated crack at a frequency of 10 cpm and curve E for subsurface cracks tested under a dwell cycle (12 cph).

## (2) Seeded Defects in IMI 685

Three sets of seeded IMI 685 specimens have been fabricated using material from a defect-free region of the forging described in Sections II.2.b(1) and b(2). The first set of specimens was prepared with either a 0.03" diagonal hardness indentation or an indentation containing Ti-6Al-4V hydride. Diffusion bonding was performed at 1800°F under 500 psi for 4 hours. These specimens were tested without further heat treatment. Both the LCF and the appearance of the fracture surfaces of specimens in the first set indicated that the diffusion bonds were inadequate. Consequently, a higher temperature and pressure were used for the diffusion bonding of the second and third sets of specimens, specifically 1850°F for 4 hours at 600 psi. The indentation size was held constant at 0.03" in both the second and third sets. Before specimen machining the bonded blocks were given a beta heat treatment of 1922°F for 1 hour followed by an oil quench and an age at 1076°F for 8 hours, air cool. As will be shown below this heat treatment resulted in a microstructure that is not equivalent to that in the center section of the forging used for the experiments described in Section 2.b. This can be traced to the smaller section size of the diffusion bonded

block and consequently faster cooling rate compared with that in the forging. In order to produce the same structure, selected specimens in the third set were reheat-treated, under vacuum, at 1950°F for 1 hour followed by cooling in an argon atmosphere. Ti-6Al-4V hydride and TiN were used as contaminants in the second set, TiN was used in the third set.

All the seeded IMI 685 specimens were tested at a maximum stress of 110 ksi with combinations of stress ratio ( $R$ ) and frequency of either  $R = 0, 20$  cpm, or  $R = 0.3, 12$  cph. These conditions were selected to allow direct comparison of data with other tests on IMI 685.

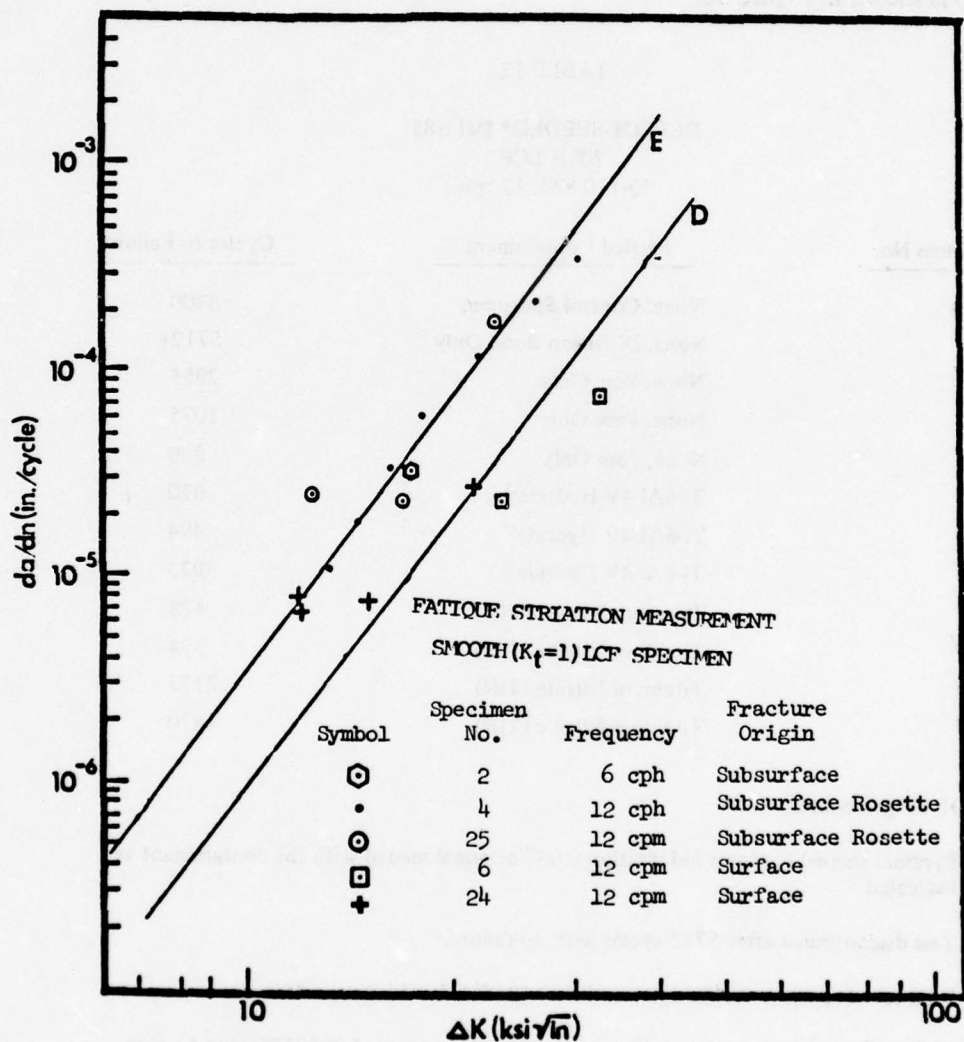


Figure 36(b) Crack Propagation Results as Determined by Fatigue Striation Measurement on Smooth ( $K_t=1$ ) LCF Specimens.

The LCF results of the three sets of seeded specimens are given in Tables 12 and 13 for tests at 12 cph and 12 cpm, respectively. Fracture initiated at the seeded pores in most cases the one exception is noted below. The microstructure of the specimens used in the major portion of tests of the second and third sets is illustrated in Figure 37a. It can be seen that the microstructure consists of a mixture of colony and Widmanstatten structures. As shown in Figure 37b the microstructure of the reheat-treated specimens in the third set consists of colony structure equivalent to that in the center region of the forging. These microstructural differences are reflected both in the fracture morphology and in the LCF behavior. The appearance of the fracture surface of a specimen tested under dwell conditions (Specimen #41) is shown in Figure 38.

TABLE 12

DEFECT-SEEDED\* IMI 685  
70°F LCF  
33-110 KSI, 12 cph

<u>Specimen No.</u>	<u>Seeded Contaminant</u>	<u>Cycles to Failure</u>
Ref. 4	None, Control Specimen	8700
42 <sup>(3)</sup>	None, Diffusion Bond Only	5712+
31 <sup>(3)'</sup>	None, Pore Only	2955
12 <sup>(1)</sup>	None, Pore Only	1075
13 <sup>(1)</sup>	None, Pore Only	900
16 <sup>(1)</sup>	Ti-6Al-4V Hydride <sup>o</sup>	610
19 <sup>(1)</sup>	Ti-6Al-4V Hydride <sup>o</sup>	494
28 <sup>(2)</sup>	Ti-6Al-4V Hydride <sup>o</sup>	3033
34 <sup>(2)</sup>	Titanium Nitride (TiN)	478
38 <sup>(3)'</sup>	Titanium Nitride (TiN)	394
40 <sup>(3)</sup>	Titanium Nitride (TiN)	2177
41 <sup>(3)</sup>	Titanium Nitride (TiN)	1470

<sup>o</sup> Hydrogen content 1.2%

\* Pyramid-shaped hardness indentation 0.03" diagonal seeded with the contaminant as indicated.

+ Test discontinued after 5712 cycles with no failure.

(1) First set of specimens diffusion bonded at 1800°F for 4 hours at 500 psi.

(2) and (3) Second and third sets of specimens diffusion bonded at 1850°F for 4 hours at 600 psi. Microstructure shown in Figure 37a.

(3)' Third set of specimens reheat treated to produce microstructure shown in Figure 37b.

TABLE 13

DEFECT-SEEDED\* IMI 685  
 70°F LCF  
 0-110 KSI, 12 cpm

Specimen No.	Seeded Contaminant	Cycles to Failure
6	None, Control Specimen	22,560
7	None, Control Specimen	33,950
15 <sup>(1)</sup>	None, Diffusion Bond Only	7,650
29 <sup>(2)</sup>	None, Diffusion Bond Only	12,170
11 <sup>(1)</sup>	None, Pore Only	6,090
14 <sup>(1)</sup>	None, Pore Only	6,110
33 <sup>(2)</sup>	None, Pore Only	9,450
17 <sup>(1)</sup>	Ti-6Al-4V Hydride <sup>o</sup>	9,160
27 <sup>(2)</sup>	Ti-6Al-4V Hydride <sup>o</sup>	7,270+
30 <sup>(2)</sup>	Ti-6Al-4V Hydride <sup>o</sup>	4,233
35 <sup>(2)</sup>	Titanium Nitride (TiN)	16,326
36 <sup>(2)</sup>	Titanium Nitride (TiN)	4,586
32 <sup>(2)</sup>	Titanium Nitride (TiN)	12,460
39(3)'	Titanium Nitride (TiN)	22,700

o Hydrogen content 1.2%

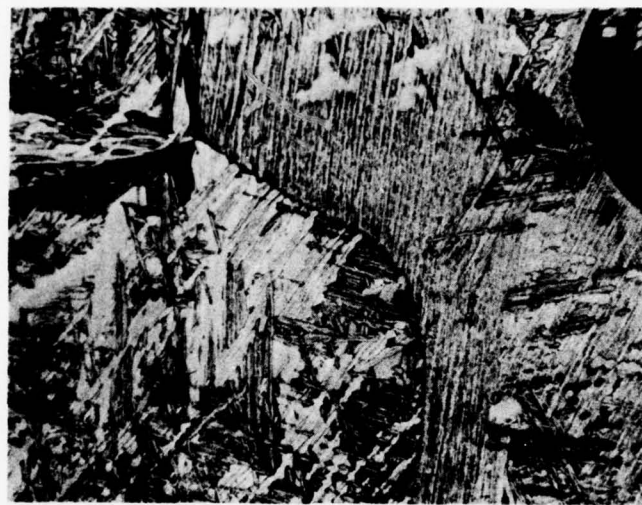
\* Pyramid-shaped hardness indentation 0.03" diagonal seeded with the containment as indicated.

+ Fracture caused by accidental overloading.

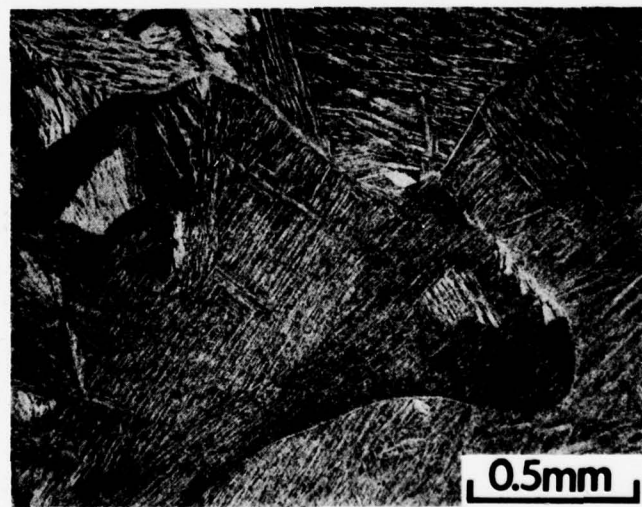
(1) First set of specimens diffusion bonded at 1800°F for 4 hours at 500 psi.

(2) Second set of specimens diffusion bonded at 1850°F for 4 hours at 600 psi.  
 Microstructure shown in Figure 37a.

(3)' Third set of specimen reheat treated to produce microstructure shown in Figure 37b.  
 Tested at 33-110 ksi, 12 cpm.



**a**



**b**

**Figure 37** (a) Microstructure of the Second and Third Sets of Specimens  
(b) Microstructure of the Third Set of Specimens After a Slower Cool From the Solution Temperature

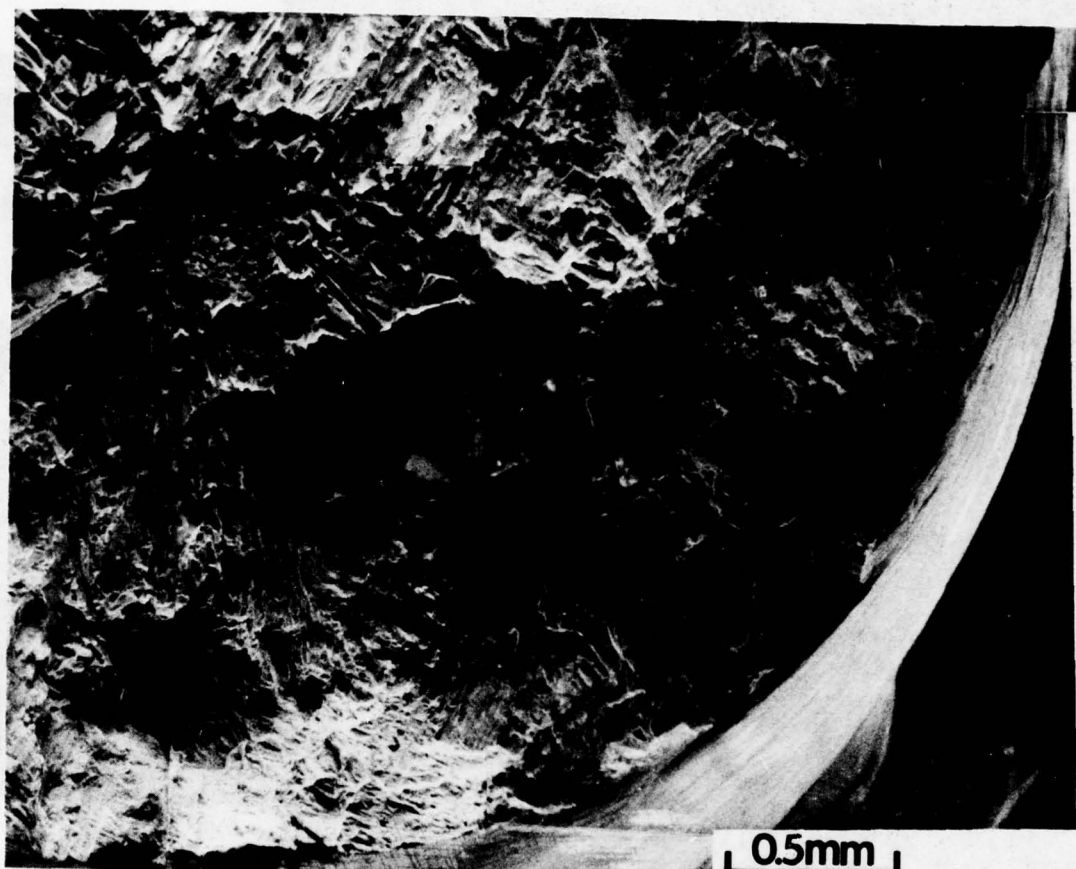


Figure 38 The Appearance of the Fracture Surface of the Nitrided-Seeded Specimen No. 41. The microstructure is given in Figure 37a. Fracture initiated at the seeded pore which can be located at the upper left corner.

Fracture initiated at the TiN-seeded pore (upper left corner of the Figure) near the center of the gage area. The morphology of the fracture around the pore is relatively flat and consists of small rectangular facets. Beyond this region which is approximately 0.07" diameter, the fracture appears to be typical of those resulting from the dwell test. By contrast, large cleavage-like facets are observed around the TiN-seeded pore in the specimen with coarser microstructure (#38) as shown in Figure 39. Except for the absence of the "fish-eye" the appearance of the fracture is typical of that in the rosette failure. A longitudinal section through the seeded pore revealed no detectable microstructural change due to the introduction of hydride or nitride. This is illustrated for the case of an indentation containing nitride in Figure 40. The fracture appearance of the dwell-tested specimen with coarse microstructure and containing a pore (Specimen #31) is shown in Figure 41a. The pore is indicated by an arrow at the upper right quarter of this Figure and is shown in higher magnification in Figure 41b, and is seen to be located at an overload fractured region.

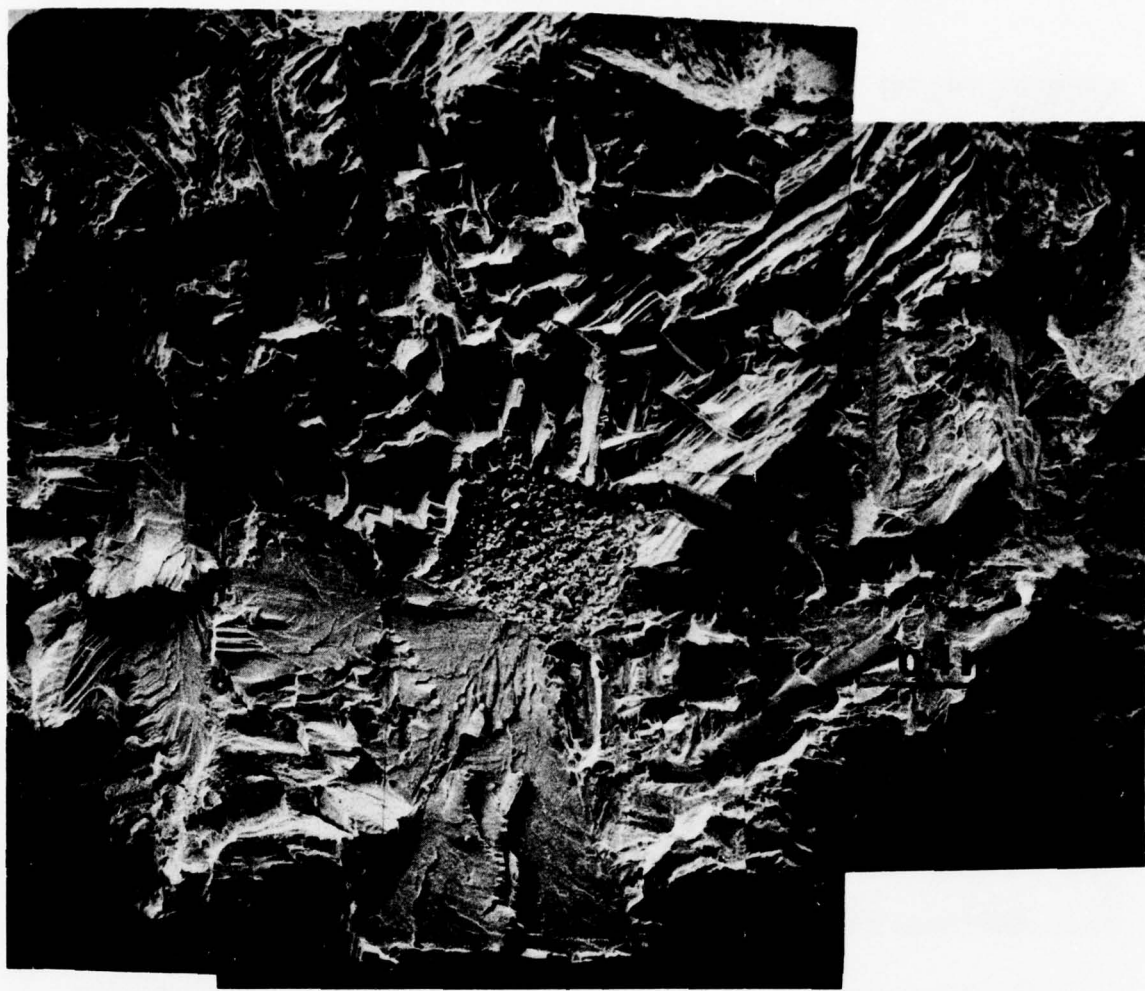
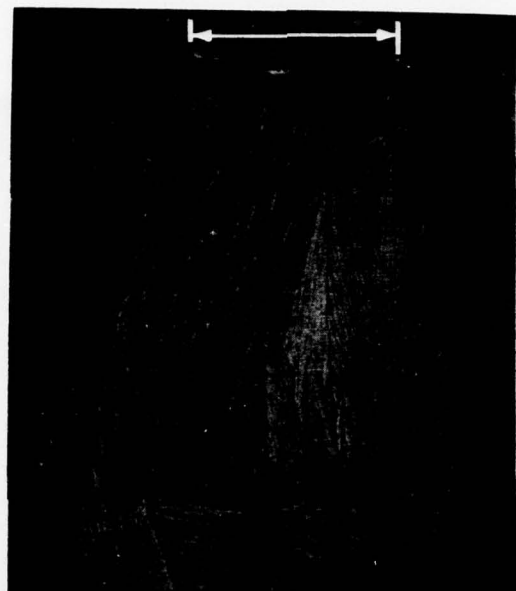
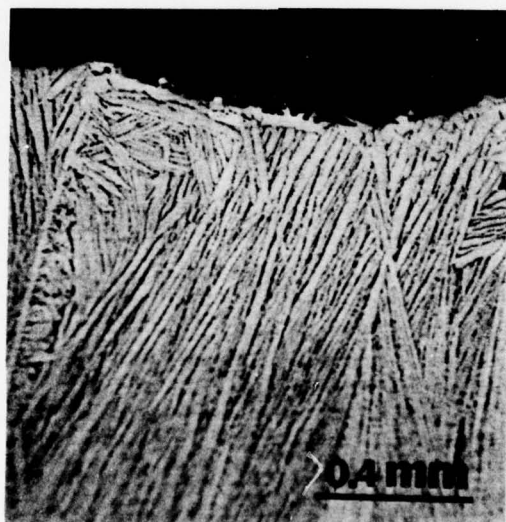


Figure 39 Fracture Appearance of the Dwell-Tested Specimen (No. 38) Which Contains A Nitride-Seeded Pore

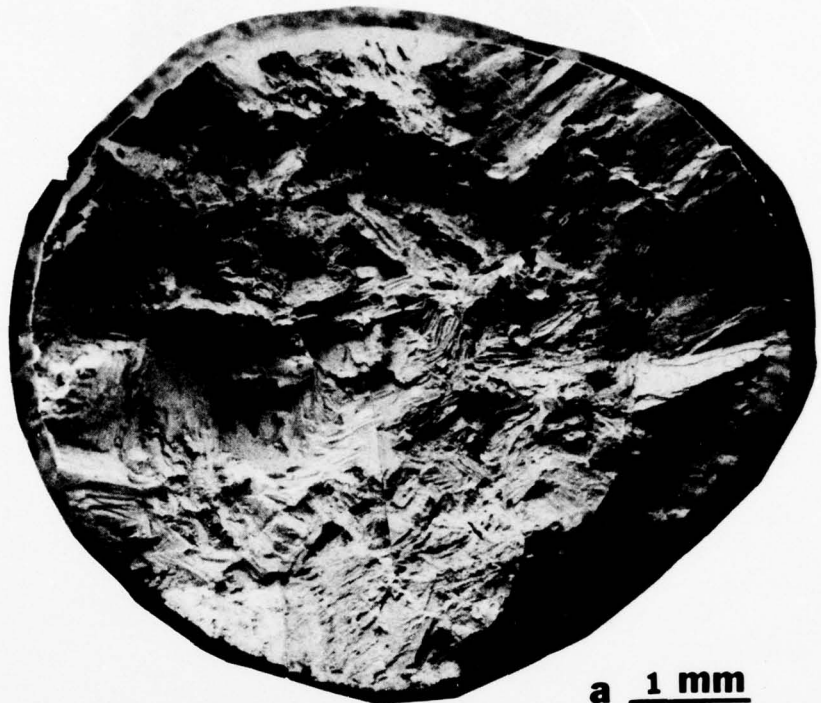


**a**



**b**

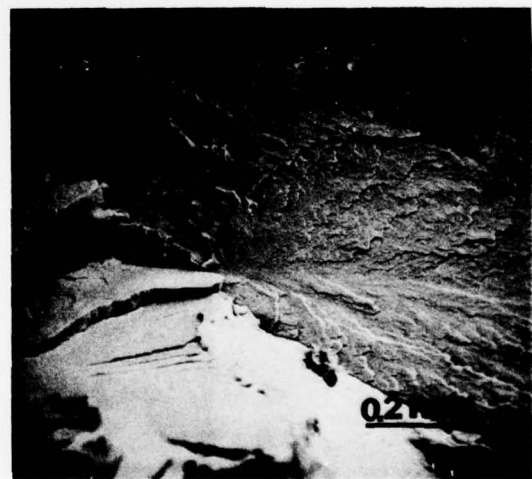
**Figure 40** (a) Microstructure of a Longitudinal Section Through the Nitride-Seeded Pore (Indicated By an Arrow) in Specimen No. 38.  
(b) Microstructure of the nitride-seeded Pore Shown in Higher Magnification.



a 1 mm



b



c

Figure 41 (a) General Fracture Appearance of the Dwell-Tested Specimen (No. 31) Which Contains a Clean Pore. The pore (indicated by the upper arrow) is partially exposed and is located at the overload failed region.  
(b) The Clean Pore Shown at Higher Magnification.  
(c) The Fracture Origin which is Indicated by the Lower Arrow in (a).

The fatigue fracture origin which is indicated by an arrow at the lower left quarter of Figure 41a. As shown in higher magnification in Figure 41c, the fracture origin consists of a cleavage-like facet on which "river markings" can be observed. Large cleavage-like facets, typical of dwell-tested specimens, are observed around the crack origin. The fracture surfaces of specimens tested at a higher frequency exhibited a somewhat different topography, an example is shown in Figure 42. This specimen (#39) had a colony type structure and thus can be compared with Figure 39. The increased roughness of the fracture surface is evident for the high frequency test and the overall appearance is similar to that of defect-free specimens tested at the same condition, see Figure 26a. However for specimens that failed from the surface origin striations are observed, while no striations were found in the present case of cracking from a subsurface nucleus.

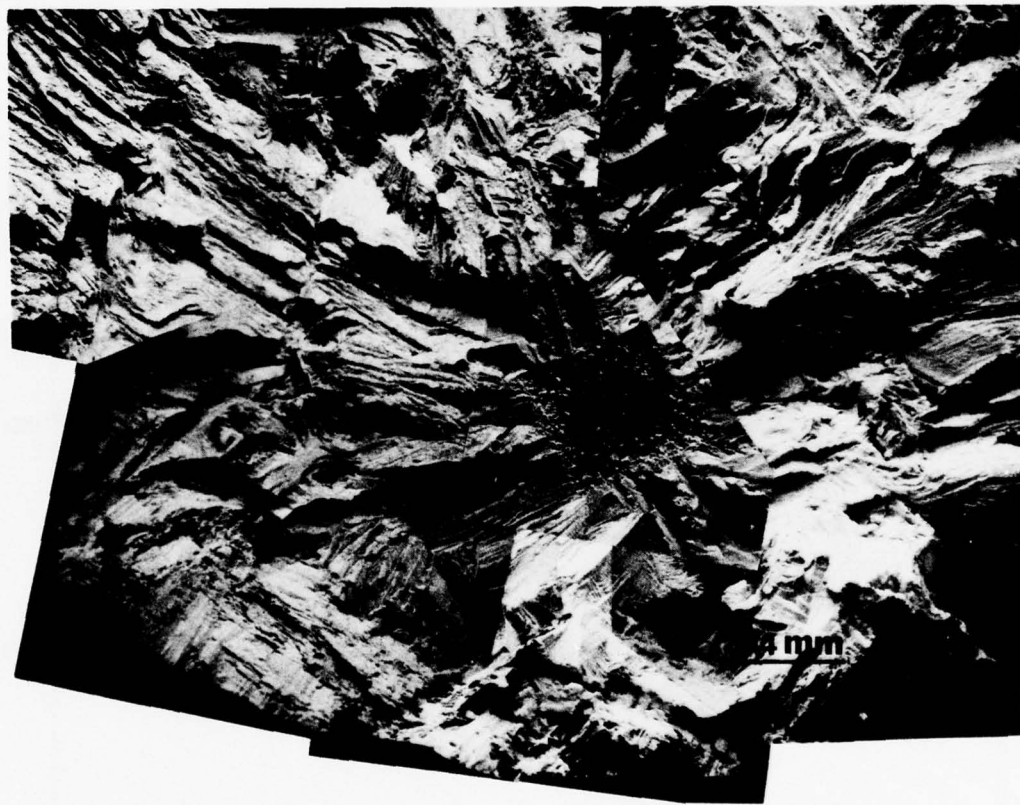


Figure 42 Fracture Appearance of the High Frequency-Tested (12 cpm) Specimen (No. 39) Which Contained a Nitride-Seeded Pore

An interesting effect of microstructures on the dwell debit on the TiN-seeded pore is obvious from Tables 12 and 13. The colony microstructure resulted in a dwell debit of two orders of magnitude. The mixed microstructure resulted in a dwell debit of one order of magnitude. The fatigue lives of the seeded specimens relative to those of the defect-free and rosette-containing specimens are illustrated in Figure 43 for sets 2 and 3. The data points from specimens seeded with hydride and nitride are indicated by the letters H and N respectively. As can be seen from this Figure, the TiN-seeded defect in the colony microstructure reproduces the rosette fatigue debit reasonably close since dwell and nondwell lives comparable to those of the IMI 685 forging are exhibited. Data points from the colony-Widmanstatten microstructure lie between the rosette and the high frequency data band, therefore the rosette debit was not duplicated in this case.

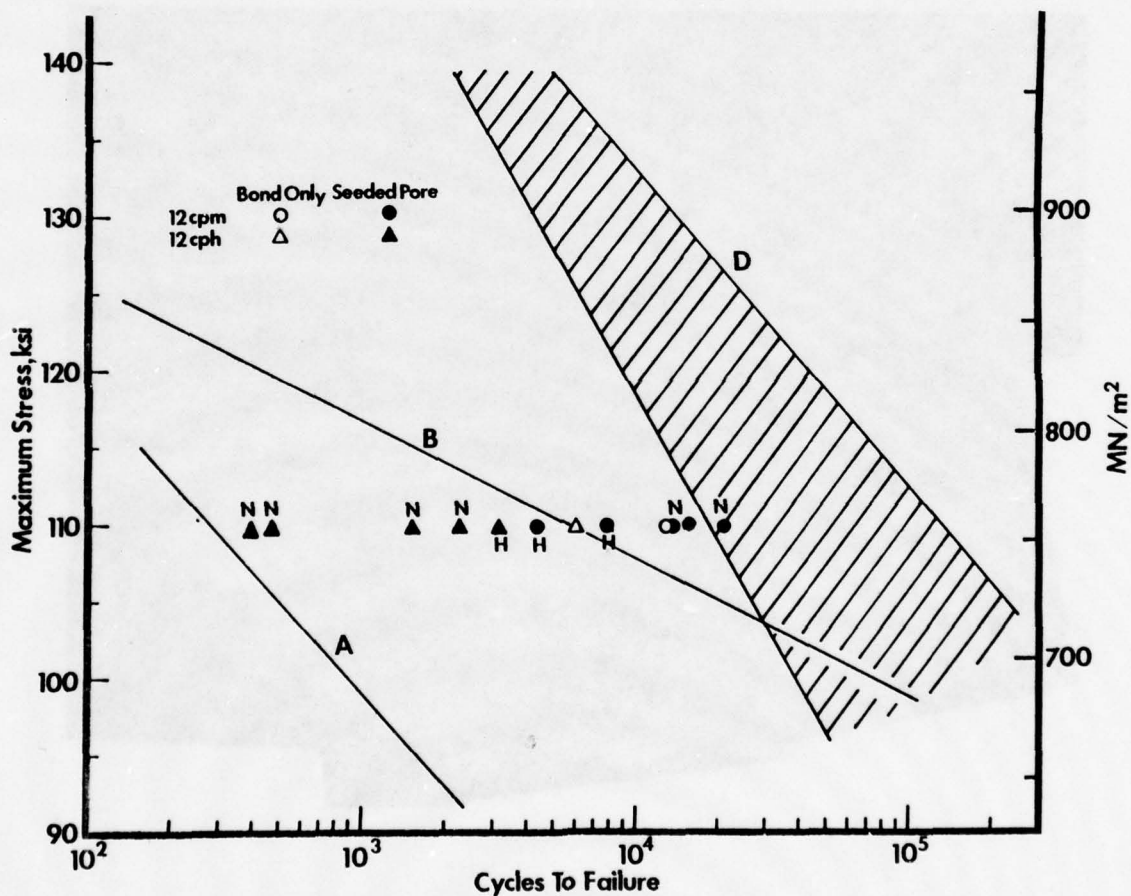


Figure 43 The LCF Lives of Seeded IMI 685 Specimens Relative to those of the Dwell-Tested (12 cph) Specimens Containing Rosette Defects (Curve A) and Defect-Free Specimens (Curve B); Those of the Defect-Free or Rosette-Containing Specimens test at 12 cpm are Given by the Scatterband D. The data points from specimens seeded with hydride are indicated by H and those from specimens seeded with nitride by N.

### (3) A Defect-Containing Specimen Machined From a Forging

In an attempt to reproduce rosette-type of failure observed previously by P&WA in a flat disk manufactured from Ti-6Al-2Sn-4Zr-2Mo alloy (See Section II.1) a disk section was inspected by ultrasonic C-scan technique to locate defective regions. A fatigue specimen was then fabricated containing one such region in the gage section, the shape and orientation of this specimen is shown in Figure 44. The microstructure of this material is shown in Figure 45 and is typical of an alpha:beta forged and heat treated component. The specimen was tested at a cyclic stress level of 10-110 ksi with a dwell of 1.5 minutes at maximum load. Fracture of the specimen occurred after  $1.2 \times 10^4$  cycles. The fracture surface around the nucleation site is shown in Figure 46, and the nucleation site is shown at higher magnification in Figure 47a. The fatigue origin consisted of a row of interconnected pores extending to the surface of the disk. This row of pores is inclined at about  $45^\circ$  to the plane of the disk and has dimensions of  $0.001'' \times 0.00013''$ . The fracture origin bears some similarity to cleavage rosette-type of failure in that it consists of small holes surrounded by a cleavage facet on which no fatigue striations were observed. Figures 47b and c illustrate the fracture appearance at positions removed from the fracture origin in which striations can be observed.

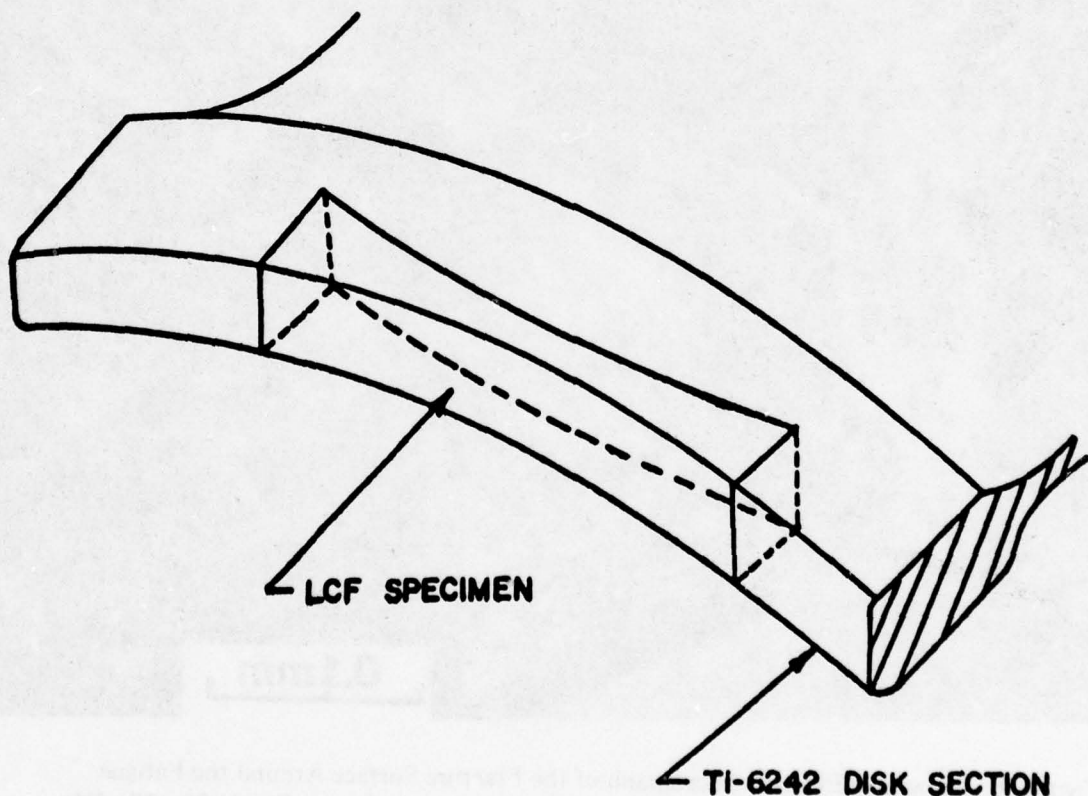


Figure 44 The Shape and Relative Orientation of the Fatigue Specimen Machined from the Ti-6Al-2Sn-4Zr-2Mo Flat Disk. A defect had been located at the gage section of the specimen by the ultrasonic C-scan technique.

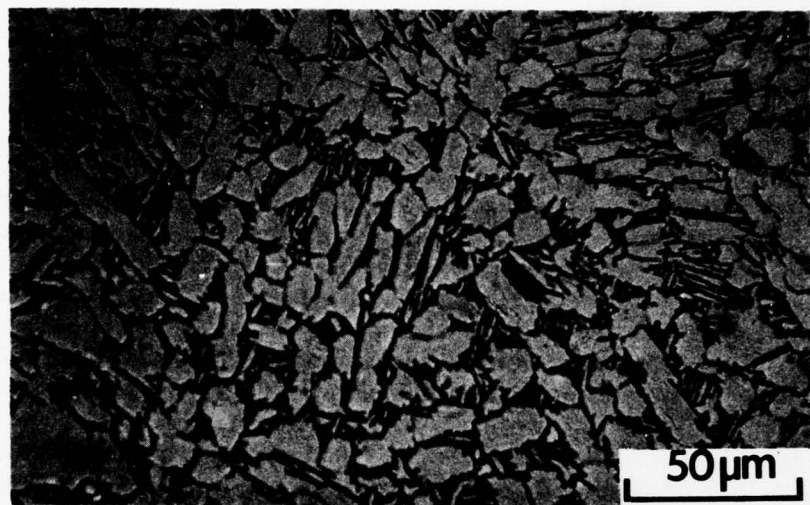


Figure 45 Microstructure of the Ti-6Al-2Sn-4Sn-2Mo Disk

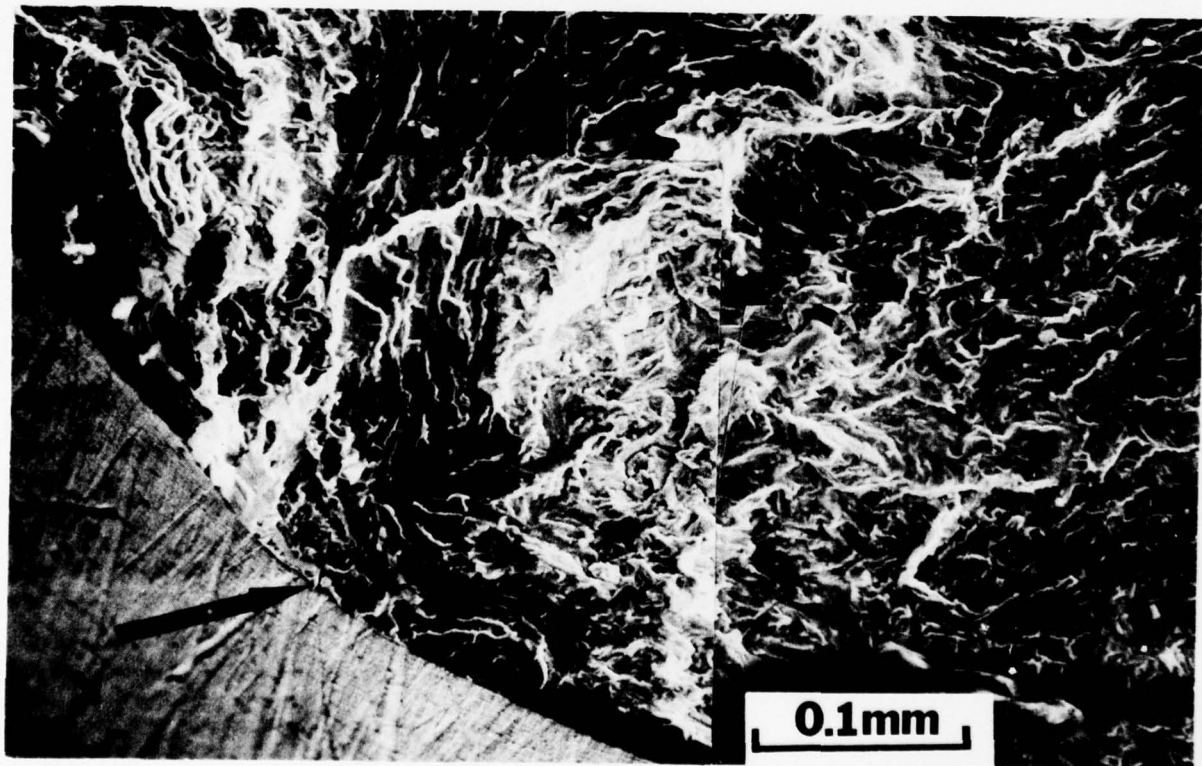


Figure 46 Scanning Electron Micrograph of the Fracture Surface Around the Fatigue Crack Origin in the Specimen Machined from a Defective Ti-6Al-2Sn-4Zr-2Mo Flat Disk (see Figure 44). The nucleation site which is shown in greater detail in Figure 47(a) is indicated by an arrow.

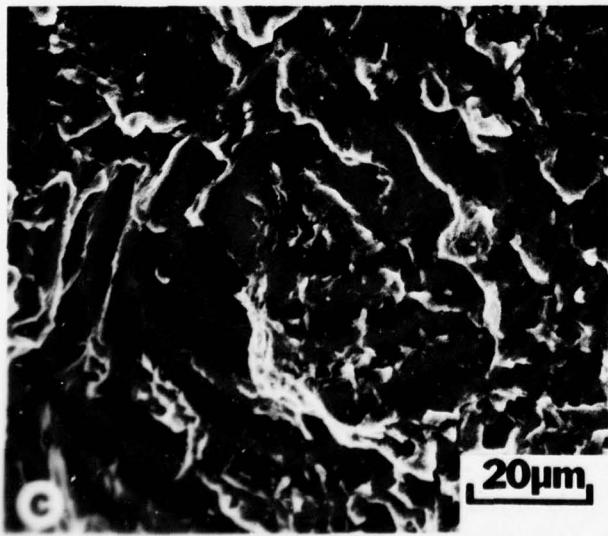
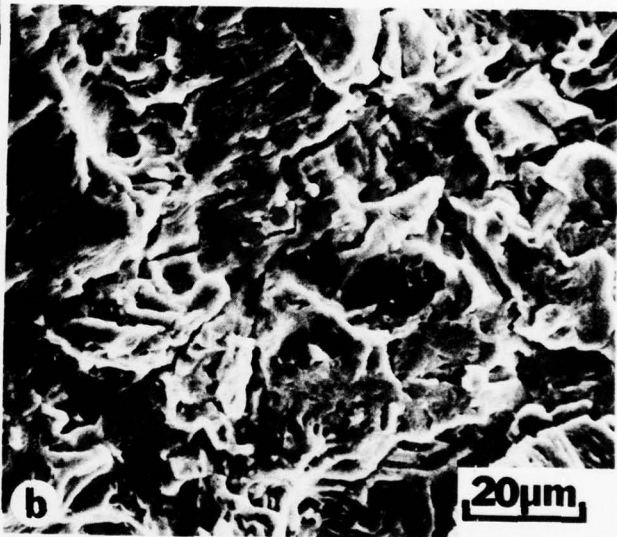
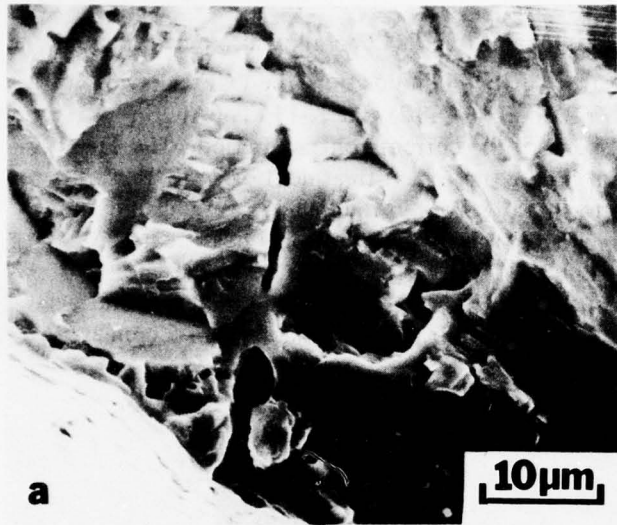


Figure 47 (a) Details of the Crack Nucleation Site Shown in Figure 46. Typical appearance of fatigue striations on fracture surfaces are shown in (b) and (c).

#### (4) Dwell Debts in Other Alpha:Beta Titanium Alloys

To determine whether the dwell debits observed in defect-free IMI 685 alloy also occur in other titanium alloys which have similar microstructure and composition, the LCF behavior of the alpha:beta titanium alloys Ti-6Al-2Sn-4Zr-2Mo (Ti-6-2-4-2) and Ti-11 (Ti-6Al-2Sn-1.5Zr-1Mo-0.35Bi-0.1Si) was examined near the end of the current contract period. The Ti-6-2-4-2 was isothermally beta forged and given a grain growth heat treatment of 2150°F for 2 hours to produce a beta grain size similar to that observed in the IMI 685 forging and illustrated in Figure 48. The sections were subsequently given a conventional heat treatment consisting of 1800°F for 1 hour, air cool and 1100°F for 8 hours, air cool. Fatigue specimens of the type shown in Figure 1 were machined from the heat treated materials and tested at maximum stresses of 110 ksi and 130 ksi using cyclic frequencies of either 5 cpm or 12 cph. All tests were performed at room temperature.

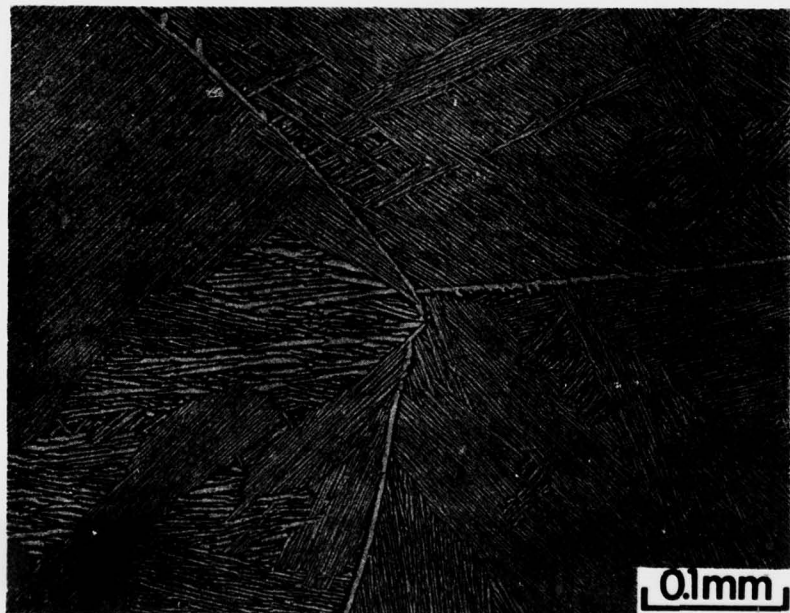


Figure 48 Microstructure of the Beta-Heat Treated Ti-6Al-2Sn-4Zr-2Mo.

Fatigue results are given in Table 14. Although none of the specimens were tested to failure under dwell conditions, it is evident from Table 14 that the dwell debits in Ti-6-2-4-2, if any, is less than one order of magnitude at 130 ksi and probably smaller at 110 ksi. Similar observations have also been made in alpha:beta heat treated Ti-6-2-4-2.<sup>(10)</sup>

The Ti-11 alloy was beta forged and had a heat treatment consisting of 1600°F/24 hr./AC + 1300°F/2 hr./AC + 1100°F/8 hr./AC. This heat treatment resulted in some spheroidization of the beta phase as shown in Figure 49. Two specimens were LCF dwell-tested under a stress range of 36-120 ksi at room temperature. Failure had not occurred after 6200 cycles. The corresponding fracture life of this material at 10 cpm is ~ 20,000 cycles. Therefore the fatigue debit in Ti-11, if present, is again smaller than for IMI 685.

TABLE 14  
LCF TESTS OF BETA HEAT TREATED  
Ti-6Al-2Ns-4Zr-2Mo

Specimen No.	Stress Range (Ksi)	Cycles to Crack Indication	Crack Size (in.)	Propagation Life	Fracture Life
12 cph					
4	33-110	16,380 +	0.000	—	—
9	39-130	14,270 +	0.010	—	—
11	39-130	12,500 +	0.000	—	—
12 cpm					
6	11-110	—	—	—	24,750
10	39-130	9,000	0.010	17,777	26,777
13	39-130	31,850	0.016	11,088	42,938

+ Test discontinued

— No data

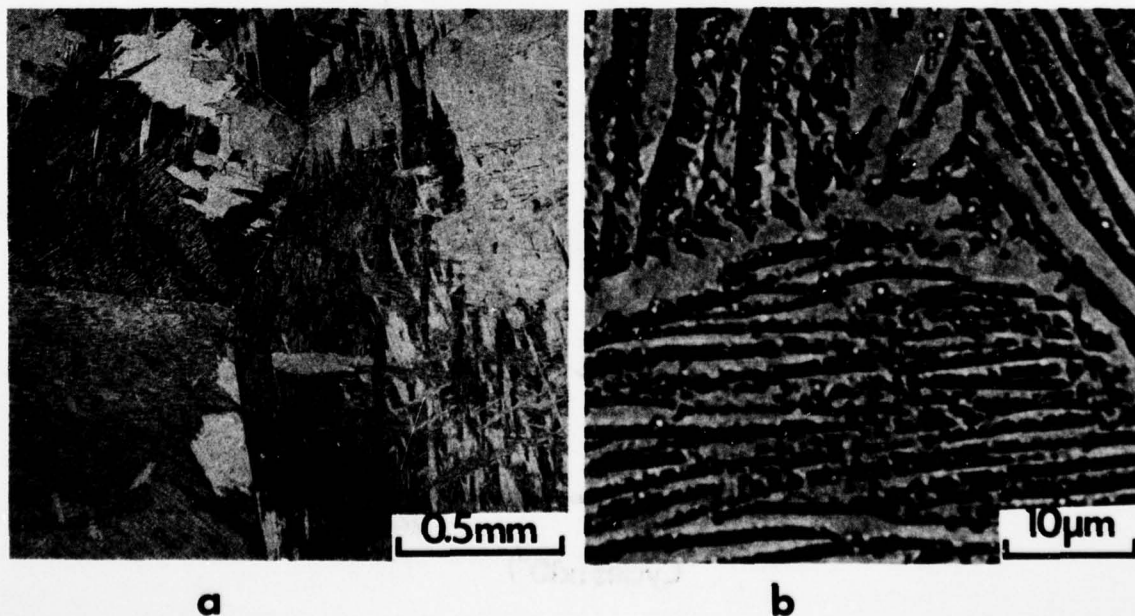


Figure 49 Microstructure of Ti-11 (a) shows the Large Prior Beta Grains and (b) Shows the Spheroidized Beta Phase

##### (5) Crack Growth Measurements in Other Alpha:Beta Titanium Alloys

As we shall examine in more detail in Section II.3, one of the anomalous features observed in IMI 685 is the lack of correlation between crack growth rates determined in precracked fracture mechanics specimens and the growth rates measured in the LCF specimens used in the current study. (This can be seen by comparing curves A and D in Figure 35). In order to identify the sources, such as difference in specimen geometry, microstructure and alloy composition, etc., for the observed discrepancy, the progression of surface-nucleated cracks in LCF specimens have been measured in beta-heat treated Ti-6-2-4-2 and an alpha:beta heat treated Ti-6Al-4V. The experimental techniques used and the treatment of data were the same as those used on IMI 685 specimens described earlier. The microstructure of the beta heat treated Ti-6-2-4-2 were given in the preceding section. The propagation data for a surface crack in Ti-6-2-4-2 (Specimen #10) is given in Figure 50. Comparisons between the crack propagation data derived from the surface crack measurements in LCF specimens and those from fracture mechanics specimens (solid lines) are illustrated in Figure 51 and it can be seen that the agreement between those two sets of data is reasonably good in both alloys.

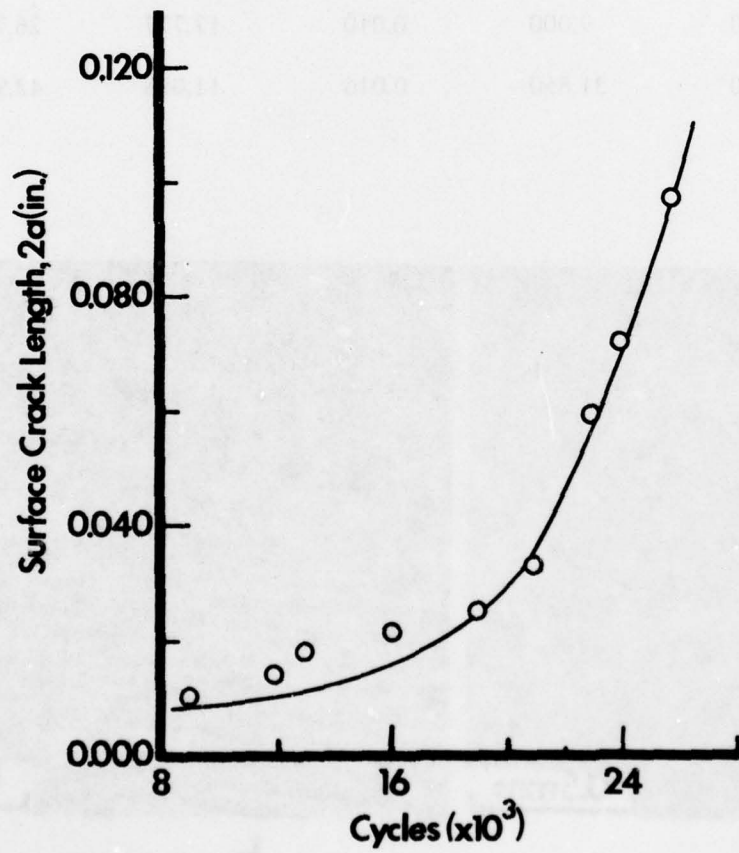


Figure 50 Surface Crack Length,  $2a$  Versus Number of Cycles for Ti-6Al-2Sn-4Zr-2Mo Specimen No. 10

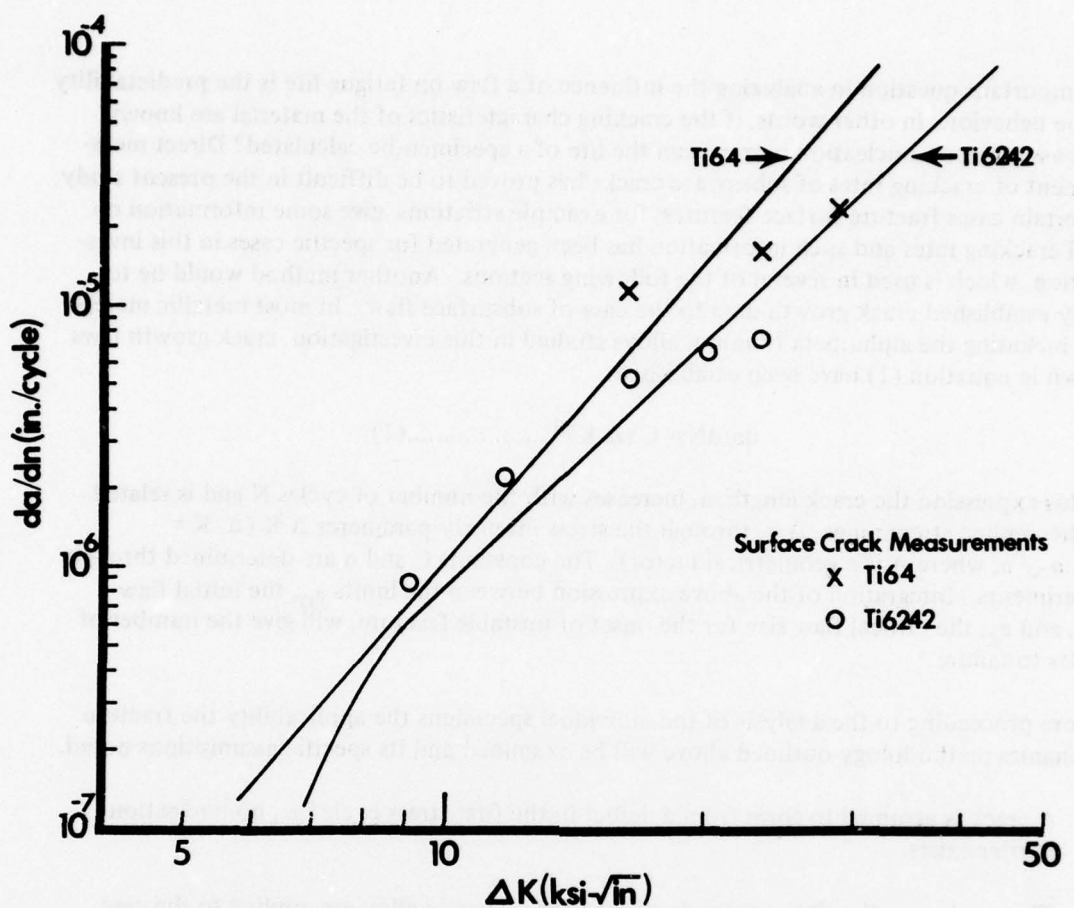


Figure 51 Results of Surface Crack Measurements on Beta-Heat Treated Ti-6Al-2Sn-4Zr-2Mo and STA Treated Ti-6Al-4V LCF Test Specimens Plotted in Terms of  $da/dN$  versus  $\Delta K$ . The fatigue crack propagation rates determined from fracture mechanics specimens are indicated by solid lines.

### 3 DISCUSSION

The major aim of this part of the investigation was to study and explain the influence of relatively small defects on the fatigue behavior of alpha:beta titanium alloys. Emphasis was placed on the modification of fatigue capability of material which contains these flaws-interest in subsurface fatigue origins having been triggered by the experience with IMI 686 noted in the introduction. As the evidence for major contamination at the fatigue origins in the IMI 685 was slight, in most of the experiments in which artificial defects were introduced, the concentration of the contaminant was relatively low. As illustrated in Figure 40 little or no indication of microstructural modification by the presence of the contaminant could be observed on longitudinal section through such flaws. (Obviously from several examples cited e.g., Figure 7 the presence of contamination within a flaw on the fracture surface could be readily detected). It should be clear therefore that the experiments did not attempt to simulate defects such as hard oxygen or nitrogen stabilized regions in which microstructural modification is readily observed.

An important question in analyzing the influence of a flaw on fatigue life is the predictability of the behavior. In other words, if the cracking characteristics of the material are known (and assuming no nucleation barrier) can the life of a specimen be calculated? Direct measurement of cracking rates of subsurface cracks has proved to be difficult in the present study. In certain cases fracture surface features, for example striations, give some information on local cracking rates and such information has been generated for specific cases in this investigation, which is used in several of the following sections. Another method would be to apply established crack growth data to the case of subsurface flaw. In most metallic materials, including the alpha:beta titanium alloys studied in this investigation, crack growth laws shown in equation (1) have been established.

In this expression the crack length,  $a$ , increases with the number of cycles  $N$  and is related to the applied stress range,  $\Delta \sigma$ , through the stress intensity parameter  $\Delta K$  ( $\Delta K = A \Delta \sigma \sqrt{a}$ , where  $A$  is a geometrical factor). The constants  $C$  and  $n$  are determined through experiments. Integration of the above expression between the limits  $a_0$ , the initial flaw size, and  $a_c$ , the critical flaw size for the onset of unstable fracture, will give the number of cycles to failure.

Before proceeding to the analysis of the individual specimens the applicability the fracture mechanics methodology outlined above will be examined and its specific assumptions noted.

- 1) A crack is assumed to form from a defect in the first stress cycle i.e., no nucleation barrier exists.
  - 2) The crack growth relationships developed for a specific alloy are applied to the case of a contained subsurface flaw. Factors such as environment, which are known to influence crack growth in alpha:beta titanium alloys, are therefore not the same. A more important consideration is the difference in conditions between conventional tests to generate  $da/dN$  information and those used for the specimens in the present study.

Typically in fracture mechanics testing, precracked specimens are used which have relatively long cracks thus low stresses can be used. Such conditions serve to minimize plasticity effects and apply to situations where fracture mechanics methodology is known to be applicable. In the type of tests used in the present study crack lengths are relatively short and the applied stresses are high. It is for this reason that the crack growth relationships were determined on the specimens used in the present study in order to provide a direct comparison with more conventional  $da/dN$  data.

- 3) The critical crack length,  $a_c$ , which defines the upper integration limit in the analysis, is not equivalent to the value observed in a valid  $K_{IC}$  test. If the measured crack sizes are used to compute stress intensities at instability,  $K_Q$  values in the range 40-50 ksi/in are obtained.
  - 4) Stress intensity solutions are functions of specimen geometry and crack shape. In the analysis used in the present study surface cracks are approximated by a semi-circular crack solution<sup>(11)</sup> and the penny shape crack solution of Erdogan and Sih<sup>(9)</sup> for sub-surface cracks.

In the following paragraphs several groups of experimental results are discussed with emphasis on the fatigue capability, fractographic features and calculated fatigue lives. Where possible, results from the various sections of the present work will be combined to give a more complete summary of a specific topic.

#### Seeded Flaw Experiments on Ti-6Al-4V and Ti-6Al-2Sn-4Zr-2Mo

The initial part of this investigation concentrated on the alloy Ti-6Al-4V in two microstructural conditions. Flaws in the form of hardness impressions into which selected contaminants were introduced were used to assess the influence of defects on fatigue capability. In the case of the equiaxed alpha:beta microstructure the relatively low life of all specimens (Table 1) can be attributed in part to the non-standard heat treatment that produces rather low strength. In the case of the small indentation size (0.01") little or no modification in fatigue life was observed. By increasing the size to 0.03" the effect of various contaminants became obvious. These results may be divided into several groups depending on both life and the observed fractographic features. The lowest life specimens which are those seeded with MgC<sub>1</sub> and hydride, showed fractographic features more typical of general embrittlement and no clear-cut evidence of a typical fatigue crack progression could be observed. In the other specimens containing seeded impressions subsurface fatigue crack growth from the seeded flaws had occurred. One feature of the subsurface fracture subsurfaces, which appears relatively general in all the experiments performed in this study, was the cleavage-like appearance and thus absence of striations on the facets. It has been shown by Yuen et. al.<sup>(6)</sup> that for cracks propagating in an air environment, striations are observed if the applied cyclic stress intensity is  $> 14 \text{ ksi}\sqrt{\text{in}}$ . In the present study of subsurface cracks no striations are observed at stress intensity levels as high as  $45 \text{ ksi}\sqrt{\text{in}}$ . Evidence suggests that this is an environmental effect for in cases where the crack forms at the specimen surface, such as the control specimens, striations are observed. One other result from Table 1 that requires comment is the observation that the specimen with the larger impression (#10) had a longer life than either the baseline or the specimen containing the smaller clean impression (#1). This could be attributed to the observed multiple crack initiation in the former case that may result in smaller stress intensities at the cracks. For equiaxed microstructures the correlation between crack growth observed in the specimens used in this study and da/dN type data is shown in Figure 51. It can be seen that both types of data are in reasonable agreement. Life calculations using an assumed 0.03" flaw diameter yields an expected life of 2000 cycles which is of the correct magnitude to account for most of these data.

The third set of specimens were processed to give an acicular beta microstructure. In this test series quite marked effects on fatigue life were observed as may be seen from Table 2. Fractographic examination showed the same trends as those observed in equiaxed microstructures; for subsurface crack growth the overall cleavage-like appearance prevailed. Closer examination of the individual facets formed by subsurface crack growth showed ill-defined surface features, however, as soon as a crack broke through the specimen surface, well-defined striations could be observed. These effects are illustrated in Figure 6. The fatigue results may be divided into two groups, a group with a cyclic life of  $\sim 6000$  cycles which includes the hydride, aluminum and uncontaminated flaws and the second group

showing a life of ~ 2500 cycles for the nitride or chloride additions. Again using a 0.03" diameter flaw the calculated life (using the crack growth data of Yoder<sup>(12)</sup>) is ~ 5000 cycles. This can be considered a reasonable agreement with the first group of results. In the case of the chloride-containing specimens in the second group a reaction layer was detected around the hardness impression (Figure 7) which could increase the effective size of the flaw. The measured increase in size does not correlate exactly with the observed decrease in life however. Nitride additions did not produce any observable increase in the flaw size and nitrogen appears to have a similar effect on Ti-6Al-4V as in IMI 685 which will be discussed below.

The attempts to seed argon into impressions in Ti-6Al-2Sn-4Zr-2Mo were not successful and this can be seen from data presented in (Table 3). Even in the best specimens quite large regions of unbonded area were still present. Thus these experiments only reinforce previous work on fabrication and joining of titanium alloys in that once argon is introduced it is difficult to remove and results in very poor adhesion between surfaces. In the case of the IMI 685 forging no evidence of similar poorly bonded regions was obtained. Therefore further attempts to produce argon contamination were not made.

#### The Fatigue Behavior of IMI 685

At the outset of this discussion, it should be emphasized that the rather large forgings that were studied in this and other investigations represent an unusual product form. The regions of the forging which exhibited the very low fatigue capability had received a low degree of mechanical work and exhibited a very large beta grain size. Further, the tendency to form rosette defects appears to be confined to forgings produced from the upper section of the ingot - which may be construed as indicating that solidification defect structure has contributed to the rosette phenomenon.

The overall fatigue capability of the forging studied in this investigation is rather complex. However, if the results are combined with those of other evaluations, as has been done in Tables 5, 6 and Figure 18, a consistent behavior pattern emerges. We shall discuss the overall phenomenology of the fatigue characteristics of the forging before examining the mechanisms that may cause the behavior. The cyclic life under dwell test conditions can be divided into two groups - the "rosette debit" which seems to be related to some type of pre-existing defect and the dwell debit which appears to be a general or bulk effect. In both cases the specifics of crack nucleation and subsequent growth can be inferred to be very rapid compared to high frequency testing and we shall examine the state of knowledge for both cases below. However before proceeding to these specific areas, the basic problem with the rosette-type failures can be appreciated by examining Table 15. If the lives of specimens are computed assuming the presence of flaws and using the known crack growth data for IMI 685 (Curves B and C shown in Figure 35b) lives of  $> 10^5$  cycles would be anticipated whereas fracture lives of  $< 10^3$  have been found. We shall return to the other calculations presented in this Table in the discussion of the growth characteristics of cracks under dwell conditions.

TABLE 15  
CALCULATED FRACTURE LIVES OF IMI 685 USING  
VARIOUS CRACK PROPAGATION LAWS  
30-100 ksi, 0.03" DIAMETER PENNY-SHAPED CRACK

Crack Propagation Law	Curve B*	Curve C*	Model B°
Calculated Life (cycle)	$1.75 \times 10^5$	$7.62 \times 10^4$	$3.86 \times 10^3$

\*Figure 35b

°Figure 52b

In discussing the nucleation event of a rosette failure, a complicating factor is the pre-exposure of the forging before analysis was initiated. As noted in the results, section inspection of the disk revealed several indications which were preferentially selected for the specimen evaluation. In one case, in which an indication was sectioned, cracks were detected, which indicates that at least in some cases the indications can be interpreted as cracks. The cracking rates that can be inferred from the lengths of these cracks, assuming that growth occurred during the 60 cycles of exposure, are  $\sim 5 \times 10^{-4}$  inch/cycle. These cracking rates are considerably more rapid than those measured with fracture mechanics specimens. The test performed on the specimen (#2) cut in the radial direction may provide some additional information on initial cracking rates. Although this specimen showed a very low life typical of rosette behavior only some of the more classic rosette fractographic features were observed compared with specimens in the circumferential direction. In one facet near the fatigue origin in Specimen #2 markings could be observed which are illustrated in Figure 17. If each of these markings represents the crack position after each cycle, the spacing correspond to a cracking rate of  $3 \times 10^{-3}$  inch/cycle in the first facet and  $9 \times 10^{-4}$  inch/cycle in the second. In other words, the crack propagated at a slower rate in the second facet. It can be noted that these rates are in reasonable agreement with the rates deduced above.

However, it should be noted that the markings observed in Specimen #2 appear to be unique, as no similar features have been observed in circumferentially oriented specimens.

As cracks extend from the origins the general mode of separation retains a cleavage-like appearance. However, as noted in the results section, sporadic patches of striations are observed. It can be assumed that the regions of striation represent growth in grain or colonies not oriented correctly for the cleavage mode of cracking. A more important question is, can striation spacings be used to assess the average growth rates for the crack extension during the rosette formation? There is no absolute answer to the question but the fact that the spacing increases in a systematic way with distance from the crack nucleus indicates that the crack grows relatively uniformly. If this was not the case, in that the cleavage area formed much more rapidly than the striated area, then we would anticipate large increases in spacing within facets and a much less regular progression. The striation data has been collected in Figure 35b in which the distance from the crack origin has been used to compute a local  $\Delta K$  value. If these two pieces of information on crack nucleation and growth are combined Figure 52(a) can be constructed for Specimen #2 and inferred from striation measurements for Specimen #4. We can generalize the behavior pattern, as done in Figure 52(b). Curve A represents a constant rate of crack progression until a more rapid crack mode becomes available. Such a "model" is a reasonable representation of Rolls Royce thinking<sup>(8)</sup>. Curve B represents an average of the behavior depicted in Figure 52(a).

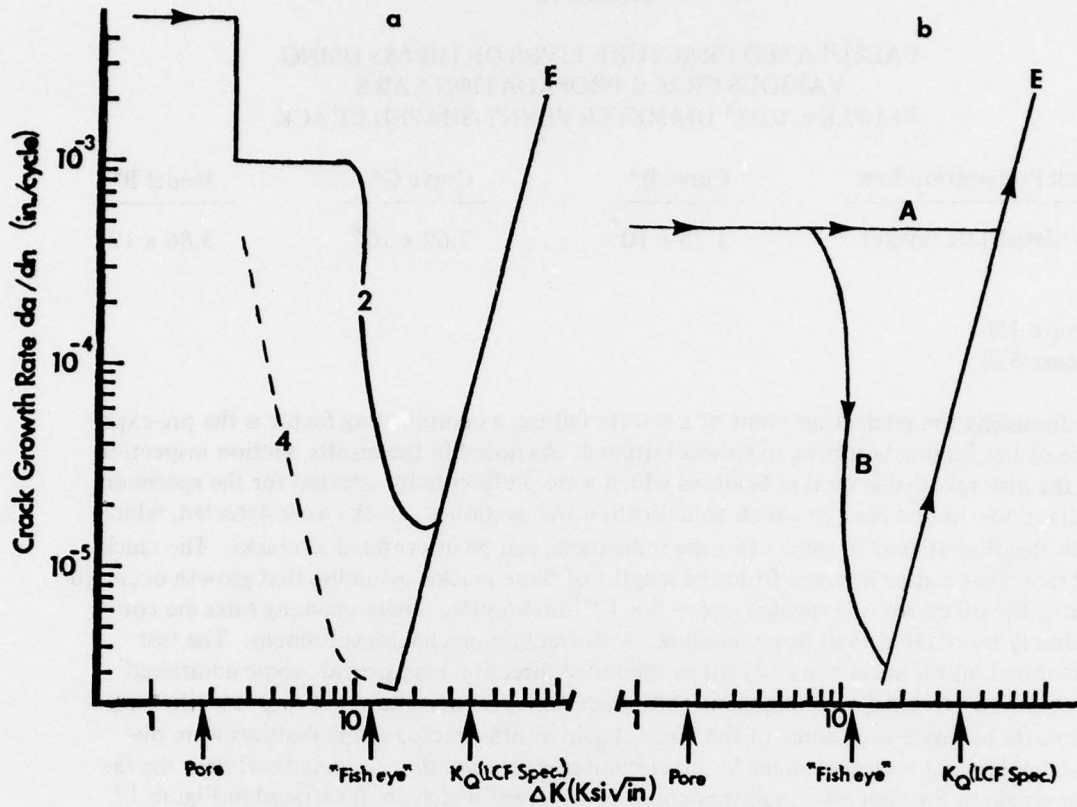


Figure 52 (a) Crack Growth Behavior Inferred From Striation Observation on IMI 685 Specimen No. 2 (Curve 2E) and Specimen No. 4 (Curve 4E)  
 (b) Idealized Representations of Results Shown in (a). Curve AE represents an initially constant rate of crack propagation until a more rapid crack mode (Curve E) becomes available. Curve B represents an average of Curves 2E and 4E in (a).

If these two models are used to calculate lives of LCF specimens the Curves A and B shown in Figure 53 are obtained, which bound the rosette results and also include some of the dwell results discussed in more detail below. The specific values that result from Model B for a stress level of 30-100 ksi are included in Table 15 assuming that a crack of length 0.03" forms very rapidly. Although curves A and B bound the data points, both curves have a slope much higher than that observed, at least for the circumferentially oriented specimens. A simplistic method of producing Curve C is to postulate that at high stresses Curve A is followed while at lower stresses cracking occurs of the type shown in Curve B. Indirect evidence that this could be true is the lives of Specimens #2 (292 cycles) and #4 (1600 cycles) both of which were sectioned from adjacent locations in the same forging. In the case of Specimen #4 the material was stress relieved during specimen fabrication, if residual stress was present in Specimen #2 the applied stress could be amplified by the local stress field, thus leading to a more rapid cracking rate. Rolls Royce have also postulated that re-

sidual stress may have modified the cracking rates in these forgings although the major effect was considered to be on crack growth under dwell cycle conditions at high  $\Delta K$  levels (Curves A, Figure 35a). This is a controversial result<sup>(16)</sup> and further the use of the dwell data at K levels which exceed the  $K_Q$  values obtained in the specimen tests is unclear.

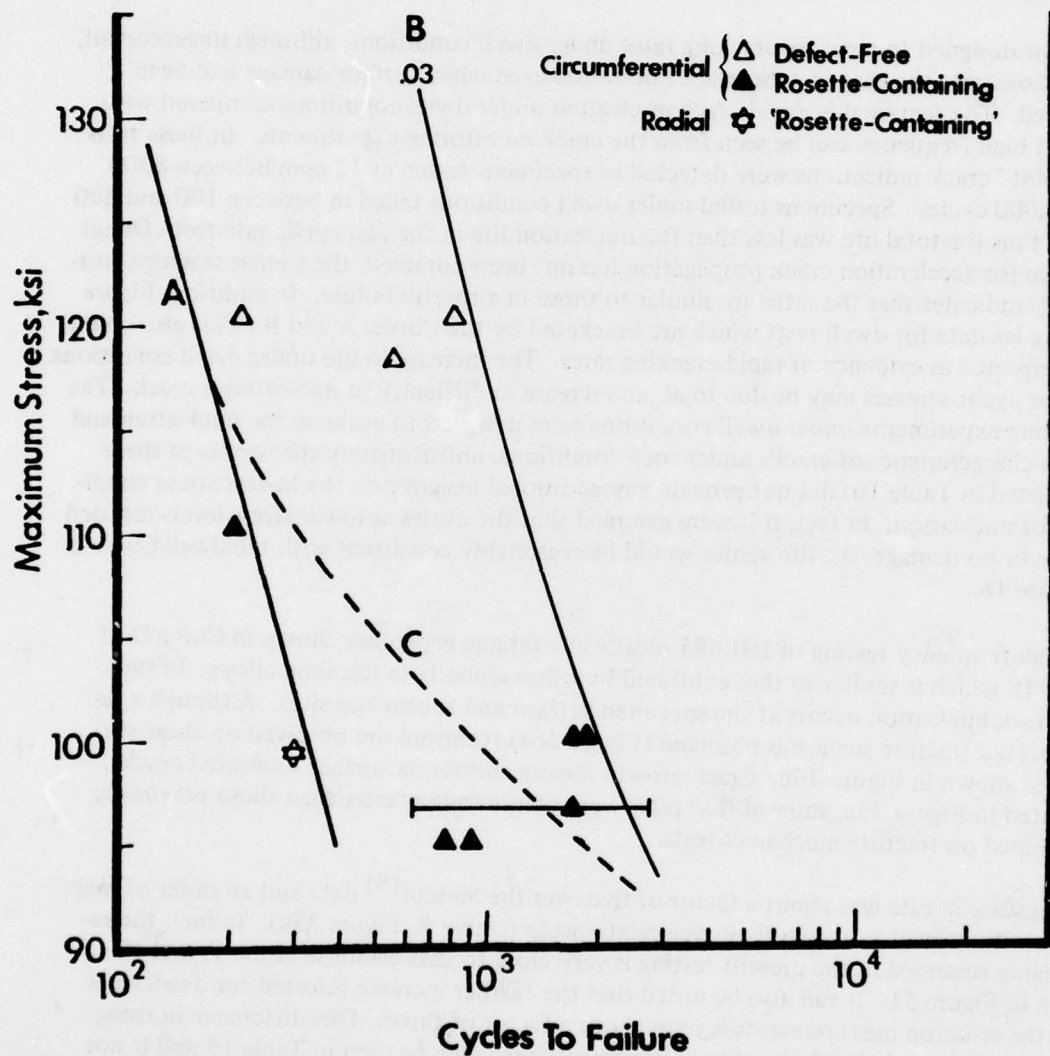


Figure 53 Calculated Fracture Lives as Function of the Maximum Stresses Assuming an Initial Penny-Shaped Flow of 0.03" Diameter. Curves A and B are obtained, respectively, from Curves AE and BE shown in Figure 52b. A combination of Curves A and B results in Curve C.

The dwell debit observed in non-defective material is defined in Figure 18. A large effect is observed at high stresses but the results merge with the high frequency data population at cyclic stresses of 0-100 ksi. The fracture morphology of dwell-tested specimens duplicate the features of a rosette failure to a marked degree the only features that are absent are the pore and a well defined "fish-eye" region. As with the rosette fracture, cracks always originate at a subsurface site.

The tests designed to measure cracking rates under dwell conditions, although unsuccessful, did demonstrate the ease of subsurface nucleation even when surface damage had been produced. The remarkably rapid crack nucleation under dwell conditions compared with those at high frequency can be seen from the crack monitoring experiments. In these tests "pinpoint" crack indications were detected in specimens tested at 12 cpm between 8000 and 24,000 cycles. Specimens tested under dwell conditions failed in between 100 and 800 cycles, thus the total life was less than the nucleation life in the fast cyclic rate test. Direct evidence for acceleration crack propagation has not been obtained, the similar fracture morphology indicates that the rates are similar to those in a rosette failure. In addition, Figure 53 includes data for dwell tests which are bracketed by the Curves A and B. This also could be interpreted as evidence of rapid cracking rates. The increase in life under dwell conditions at lower cyclic stresses may be due to as an increase in difficulty of nucleating a crack. The uploading experiments under dwell conditions were designed to evaluate the nucleation and growth characteristics of cracks under such conditions, unfortunately the results of these tests (listed in Table 10) did not provide any additional insight into the lowest stress conditions for nucleation. In fact, if it were assumed that the cycles at lower stress levels resulted in little or no damage, the life values would be reasonably consistent with the dwell Curve B in Figure 18.

The high frequency testing of IMI 685 results in a fatigue capability shown in Curve D of Figure 18 which is similar to that exhibited by other alpha:beta titanium alloys. In such tests crack nucleation occurs at the specimen surface and subsurface sites. Although a rather faceted fracture surface is observed (Figure 26a) striations are observed on these surfaces, as shown in Figure 26b. Crack growth measurements on surface nucleated cracks, presented in Figure 35a, showed that rates were considerably faster than those previously determined on fracture mechanics tests.

The increase in rate was about a factor of five over the Metcut<sup>(8)</sup> data and an order of magnitude with respect to the Rolls Royce relationship (Curve B, Figure 35a). In fact, the relationship observed in the present testing is very close to that established for Ti-6Al-4V shown in Figure 51. It can also be noted that the further increase inferred for dwell tests from the striation measurements is only about a factor of three. This difference in using the dwell curve and air relationship in life calculations may be seen in Table 15 and is not large.

The group of results obtained in the present and other investigations for specimens tested as a fast frequency but which (probably) contained pre-existing defects show somewhat variable fatigue results. One case of a rosette fracture showing a large life debit although tested under a high frequency (Specimen #25) has been found, if in this specimen the rosette was present at the start of the test, the life can be predicted readily. The measured radius of the "fish-eye" in the specimen was 0.023" using this value in conjunction with the growth laws

labeled E and D in Figures 35b the calculated lives are 490 and 1700 cycles, respectively. A life of 890 cycles was observed. This may indicate that the growth of a subsurface crack under rapid cycling is faster than a surface crack, a conclusion which is supported by the striation measurement, included in Figure 35b, which lie on Curve E.

Eylon and Hall<sup>(5)</sup> report the failure of a specimen tested at 33-110 ksi at 20 cpm (Specimen #1, Table 6) from a small surface rosette. This data is plotted in Figure 18. Assuming the rather small rosette was present at the initiation of testing the same computational method using Curves E and D gives results of  $1.3 \times 10^4$  and  $4.1 \times 10^4$  cycles which bound the actual failure life of  $2.4 \times 10^4$ . This leaves two other test results in which rosettes were detected on the fracture surface<sup>(5)</sup>. As cracks apparently did not nucleate in these areas it could be postulated that they were formed during crack propagation and therefore did not modify life.

The final group of results are for IMI 685 specimens with artificially introduced defects. Fatigue lives obtained from these specimens given in Tables 12 and 13 and plotted in Figure 43 conform reasonably well with the fatigue capability exhibited by specimens from the forging. All dwell test results lie between the rosette debit and dwell curves while the high frequency lives are greater than the dwell debit but lower or equal to the "normal" fatigue capability. Results from the first set of diffusion bonded specimens can be regarded as suspect due to inadequate diffusion bonding and the results from the second and third sets are complicated by the structural differences noted in Section II.2.c(2). Analytically, the results of the nitride-seeded flaw tested under dwell conditions with the same microstructure as that of the forging (Specimen #38) can be explained using the above "model". The results on the companion specimen containing an uncontaminated impression (Specimen #31) gave a life equivalent to a non defective dwell tested specimen. As the fatigue initiation site in this specimen was independent of the seeded impression the result is obviously consistent with the data on the forging. The high frequency test on a specimen (#39) containing a nitride seeded defect resulted in a life in excess of the anticipated value. Assuming that a crack initiated at the bonded defect in the first cycle a life  $2 \times 10^3$  cycles would have been projected when in fact a life of  $2 \times 10^4$  was observed. One possible rationalization of the result is that a finite nucleation barrier existed due to the extended elevated temperature exposure experienced by this specimen (diffusion bond cycle plus a double solution treatment and age treatment). The results on the uncontaminated impression may add some credence to this suggestion.

#### Mechanism(s)

In this section we shall attempt to combine the results of the present investigation, including the tests on artificially defect-seeded specimens with other information to account for the behavior pattern discussed above. Two theories have been advanced for the nucleation stage of a rosette type failure which are critically examined below.

Rolls Royce<sup>(1)</sup> assumed that a pore was derived from the ingot stage of production and that a rosette represented a poorly bonded area which split open very rapidly on application of load. Evidence, although limited, against this is that the debit observed in a direction normal to plane of defects is of the same magnitude. A second postulate was that a cloud of

interstitials surrounded a forging defect and this produced a volume of general embrittlement. The results of local chemical analysis of a rosette fracture origin did not show any major contamination with the exception of a higher nitrogen content. A fourfold increase in local nitrogen level, over the bulk content of 0.008<sup>(5)</sup> in the material, would seem to be insufficient to produce a region of general embrittlement. On the other hand the use of nitride as a contaminant did duplicate the rosette debit in the seeding experiments, see Figure 43. The use of a large hardness impression (0.03") in this test does not simulate exactly the sites of the crack initiation in the IMI 685 forging.

Eylon and Hall<sup>(5)</sup> consider that the presence of a pore within the material is important for the nucleation stage of the process. The hypothesis derives in part from work conducted at the Aerospace Research Laboratory by the late J. Robertson and others on coarse acicular structure in Ti-6Al-2Sn-4Zr-2Mo. The investigation showed that the motion of a dislocation, especially on the basal plane has given rise to narrow slip bands with very large displacements. These slip bands can develop into shear cracks which nucleate at alpha:beta interfaces and examples are shown in Figure 54. Activation of the other important slip vector, c + a, resulted in a far more uniform dislocation arrangement with little tendency to produce large slip offsets on a specific slip plane. Eylon and Hall<sup>(5)</sup> showed that similar processes occur in IMI 685. Further they considered that in a colony containing a pore and oriented for basal slip the stress concentration associated with the pore would further concentrate deformation leading to a situation especially favorable for the formation of a shear crack.

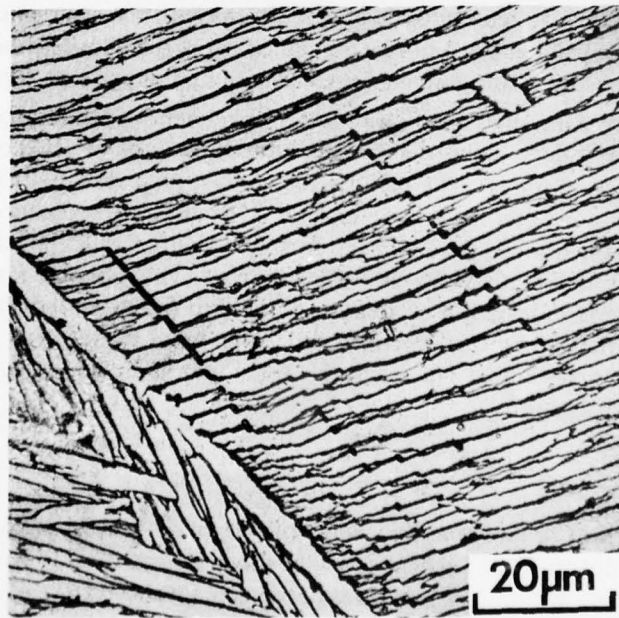


Figure 54 Formation of a Shear Crack in a Beta-Colony Structure. (Taken from the unpublished work of Roberson et al, ARL, 1972)

AD-A052 883

PRATT AND WHITNEY AIRCRAFT GROUP WEST PALM BEACH FL  
INFLUENCE OF SUBSURFACE DEFECTS ON FATIGUE PROPERTIES OF TITANIUM--ETC(U)

F33615-75-C-5138

NL

UNCLASSIFIED

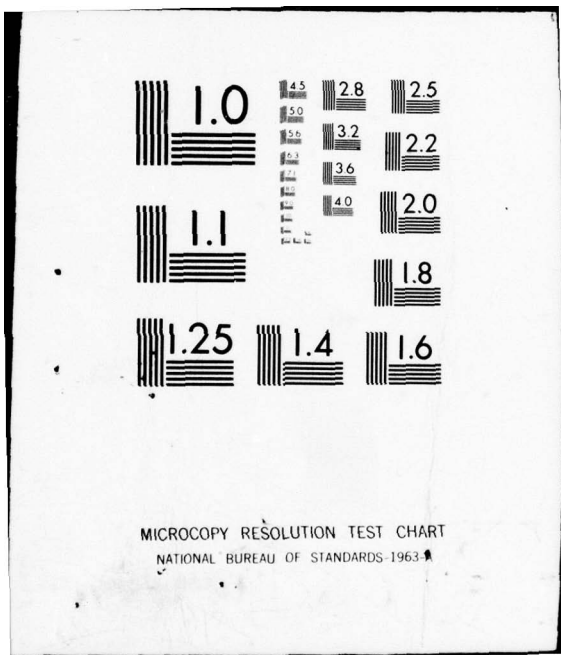
PWA-FR-8666

AFML-TR-77-112

2 OF 2  
AD  
A052 883



END  
DATE  
5-78  
FILED  
DDC



The fish-eye region would therefore be equivalent to a colony size, and Eylon and Hall produced metallographic evidence to support this premise. The results of the present investigation would also support the conclusion. Supportive kinetic evidence for Eylon and Hall's hypothesis is lacking at the present time and could prove very difficult to obtain. In the experiments conducted with an uncontaminated hardness impressions the life of one specimen (#31, Table 12) was consistent with the dwell rather than the rosette debit. This could be taken as evidence against the hypothesis. However to simulate the proposed structural condition exactly is not a trivial problem. Not only does a defect have to be introduced into a correctly oriented grain or colony but preferential growth of the colony or grain during diffusion bonding to contain the flaw has to occur. In the case cited above the crack did not nucleate at the hardness impression which highlights the simulation problem. The above postulates refer to the crack nucleation phenomenon, the second part of the process is the growth of cracks from such nuclei. If a shear crack forms in a preferentially oriented grain or colony then extension into surrounding grains should become more difficult as these will have different (random) orientations. This problem may be circumvented if the material is textured. However, as shown in Figure 12, no pronounced texture was detected in the forging studied in this investigation. The crack rate would then be anticipated to fall and as noted in the previous section this appears to occur. However the crack still propagates more rapidly than would be predicted from previously established  $da/dN$ :  $\Delta K$  relationships, an observation that applies to both a surface or subsurface crack. Typically crack growth data is obtained here from precracked specimens with relatively large notches and starting crack lengths. Thus the applied stress is usually relatively low in order to comply with fracture mechanics criteria for a valid test. On the other hand an LCF specimen is usually tested under high stresses in order to produce failures in a finite number of cycles, in this situation the crack lengths are usually short. In most cases, this difference in test conditions does not lead to vastly different growth rates when compared on the basis of applied  $\Delta K$  as shown in Figure 51. Why then is IMI 685 different? The  $da/dN$  versus  $\Delta K$  growth rates established for IMI 685 indicate considerably slower growth rates than most titanium alloys. (Compare curves B & C in Figure 35a with results for Ti-6Al-4V and Ti-6Al-2Sn-4Zr-2Mo, Figure 51). The reasons usually advanced for slower rates are the large beta grain and colony size which leads to profuse crack branching and discontinuities in cracking.<sup>(5)</sup> It is clear from the analysis of the many cracks examined in this study, formed under high stress, that the number of secondary cracks is much reduced - for example Figure 22 shows no evidence of multiple cracks. A contributing reason could be the nature and size of the plastic zone size. At low  $\Delta K$  levels the calculated plastic zone size is small compared with the microstructural size of IMI 685. The exact nature of plasticity at the tip of a crack in this material has not been studied but could differ from other alloys in that slip can propagate for large distances, and relax the intensity of stresses and strains near the crack tip. In the LCF specimen case, where stresses are close to the yield strength, this conceivably may not be true and cracking rate more typical of a normal titanium alloy with finer microstructure could be observed. Such a premise may be supported by the observation that the crack growth rate in IMI 685 LCF specimens is almost exactly equal to that observed in Ti-6Al-4V ( $da/dN$  and LCF specimens). For subsurface cracks evidence of yet faster cracking has been presented and we shall examine below some processes that could contribute to this phenomenon.

In this discussion, the distinction between crack nucleation and growth processes becomes more blurred and in practice the distinction is not clear cut. If the dwell and rosette debits are considered manifestation of the same process, the only difference being in the stress dependence of the crack nucleation event the same critical questions can be asked. These are, why the crack is always formed in a subsurface location and why is the process frequency dependant? The subsurface nature of cracking suggests either constrained plastic flow and/or a vacuum environment are important. Hold time dependence is indicative of a diffusion controlled process. The minimum hold time required appears to be  $\sim$  2 minutes depending on the stress conditions as may be seen from Figure 18. Rolls Royce has reported that no difference in behavior is noted with a five minute or a thirty minute hold time which indicates that the process is not a simple function of time but saturates at a hold time of  $\sim$  5 minutes. At least two processes can be suggested that are perhaps consistent with this type of behavior, a creep type process and a hydrogen embrittlement sequence. There are problems with either of these suggested mechanisms. Creep-type process are known to occur in alpha:beta type alloys at ambient temperatures<sup>(13)</sup>. It has recently been shown that strain is accumulated more rapidly in the acicular beta microstructure than in the equiaxed microstructure in Ti-6Al-4V<sup>(14)</sup> during cyclic testing under complex stress conditions suggesting a structural dependence in the correct direction. Further it has been suggested that a creep-type crack extension under static loading can occur in alpha:beta type alloys especially under constrained conditions<sup>(15)</sup>. However, as in these tests cracking was shown to be independent of the external environment it is therefore unclear why accelerated growth in da/dN dwell testing of IMI 685 specimens is not observed if this mechanism applies. Hydrogen embrittlement of titanium alloys is also a well known phenomenon which can take many forms. Again many superficially attractive similarities can be enumerated between the various forms of hydrogen embrittlement as the dwell and rosette phenomenon in IMI 685. Examples include the general fracture topography<sup>(16)</sup>, frequency dependence<sup>(17)</sup>, high susceptibility of the beta processed structure<sup>(18)</sup> etc. for embrittlement in hydrogen gas. These examples were deliberately cited for the case of testing in a hydrogen gas environment as it would explain the subsurface cracking observation. Diffusion of the hydrogen to a crack tip and embrittlement in that location should occur as readily for an external as an internal crack. Hammond<sup>(19)</sup>, however, has reported that a reversible hydride formation occurs in IMI 685 foils under subjected to cyclic stress. These electron microscopy observations could lend more credence to a hydrogen theory but the exact mechanism remains unclear. The series of tests performed at 400°F were undertaken to confirm a report that the rosette debit did not occur above  $> 200^{\circ}\text{F}$ <sup>(1)</sup> an observation that would lend support to a hydrogen aided cracking process. As is clear from the results a dramatic effect was found at this temperature although it is unclear if the cracks formed from pre-existing defects or were independently nucleated. These test results therefore provide no definitive information on possible hydrogen effects.

Probably the most critical objection to both postulates is that in either case the phenomenon is general to most alpha:beta titanium alloys. As discussed below there is little evidence that the dwell debit, and by inference the rosette debit, is found in any alloy other than IMI 685.

### Comparison With Other Alloy Systems

Two other types of tests were performed in order to establish if the effect found in IMI 685 were found in other alloy systems. Those were the tests on a Ti-6Al-2Sn-4Zr-2Mo disk section containing a natural defect and the dwell testing of the same alloy and Ti-11 to establish if dwell debits occurred in these systems.

The cracking observed from the naturally occurring pore in a specimen sectioned from a Ti-6Al-2Sn-4Zr-2Mo component showed evidence of some cleavage like separation at the origin. The bulk of the fracture surface appeared typical of a normal LCF failure and including the presence of striated regions. As the crack origin was very near the surface and penetration probably occurred early in the test these observations are not unexpected. The patchy nature of the striations prevented attempts to determine, by striations counting, the number of stress cycles spent in the formation of the cleavage facet at the origin. However, using the crack propagation data for Ti-6Al-2Sn-4Zr-2Mo at room temperature and an initial surface crack size of 0.0012" measured from Figure 47a, the predicted number of cycles to failure is 27,000. The measured life is 12,000 cycles and as the component had received several thousand cycles before the test the actual number of cycles to failure is greater than this. Reasonable agreement between these values suggests that the fatigue life of the defect-containing specimen was spent primarily in crack propagation and that the premature failure can be rationalized from the presence of the embedded pores which provided easy crack nucleation sites.

Dwell tests were performed on Ti-6Al-2Sn-4Zr-2Mo and Ti-11 in order to ascertain if debits similar to those in IMI 685 occurred in these alloys. If such effects were found it could be inferred that rosette-type failures may also be possible.

Although time limitations precluded carrying these tests to completion the results cited in Section II.2.C(4) indicate that dwell debits are much smaller than in IMI 685 and may not occur at all. Once conclusion that may be drawn, is that the alloy IMI 685 is unique in exhibiting the dwell and rosette phenomena in the product form examined in this program. The difference cannot be traced simply to the large structural size as a similar microstructure was produced in Ti-6-2-4-2 for the dwell tests. The two compositional factors that distinguish IMI 685 from most other alpha:beta titanium alloys are the very low beta stabilizing element content (0.5% Mo) and the relatively high silicon content (0.25%). It can be suggested that perhaps both factors may influence the deformation characteristics sufficiently to cause easy crack formation. The specific nature of these changes are not clear as narrow slip bands, shear cracks etc., can occur in Ti-6-2-4-2, and other titanium alloys with coarse acicular structures. However, the width and perhaps strength of the beta lamella present in the colony structure are lower in IMI 685, further the high silicon content may provide dislocation pinning sites. Both factors could combine to produce narrow piled-up groups of dislocations in a manner conducive to shear crack formation. As such a process is in all probability dynamic and occurs in a subsurface location confirmation of such speculation will be difficult to obtain.

### Practical Consideration

There is evidence that rosette failures are associated with inadequate ingot processing: with an improved fabrication cycle the effect can (and has) been eliminated.

The dwell debit occurs at high stresses and it is doubtful if this phenomenon would be encountered in the smooth section of a component. Notched sections could be of more concern as local stresses could be high. The alloy IMI 685 was designed as a high temperature creep resistant alloy which is the reason for the high silicon content. Beta processing of this and other alloys of the same type is becoming more common in order to amplify the creep properties. With the advent of isothermal forging techniques such processing can be controlled to give relatively fine beta grain sizes. Thus the second feature of the forging evaluated, the very large beta grain size, is not present in current forged products, similar grain sizes however, can be encountered in large titanium castings. The implications of the low fatigue life observed at 400°F are not clear, the effect is obviously related to large beta grain size but the part played by the prior cycling at ambient temperature, which could have produced damage, cannot be assessed. If an alpha:beta titanium alloy is contemplated for use with a coarse acicular structure dwell testing in the service temperature regime could well form part of any data generation program.

#### 4. Summary and Conclusions

The most important conclusions of this part of the study are summarized below, and are divided into three general categories, Fatigue Behavior, Fracture Appearance and Analysis.

##### a. Fatigue Behavior

- (1) The introduction of large (0.03") contaminated subsurface flaws in Ti-6Al-4V reduces the fatigue life in comparison with defect-free specimens, in both alpha:beta and beta processed conditions. Smaller flaws (0.01") do not reduce fatigue capability in Ti-6Al-4V processed and heat treated to give an equiaxed alpha:beta structure. Chloride and nitride seeding produced the maximum debits in beta processed Ti-6Al-4V.
- (2) The fatigue behavior exhibited by specimens sectioned from a large forging of IMI 685 and tested at 70°F is rather complex. The forging contained several sonic indications, which may indicate defective regions and in some cases cracks formed during prior cyclic exposure. Lives of specimens can be divided into groups depending on the presence of sonic indications and test frequency as shown in Figure 18.
  - 1) Specimens tested at 12 cpm which do not contain sonic indications exhibit lives comparable with other alpha:beta titanium alloys.
  - 2) Tests of non-defective specimens under hold time conditions (12 cph) at high stresses show a reduction of life of up to two orders of magnitude. (This phenomena has been termed the dwell debit<sup>(5)</sup>). At lower stresses the dwell test lives tend to become equal to high frequency test values.
  - 3) Specimens containing a sonic indication and tested under dwell conditions exhibit very low lives at stresses as low as 97 ksi. The life reduction, designated the rosette debit, can be over three orders of magnitude with respect to lives of non-defective material tested at high frequency.

- 4) High frequency testing of specimens containing defective regions gives mixed results, varying from no reduction in life<sup>(5)</sup> to quite large fatigue debits.
  - (3) Tests at 400°F produced very low cyclic lives in material with a large beta grain size. Low lives are apparently dependent on the presence of sonic indications but independent of frequency.
  - (4) In all IMI 685 specimens tested under dwell conditions crack nucleation is subsurface. Even if small surface crack nuclei were produced by high frequency testing, subsequent low frequency cycling causes independent subsurface nucleation. High frequency testing produces either surface or subsurface nucleation.
  - (5) Specimens of IMI 685 into which (0.03") artificial flaws are introduced show fatigue capability that depends on heat treatment and frequency. Dwell testing of specimens, with the same acicular colony microstructure as the forging, show lives equivalent to the rosette debit curve with nitrogen seeding and the dwell debit curve in the case of a uncontaminated defect. Dwell tests on seeded specimens with a mixed colony and Widmanstatten structure result in lives between these extremes. High frequency testing produces results that lie between the dwell debit curve and the high frequency curve.
  - (6) Based on limited testing the dwell debit in Ti-6-2-4-2 or Ti-11 with acicular microstructures is of a lower magnitude than that observed in IMI 685 or does not occur.
- b. Fracture Appearance
- (1) In all specimens tested in which subsurface crack nucleation and growth occurred the fracture surface have a general cleavage-like appearance. The individual facets exhibit rather varied structures ranging from areas of striations to virtually featureless regions. Cracks that nucleated on the surface, or subsurface cracks that break through the surface, exhibit more "typical" fatigue surfaces in which extensive regions of striations can be observed.
  - (2) The IMI 685 fracture surfaces could be related to the fatigue life exhibited by the specimen as follows:

    - 1) Specimens sectioned in the circumferential direction which contained a sonic indication exhibit rosette type failures. Fracture initiates at a small pore and is surrounded by a very flat cleavage-like facet which contained linear markings which can be correlated with the positions of alpha:beta interfaces. The size of this first facet is equivalent to the colony size. Continued growth also occurred in a cleavage mode although the cleavage facets are somewhat rougher and occasional regions of striations are observed. Again the cleavage facet size can be correlated with the colony size. A specimen tested in the radial direction exhibited the same fracture topography with the exception of the pore at the crack origin.

- 2) Dwell-tested specimens that contain no sonic indications exhibit many of the fracture features of the rosette-type failures with the exception of the central pore. Further, the nucleation (first) cleavage facet is less well defined.
- 3) Specimen tested at high frequency also show a faceted appearance at low magnification although the facet size is usually smaller than in the above cases, and have a rougher topography. At higher magnification striations are observed, if the crack growth occurred in air.
- 4) The specimens tested at 400°F under dwell condition and with a large beta grain size exhibit large featureless cleavage facets. The facet size is equivalent to the beta grain size.
- 5) Specimens with seeded flaws exhibit the same fracture features as monolithic specimen sectioned from the forging, with the exception of the crack nucleation site. Thus dwell testing resulted in well defined cleavage appearance while high frequency testing gives a rougher topography. Specimens tested at high frequency in which the fracture origin was subsurface did not show striations.

#### c. Analysis

- (1) The growth of cracks from subsurface origins in Ti-6Al-4V and Ti-6Al-2Sn-4Zr-2Mo appear to follow the established growth laws determined by fracture mechanics methodology. Surface cracks in smooth LCF specimens tested at high stress rates grow at rates compatible with these laws.
- (2) Chemical analysis of rosette origins in IMI 685 indicates that the only compositional anomaly is a higher nitrogen content. The seeding experiments on both Ti-6Al-4V and IMI 685 also indicate that local nitrogen contamination can produce marked degradation of fatigue properties.
- (3) The very low lives exhibited by IMI 685 tested under dwell conditions appear to be related to extremely easy subsurface crack nucleation. A completely satisfactory explanation of all structural and kinetic features of the crack nucleation process cannot be given.
- (4) The crack growth rates observed in small specimens of IMI 685 tested under high stresses do not follow the growth laws for the material established in fracture mechanics tests. Surface-nucleated cracks formed in high frequency tests grow at rates up to five times faster compared with the fracture mechanics data. More indirect evidence indicates that subsurface cracks grow at yet faster rates.
- (5) By combining information from several sources, including the fractographic results, a phenomenological model can be constructed which is consistent with the observed fatigue lives of dwell tested IMI 685.

### III BETA - FLECK DEFECTS

#### 1. Introduction

Another defect which has recently caused concern in Ti-6Al-4V is related to the segregation of solute elements which form the localized areas known as beta-flecks. Previous experience with such regions has shown that they are rich in beta stabilizing elements and lean in alpha stabilizing elements. This chemical heterogeneity results in different transus temperatures for different regions within a material and, on heating or forging at temperatures slightly below the normal beta transus temperature, regions of acicular microstructure are formed. Experience with such defects has been chiefly in alloys containing finite quantities of beta-eutectoid elements such as the alloys Ti-6Al-6V-2Sn (Fe, Cu), and beta alloys containing Cr, e.g., Ti-13V-11Cr-3Al, etc., although not unknown in the more common alpha:beta alloys, such as Ti-6Al-4V. The defects usually occur on a macroscopic scale and are often accompanied by alpha segregation in other locations. Such large scale regions are generally readily detected by standard NDI practices so that suspect material or components can be rejected. Potential problems can arise when flecks occur on a smaller scale as discussed below.

Only limited mechanical property data are available due to the scarcity of material with beta-flecks and the difficulty specimens containing beta-flecks in gage sections. However, in LCF testing of Ti-6Al-4V by Wyman-Gordon Company (20) two of a group of five specimens were found to contain beta-flecks. These two specimens exhibited a severe debit in LCF capability with respect to the other three specimens with a normal alpha:beta structure. The data showed that the flecked group had essentially zero life when compared with beta forged specimens. Considerably more data defining the effect of beta-flecks on the mechanical properties of the Ti-6Al-6V-2Sn (Ti-662) alloy are available from other sources. (20, 21) Based on existing data, it appears that the presence of beta-flecks does not have a great effect on tensile properties but has a fairly strong detrimental effect on LCF life. Forging low in the alpha:beta range, which essentially conceals the flecks, does not completely eliminate the LCF debit indicating that the mere presence of the chemically segregated areas may have adverse effects. (20)

More recently, there has been some concern over the occurrence of small scale beta-flecks in the alloy Ti-6Al-4V. The concern stems from one series of tests which indicated fatigue debits of up to two orders of magnitude in such flecked material. (22) However, there is some question about the specifics of the test methods used in this study and there is a suspicion that overloads in the initial part of a test may have resulted in these large fatigue debits.

It is clear that large scale beta-fleck regions are relatively easily detected using standard NDI inspection techniques that such flecked material can be subsequently withdrawn from any manufacturing cycle. However, small scale beta-flecks can only be detected by more sophisticated and detailed macro- and microstructural examination. The study of such small scale beta-flecks constitutes the second part of this investigation. The major objective of this study is to obtain a detailed insight into the effect of such regions on properties, especially for the fatigue behavior.

## 2. Experimental Methods and Results

### a. Characterization of Ti-6Al-4V Containing Beta-Fleck Defects

#### (1) Materials

Ti-6Al-4V alloy from two different sources have been used in this study. A 9" diameter, 12" long bar which has been determined to contain beta-fleck defects was procured from the Titanium Metal Corporation of America (TMCA). The bar was obtained from a 15" square billet section by a four-stage operation at 1750°F with reheating after each forging stage. This material will be referred to as billet material. The bar was sectioned longitudinally into two halves. A longitudinal slice from the center of one half was prepared for microstructural, chemistry, microhardness and heat treatment studies. Transverse slices were cut from the longitudinal halves and given a solution treatment of 1750°F for 1 hour followed by water quenching (WQ), except as noted in Table 26, and then aged at 1300°F for 2 hours followed by air cooling. The majority of the data in this report have been obtained using the billet material.

The macro- and microstructural characteristic of the longitudinal mid-section of the Ti-6Al-4V billet in the as-received condition is illustrated in Figure 55. The macrostructure consists of a core region of varying diameter (approximately 2-1/2"), within which structure coarser than the surrounding envelope is evident. The microstructure consists of varying amounts of primary alpha particles distributed heterogeneously in a matrix of an acicular mixture of the alpha and beta phases. The microstructural variation is primarily along the radial direction of the bar and it will be described in detail in the next section.

Beta-flecked material obtained from a second source was in the form of a pancake forging. The material had been alpha:beta forged and given the same heat treatment as that of the billet material except that air cooling was used following the solution treatment.

The macro- and microstructural characteristic of the Ti-6Al-4V pancake forging is shown in Figure 56. The beta-fleck defects are distributed primarily in the center region and defined by the plastic flow pattern of the forging. Table 16 shows a comparison of the metallurgical parameters for the Ti-6Al-4V billet and forging.

#### (2) Microstructure

Characterization of beta-fleck defects involves a description of the distribution of the defect, its volume fraction and severity. The latter is measured by the relative amounts of primary alpha particles (particle densities) in the defect and in the local microstructure. The most severe defect would be one completely devoid of primary alpha particles which is often referred to as a "nudie". Since a beta-fleck defect is microstructurally indistinguishable from the transformed beta-matrix in an alpha:beta forged material, it is recognizable only when it reaches a certain size. Therefore a quantitative description of a beta-fleck defect

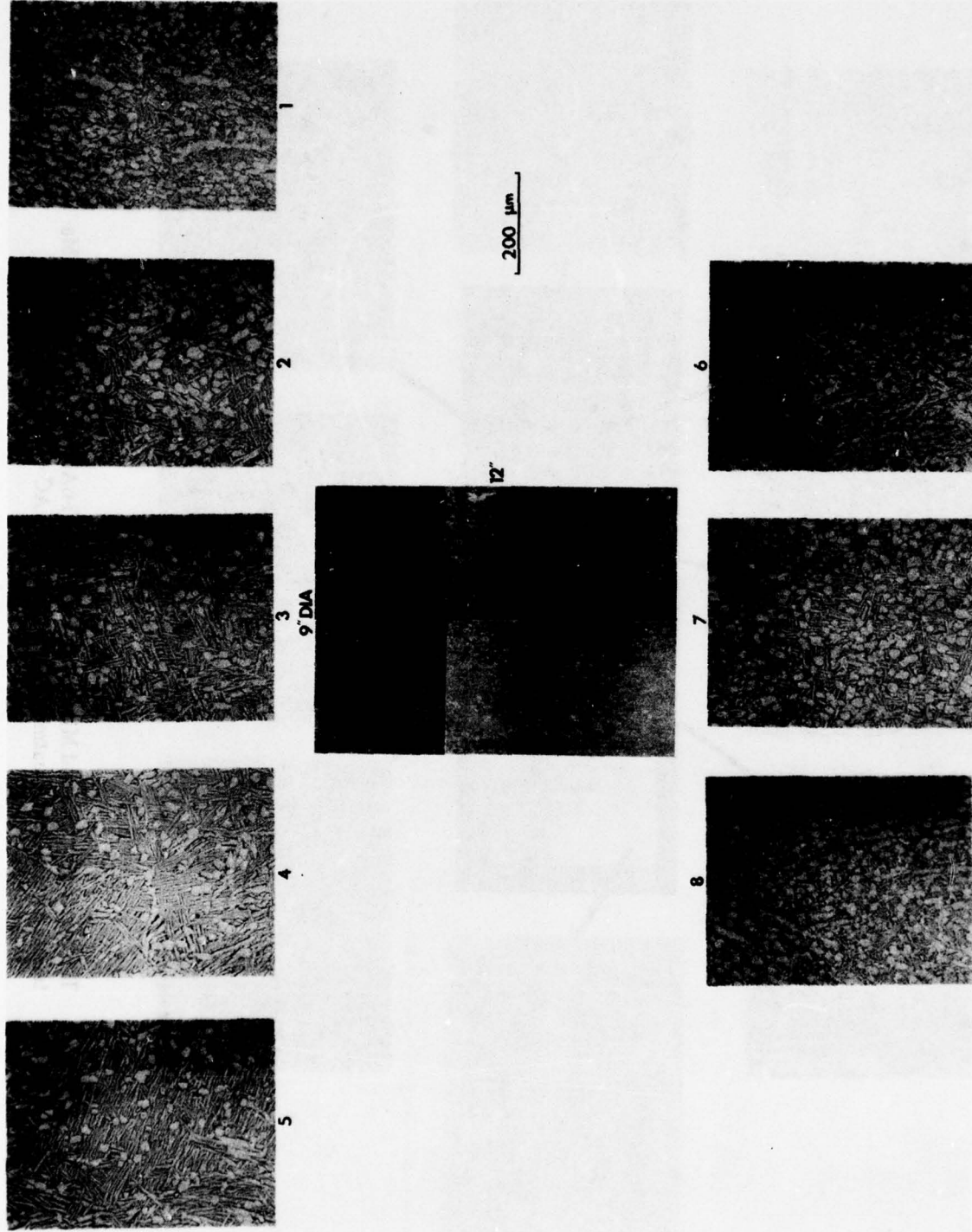


Figure 55 The Macrostructure and Microstructure of the Longitudinal Midsection of the Ti-6Al-4V Bar (TMCA Material) in the As-Received Condition

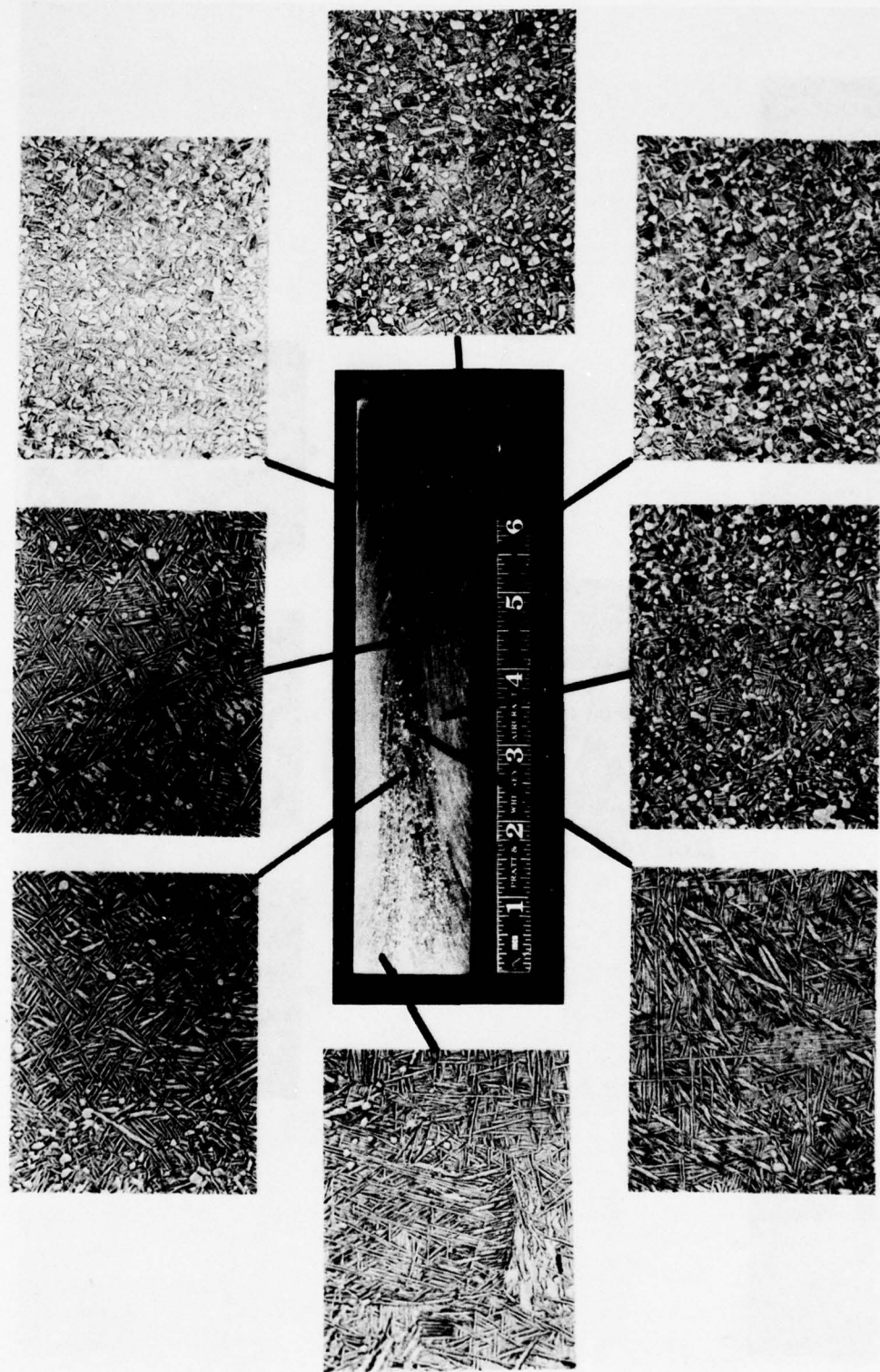


Figure 56 The Macrostructure and Microstructure of the Ti-6Al-4V Forging (P&WA Material) After a Heat Treatment of 1750F/1 hour AC + 1300F/2 hours AC.

TABLE 16  
Ti-6Al-4V  
METALLURGICAL PARAMETERS

Parameters	Billet		Forging	
	Normal	$\beta$ -Fleck	Normal	$\beta$ -Fleck
Primary $\alpha$ Particle Size (mm)	0.017	0.019	0.015	0.017
Secondary $\beta$ Grain Size (mm)	0.07	*	0.02	0.05
Prior $\beta$ Grain Size (mm)	0.4	0.9	*	0.2

\*not obvious in the microstructure

involves definitions of both the minimum difference in primary alpha particle densities between the region considered and its local microstructure and the minimum area of the region above which it can be described as a beta-fleck defect. These definitions are necessarily arbitrary. The definitions of a beta-fleck defect in the present work are as follows:

- 1) The primary alpha particle density,  $d_{\alpha}$  is 50% less than that of the bulk microstructure,  $\bar{d}_{\alpha}$ . Such a region is called type A fleck. If  $d_{\alpha} \leq 0.2 \bar{d}_{\alpha}$ , then the beta-fleck is called type B.
- 2) The primary alpha particle-deficient region must have an area  $\geq 25 \bar{l}^2$ , where  $\bar{l}$  is the average spacing of the primary alpha particle in the local microstructure.

Lineal analysis was performed to determine the average primary alpha particle densities, spacings and the beta-fleck volume fractions at various locations in the Ti-6Al-4V billet. These measurements were made on the billet in as-received conditions.

Quantitative metallographic results on the billet are given in Table 17. The volume fraction of primary alpha is the highest near the surface, decreases to a minimum near the half radius location, and then increases toward the center. The beta-fleck volume fraction is zero near the surface, highest near the half-radius location, and then decreases slightly toward the center. However, the beta-fleck is more severe near the center where 17% of the total beta-fleck volume fraction is of B type. No type B beta-fleck has been found at the half-radius location. Quantitative metallographic results of a center sample at a normal location and a type B "nudie" location is given in Table 18.

Vickers microhardness measurements were used to ascertain the possible strength variation on regions containing beta-fleck defects. Further, to study the possible load dependence of the microhardness, loads of 50g (grams), 100g and 200g were used. Using a 50g load, the size of the hardness indentations is about the same as that of the primary alpha particle. Indentations were made randomly in locations with the normal microstructure and in the beta-fleck locations where the densities of primary alpha were the lowest.

TABLE 17

**QUANTITATIVE METALLOGRAPHIC RESULTS OF THE  
Ti-6Al-4V BILLET IN THE AS-RECEIVED CONDITION**

Location	Average Primary Alpha Data			Total (Types A & B) $\beta$ -Fleck Volume Fraction
	Particle Size ( $\mu\text{m}$ )	Spacing ( $\mu\text{m}$ )	Volume Fraction	
Surface	16.7	34	0.190	0
Half-Radius	17.5	52	0.116	0.115
Center	19.2	45	0.144	0.085

TABLE 18

**QUANTITATIVE METALLOGRAPHIC RESULTS OF Ti-6Al-4V  
BILLET CENTER IN THE AS-RECEIVED CONDITION**

Location	Primary $\alpha$	Volume Fraction	
		$\alpha$ Platelet	$\beta$ Platelet
Normal	0.144	0.690	0.166
B Type 'Nudie'	0	0.863	0.137

The results of the microhardness measurements are given in Tables 19. The Vickers Hardness Number (VHN) is almost independent of the load used (50g to 200g); the tabulated data were obtained using a load of 100g. There are no significant variations between the VHN at the normal structure and the beta-fleck structure. The magnitude of the variations is about the same as that among the normal microstructures between the surface, half radius and the center regions.

TABLE 19

**MICROHARDNESS OF Ti-6Al-4V BILLET  
IN THE AS-RECEIVED CONDITION**

Location	Normal Structure		VHN $\beta$ -Fleck Structure	
	No. of Indentations	Average	No. of Indentations	Average
Surface	9	329	None	
Half-Radius	9	353	2	379
Center	9	335	6	322

### (3) Chemical Analysis

To correlate the microstructural variation to the possible chemical segregation of the alpha stabilizers (Al, O, C and N) and the beta stabilizers (V, Fe and H), samples were taken from the billet material at locations near the surface, half-radius and center. Chemical analysis was performed by electron microprobe and by conventional chemistry techniques to establish the extent of the partitioning of elements between the primary alpha, the acicular alpha in the normal and the beta-flecked regions and for the segregation of elements between the center and the surface locations. The average (alpha-beta) compositions of a center sample at a normal location and a beta-flecked location were determined by microprobe techniques using a defocused beam size of about 100  $\mu\text{m}$  diameter.

Compositions of the alpha phase are summarized in Table 20. The microprobe results show that, for a given location, the Al contents are the highest in the primary alpha and the lowest in the acicular alpha in the beta-flecked location; the reverse is true for V. However, the differences in Al and V contents among the acicular phase at different locations are small. Fe was not detected in the primary alpha or in the acicular alpha at either the normal or the beta-flecked locations; the element was found in the beta phase.

Because of the fineness of the beta phase, its compositions could only be determined reliably after a selective electrochemical dissolution of the alpha phase. The electrolyte used consisted of 1 liter methanol, 3 g succinic acid and 3 ml concentrated sulfuric acid and used at a current density of about 50 milli-ampere per  $\text{cm}^2$  and at a temperature of 40-50°F.

TABLE 20  
COMPOSITIONS (WT. PERCENT) OF THE ALPHA PHASE IN THE Ti-6Al-4V  
BILLET IN THE AS-RECEIVED CONDITION

Element	Avg. Chem. From TMCA	Surface			Half Radius			Center		
		Primary $\alpha$	Normal Micros. $\alpha$	Avg. Chem. $\alpha + \beta$	Primary $\alpha$	Normal Micros. $\alpha$	$\beta$ -Fleck $\alpha$	Primary $\alpha$	Normal Micros. $\alpha$	$\beta$ -Fleck $\alpha$
Al	6.40	7.77	7.38	6.40	7.80	7.67	7.47	7.73	7.40	7.37
V	4.20	2.17	2.88	4.18	2.20	2.63	2.80	2.20	2.63	2.93
Fe	0.13	ND	ND	0.10	ND	ND	ND	ND	ND	0.16
O	0.173	--	--	0.170	--	--	--	--	--	0.150
C	0.022	--	--	0.008	--	--	--	--	--	0.010
N	0.016	--	--	0.011	--	--	--	--	--	0.008
H	0.002	--	--	0.007	--	--	--	--	--	0.004

ND = Not detected

-- = No determination made

The morphologies of the beta phase in a center sample at a beta-flecked location and at a normal location are shown in Figure 57a and b, respectively. The concentrations of Al, V and Fe in the beta phase at a beta-flecked location were determined to be, respectively, 0.5, 1.25 and 1.5 times those at the normal location. From these relative concentrations and the quantitative metallographic results, the compositions of the beta phase and the average (alpha + beta) compositions at these two locations in the center sample were calculated. The results are summarized in Table 21.

A center sample was also studied by secondary ion mass spectrometry technique. Mass spectra were obtained at a beta-flecked band at a normal area using either  $^{32}\text{O}^+$  ions or  $^{28}\text{N}^+$  ions after a sputtering of 15 to 30 minutes. The reduction and therefore interpretation of the data are subject to the same limitations described previously in the cleavage rosette studies. To determine the spatial distribution, secondary ion images of V, Fe, O, N, C and H were also taken at the normal and beta-flecked areas.

The compositions that were measured after sputtering for 15-30 minutes are given in Table 22. The segregation pattern of the alpha stabilizing and beta stabilizing elements in the normal and beta-flecked regions is not clear using this technique. The beta-flecked region contains a higher concentration of beta stabilizing Fe and a lower concentration of alpha stabilizing C. On the other hand, the normal region contains higher concentrations of H and Cr both of which are beta stabilizers. The other elements present appear to be due to residual contamination. Selected secondary ion images are shown in Figure 58. In Figure 58a and b the light areas correspond to the beta phase while the dark area corresponds to the alpha phase. It appears from Figure 4b that the change in V concentrations between alpha and beta phases is a gradual one. Similar observations can be made on Fe (Figure 58c).

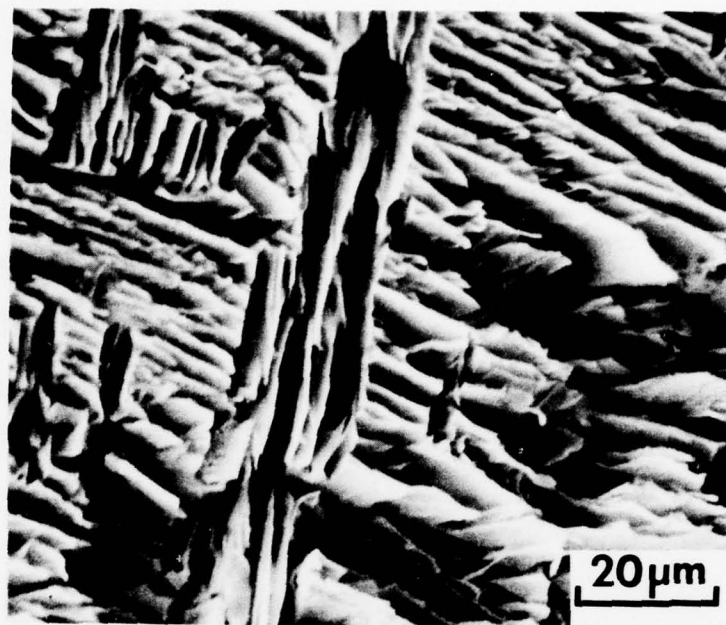
The bulk chemistry (Table 20) shows that there is a significant difference in the Fe contents between the surface and the center locations, which are, respectively, 0.10 and 0.16%. This result has been verified by microprobe technique using a defocused electron beam of  $100\mu\text{m}$  diameter. A difference in the average Fe content between a beta-flecked location and a normal location in the center sample was not detected by this microprobe technique.

The interstitials (O, C, N and H), which cannot be adequately measured in the microprobe, were analyzed by conventional chemistry techniques. The results indicate that the alpha stabilizers, O and N, and the beta stabilizer, H, are higher near the surface than the center. The center contains a higher C which is an alpha stabilizer.

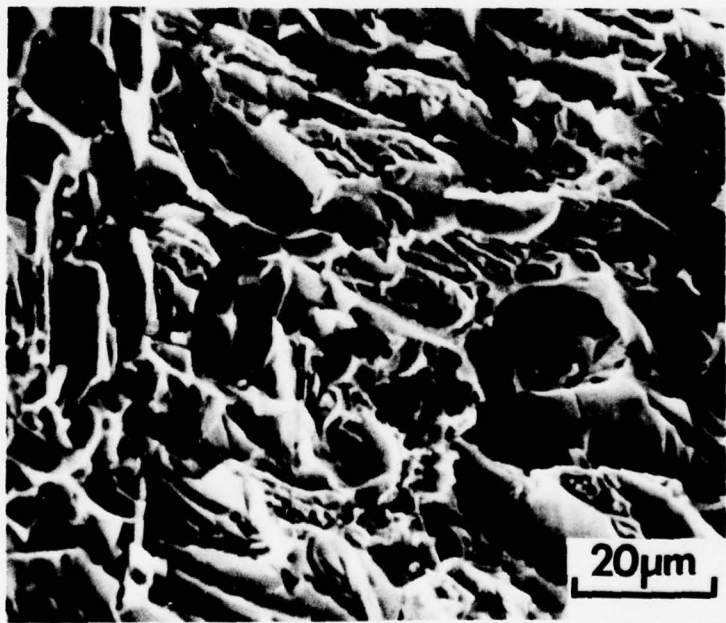
#### (4) Thermo-mechanical Processing/Heat Treatment Studies

In a conventional forging operation, the surface of a bar would experience a larger amount of deformation at a lower temperature than the center of the bar. To examine the possible contribution of this temperature and deformation gradient to the microstructural variation observed (Figures 55 and 56), and to investigate the potential variation of the heat treatment response, the microstructural changes of the surface and center samples were studied after the following thermomechanical treatment:

- 1) Exposure for 1 hour at temperatures of  $1750^\circ\text{F}$ ,  $1780^\circ\text{F}$ ,  $1810^\circ\text{F}$  and  $1830^\circ\text{F}$ .
- 2) Isothermal forging of a center sample at  $1675^\circ\text{F}$  to a strain of 130% followed by exposure for 1 hour at  $1780^\circ\text{F}$ .



a



b

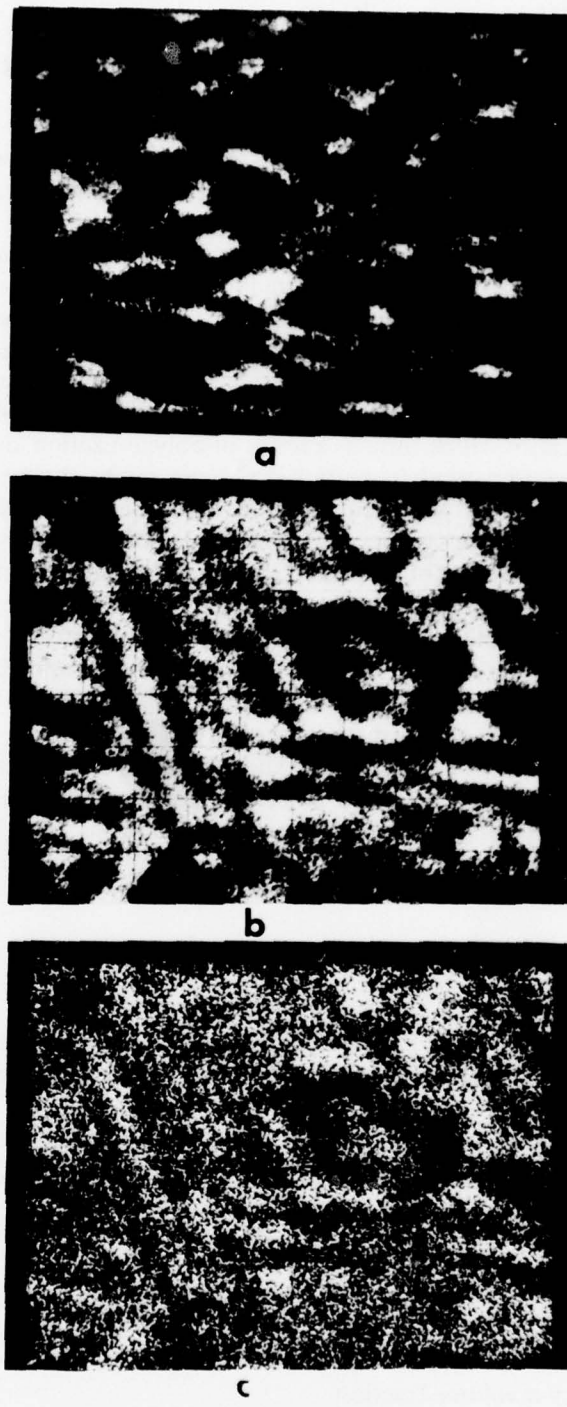
**Figure 57** Scanning Electron Micrographs Showing the Morphologies of the Beta-Phase in the Center of the Ti-6Al-4V Bar at (a) a Beta-Fleck Location and (b) a Normal Location

TABLE 21  
COMPOSITION (w/o) OF THE BETA-PHASE IN THE BILLET CENTER  
IN THE AS-RECEIVED CONDITION

	Bulk	$\beta$ -Fleck Location		Normal Location	
		$\beta$ -Phase	Average	$\beta$ -Phase	Average
Al	6.50	0.90	6.46	1.80	6.51
V	4.35	14.90	4.57	11.90	4.10
Fe	0.16	1.42	0.20	0.95	0.16

TABLE 22  
SECONDARY ION MICROPROBE RESULTS  
Ti-6Al-4V BILLET CENTER  
(ppma)

<u>Element</u>	<u>Normal Region</u>	<u>Beta-flecked Region</u>
B	44	21
C	456	377
Na	63	261
Mg	861	895
K	9	12
Ca	52	46
Cr	61	50
Fe	1200	1300
H (relative ion intensities) Ti = 1.0	.0037	.0036



**Figure 58** (a) 51 V Image of a Normal Area  
(b) 51 V Image of a Beta-Flecked Area  
(c) 56 Fe Image of a Beta-Flecked Area

The temperature control in all the experiments was  $\pm 5^{\circ}\text{F}$ . The forging was performed in an Instron Machine and boron nitride was used as a lubricant.

The results of heat treatment of the surface and the center samples for one hour at temperatures of  $1750^{\circ}\text{F}$ ,  $1780^{\circ}\text{F}$ ,  $1810^{\circ}\text{F}$  and  $1830^{\circ}\text{F}$  are given in Table 23. As expected, the primary alpha volume fraction decreases with increasing temperature. In the surface samples the decrease in primary alpha particle density occurred rather uniformly throughout the entire specimen. Thus, no beta-fleck defects were produced. At  $1830^{\circ}\text{F}$  there were 2% primary alpha particles left in the surface sample while all the primary alpha particles had solutioned in the center sample. The beta transus of the surface sample was determined to be  $1835^{\circ}\text{F}$ . The prior beta grain sizes which should not be changed by the sub-transus heat treatment, were 0.4 mm and 0.9 mm in the surface and the center of the Ti-6Al-4V bar, respectively. The secondary beta grains which form as a result of polygonization and recrystallization occurring between the primary alpha particles<sup>(23)</sup> were rarely observed in the center samples, suggesting perhaps, the lack of sufficient amounts of mechanical working in the center region of the bar. Even in the surface samples, the detection of the secondary beta grains was rather difficult because of the absence of a distinct layer of alpha outlining their boundaries. The secondary beta grain sizes in the surface samples were estimated to be 0.07 mm and 0.12mm after one hour at  $1750^{\circ}\text{F}$  and  $1810^{\circ}\text{F}$ , respectively. The microstructure of the center sample after isothermally forged at  $1675^{\circ}\text{F}$  to a strain of 130% is shown in Figure 59a. This microstructure appears to be typical of alpha:beta worked material. The beta-fleck defects that were present before forging could not be distinguished. The corresponding microstructure after one hour at  $1780^{\circ}\text{F}$  is shown in Figure 59b. The apparently normal microstructure has reverted to the beta-flecked structure after this treatment. Furthermore, the presence of the secondary beta grain after the heat treatment becomes obvious, especially when observed at higher magnification, indicating the important role of plastic working on the formation of the secondary beta grains.

TABLE 23  
METALLURGICAL PARAMETERS OF Ti-6Al-4V BILLET AFTER  
ONE HOUR AT VARIOUS TEMPERATURES

	1750°F				1780°F				1810°F				1830°F			
	$\alpha$ v/o	SBG	PBG	$\alpha$ v/o	SBG	PBG	$\alpha$ v/o	SBG	PBG	$\alpha$ v/o	SBG	PBG	$\alpha$ v/o	SBG	PBG	
Surface	19.0	0.07	0.4	13.5	--	0.4	9.3	0.12	0.4	2.0	--	0.5				
Center	14.4	--	0.9	10.1	--	0.9	6.0	--	0.9	0.0	--	1.1				

- $\alpha$  v/o = Primary  $\alpha$  volume fraction
- SBG = Secondary  $\beta$  grain size (mm)
- PBG = Prior  $\beta$  grain size (mm)
- = Not observed

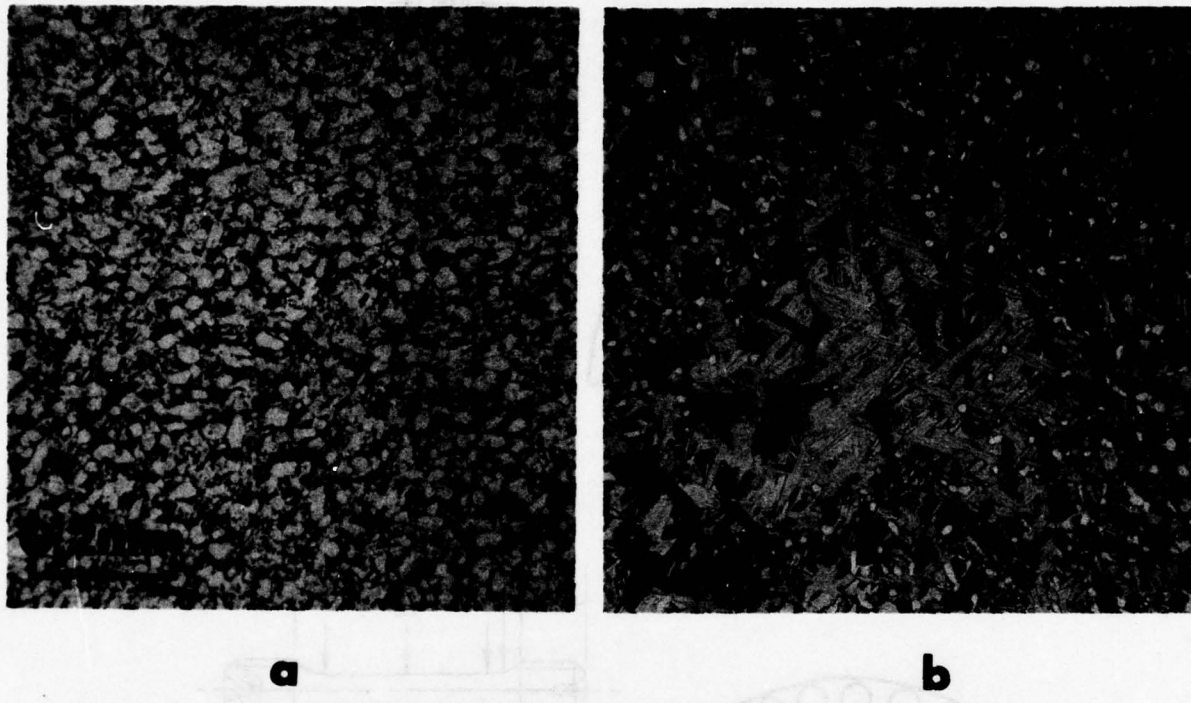


**Figure 59** The Microstructure of a Center Specimen Isothermally Forged at 1675°F to a Strain of 130%. (a) before and (b) after heat treatment for one hour at 1780°F.

#### b. Mechanical Properties Characterization

Specimens for tensile, stress-controlled and strain-controlled LCF tests were machined from the billet material. These specimens were machined from the center (beta-flecked) and near the surface (normal equiaxed alpha:beta) of the transverse slices where the microstructures showed the largest variation. The orientation of the specimens relative to that of the bar and their dimensions are shown in Figure 60.

##### (1) Tensile Properties

The tensile specimens (Figure 60d) were tested at room temperature in the as-machined surface condition. The results are presented in Table 24 from which it can be seen that the main difference between specimens with and without beta-fleck defects is in the tensile ductility. The former have slightly lower ductility than the latter.

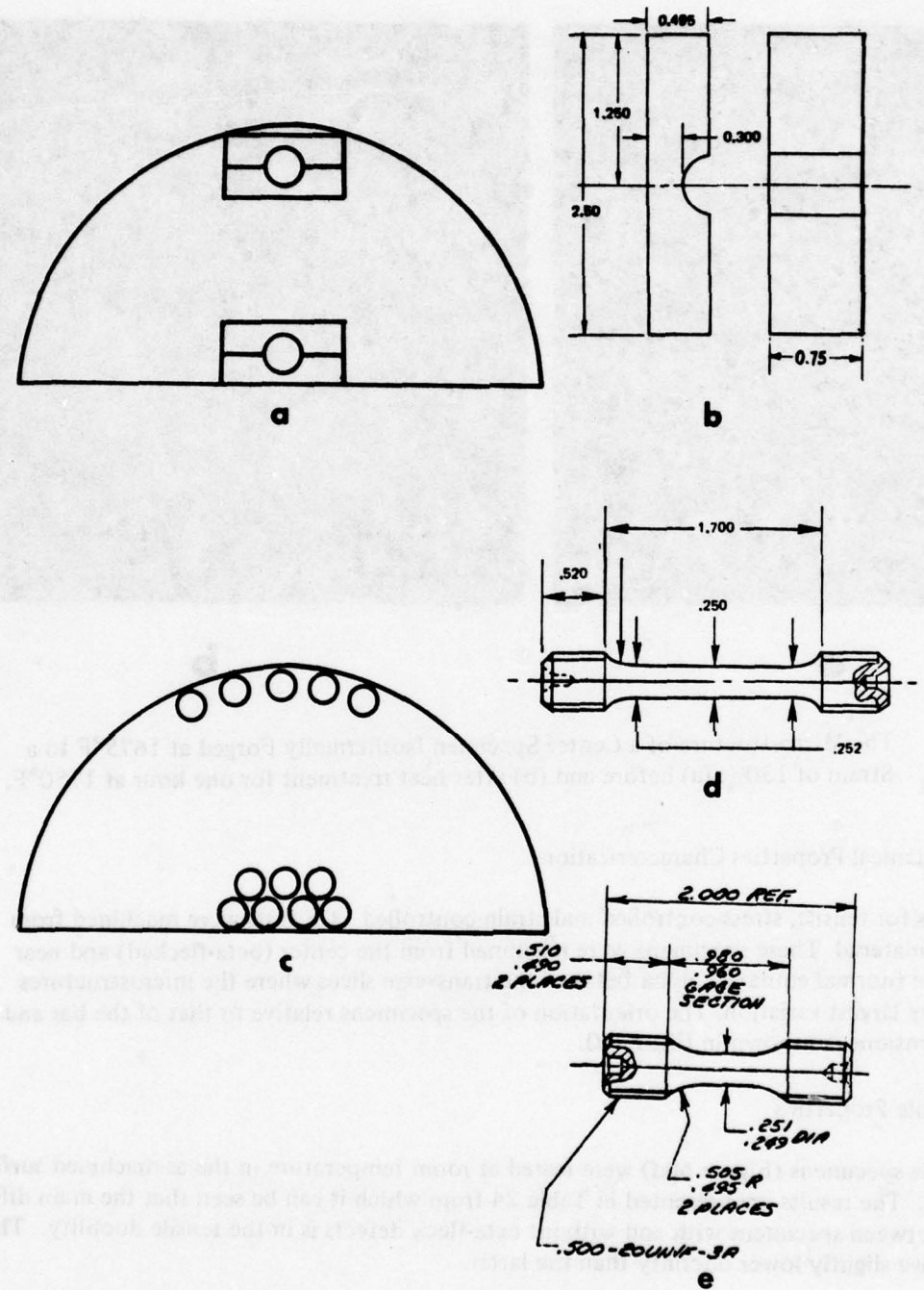


Figure 60 Orientations of the Half Bolt Hole Specimens (a) and Tensile and LCF Specimens (c) relative to the transverse slices cut from the longitudinal halves of a Ti-6Al-4V bar. The dimensions of these specimens are given in (b), (d) and (e), respectively.

TABLE 24  
RESULTS OF TENSILE TESTING  
Ti-6Al-4V Billet

<u>Specimen No.</u>	<u>Micro-Structure</u>	<u>0.2% YS (Ksi)</u>	<u>U.T.S. (Ksi)</u>	<u>% Elong.</u>	<u>% RA</u>	<u>Elastic Modulus (<math>10^6</math> psi)</u>
F-10	Normal	143.7	154.2	16.0	30.3	—
G-10	Normal	141.4	149.1	18.0	42.2	17.0
F-7	$\beta$ -Fleck	141.0	147.9	13.6	27.4	17.4
F-7-1	$\beta$ -Fleck	—	148.9	14.6	26.4	17.1

— Recorder Malfunction

#### (2) Strain-Controlled LCF Properties

Two types of specimens were used to evaluate LCF properties in strain-controlled tests, a notch-type and a smooth-type. Specimens which contain semi-circular notches ( $K_t = 2$ ) in the gage sections, half bolt hole specimens, shown in Figure 60b were chosen since they provide the maximum volume of test material and therefore circumvent the material sampling problem usually associated with specimens such as notched round bar or bolt hole type. This specimen also simulate the local stresses as encountered in notched details of fan and compressor disks. For smooth-type tests, a miniature version of the Krouse specimen (mini-Krouse) shown in Figure 61 was used. The half bolt hole specimens were machined from both the billet and the forging while the mini-Krouse specimens were machined from the forging only. Most of the strain-controlled LCF data has been collected using the half bolt hole specimens. The mini-Krouse specimens which were tested toward the end of this program were intended to facilitate the X-ray measurement of cyclic relaxation of surface residual stress in specimens with and without beta-fleck defects.

The half bolt hole specimens were tested at room temperature in a bending mode at cyclic strain ranges of 0-0.007 and 0-0.009. A frequency of 6 seconds per cycle (3 seconds at maximum strain) was used. The tests were interrupted for surface crack inspection at 500 cycle intervals. To determine the effects of surface residual stress on LCF crack nucleation, LCF specimens were tested in three different surface conditions: stress-relieved and electro-polished surface, as-machined surface and stress-relieved plus glass bead peened surface (6N intensity). Stress relieving was performed at 1100°F for 2 hours in a vacuum of  $10^{-6}$  torr. Electropolishing was accomplished in an electrolyte consisting of 95% methanol and 5% perchloric acid at -40°F using 16 volts. A surface layer of approximately 0.002" was removed from the specimen.

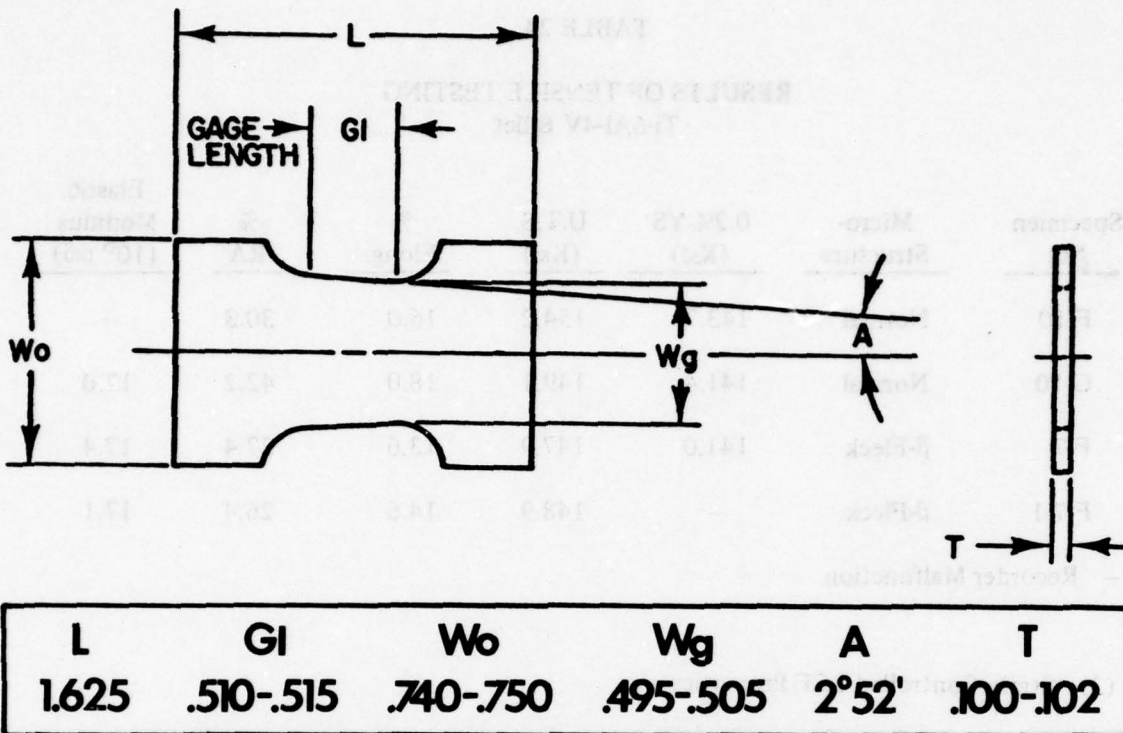


Figure 61 Dimensions of the Mini Krouse Specimen

Results are as follows:

(a) Effect of Surface Preparation

The effect of surface preparation on 'pinpoint' crack nucleation life in half bolt hole specimens from the Ti-6Al-4V billet and forging are given in Table 25. A 'pinpoint' crack refers to an indication whose length is near the limit of detectability by Zyglo inspection techniques, which is about 0.005". As shown in this Table there is no effect of beta-fleck defects on crack nucleation life in either the billet or the forging when tested with stress-relieved and electropolished surface condition (SR). It is also interesting to note that the forging has a longer crack nucleation life than the billet. This difference seems to be attributable to the differences in processing/microstructure since the forging has similar heat treatment as the billet and that there are no significant differences in composition in these two materials.

The fatigue debits in the beta-flecked material, especially the forging, become obvious when surface residual stress is present, i.e., in the as-machined (A-M) and stress-relieved and peened (GB-6N) surface conditions. In these surface conditions the crack nucleation lives of the forging with beta-fleck defects are about 50-60% lower than the corresponding values in the defect-free (normal) microstructure. The fatigue debits of the beta-fleck defects in the billet appear to be less than those in the forging. In GB-6N surface condition, the nucleation lives in the normal and beta-flecked microstructures of the billet are longer than the corresponding ones in the forging. This reversal in fatigue capabilities between these two materials suggests a complicated interaction of microstructure with surface residual stress.

TABLE 25  
**EFFECTS OF SURFACE PREPARATION ON CRACK INITIATION  
 IN Ti-6Al-4V HALF BOLT HOLE SPECIMENS**  
 70°F, 0-0.009 $\epsilon$ , 10 cpm

Specimen Number	Micro-Structure	Heat Treatment	Surface Preparation	Cycles to 'Pin-Point' Crack Indication
<b>Billet</b>				
A-1	$\beta$ -Flecked		Stress Relieved	1,500
A-2	$\beta$ -Flecked	WQ	and	1,500
A-4	Normal		Electropolished	1,500
B-3	Normal			1,500
D-1	$\beta$ -Flecked		Stress Relieved	118,000
D-2	$\beta$ -Flecked	WQ	and	86,000
D-3	Normal		Glass Bead	118,000
D-4	Normal		Peened (6N)	124,000
<b>Forging</b>				
13-A	$\beta$ -Flecked	WQ	Stress Relieved	3,500
14-B	$\beta$ -Flecked	AC	and	3,500
19-B	Normal	AC	Electropolished	3,500
9-A*	$\beta$ -Flecked	AC	As-Machined	6,000
11-A*	$\beta$ -Flecked	AC	As-Machined	7,000
12-A*	$\beta$ -Flecked	AC	As-Machined	7,000
15-B*	$\beta$ -Flecked	AC	As-Machined	7,000
18-B*	$\beta$ -Flecked	AC	As-Machined	9,000
1-A*	Normal	AC	As-Machined	15,000
2-A*	Normal	AC	As-Machined	16,000
5-A*	Normal	AC	As-Machined	15,000
6-A*	Normal	AC	As-Machined	19,000
7-A*	Normal	AC	As-Machined	25,000
32-T	$\beta$ -Flecked	AC	Stress Relieved	26,000
32-B	$\beta$ -Flecked	AC	and	58,000
23-T	Normal	AC	Glass Bead	94,000
23-B	Normal	AC	Peened (6N)	83,000

\* Ref. (24)

$$WQ = 1750^{\circ}\text{F}/1 \text{ hr}/WQ + 1933^{\circ}\text{F}/2 \text{ hr}/AC$$

$$AC = 1750^{\circ}\text{F}/1 \text{ hr}/AC + 1300^{\circ}\text{F}/2 \text{ hr}/AC$$

The difference in the crack nucleation life between the billet and forging disappears after a beta-heat treatment which also reduces the crack nucleation life, Table 26. Figure 62 summarizes results presented in Tables 25 and 26. The bars on the data points represent the maximum scatter in either LCF or surface residual stress data.

TABLE 26  
CRACK INITIATION LIFE IN BETA PHASE  
TREATED Ti-6Al-4V HALF BOLT HOLE SPECIMENS  
70°F, 0-0.009 $\epsilon$ , 10 cpm

<u>Specimen Number</u>	<u>Micro-Structure</u>	<u>Heat Treatment</u>	<u>Surface Preparation</u>	<u>Cycles to 'Pin-Point' Crack Indication</u>
B-2(1)	$\beta$ -Flecked	B	Stress Relieved and Electropolished	1,000
A-3(1)	Normal	B	Stress Relieved and Electropolished	500
14-A(2)	$\beta$ -Flecked	B	Stress Relieved and Electropolished	1,500
19-A(2)	Normal	B	Stress Relieved and Electropolished	1,000
(3)	Normal	AC	As-Machined	2,000 to 4,000

(1) Billet

(2)  $\alpha$ - $\beta$  forged pancake

(3)  $\beta$ -forged pancake, Ref. (25)

B: 2190°F/10 min/FC + 1300°F/2 hr/AC

AC: 1750°F/1 hr/AC + 1300°F/2 hr/AC

#### (b) Effects of Strain Range

The effects of strain ranges 0-0.007 and 0-0.009 on crack nucleation in Ti-6Al-4V half bolt hole specimens have been evaluated only on specimens with a stress-relieved and electro-polished surface condition. The results are given in Table 27. At the lower strain range the beta-flecked microstructures have cracks nucleation lives longer than those in the normal microstructures by a factor of at least four. As mentioned previously, at the higher strain level no difference in crack nucleation life between the normal and beta-flecked microstructures is observed.

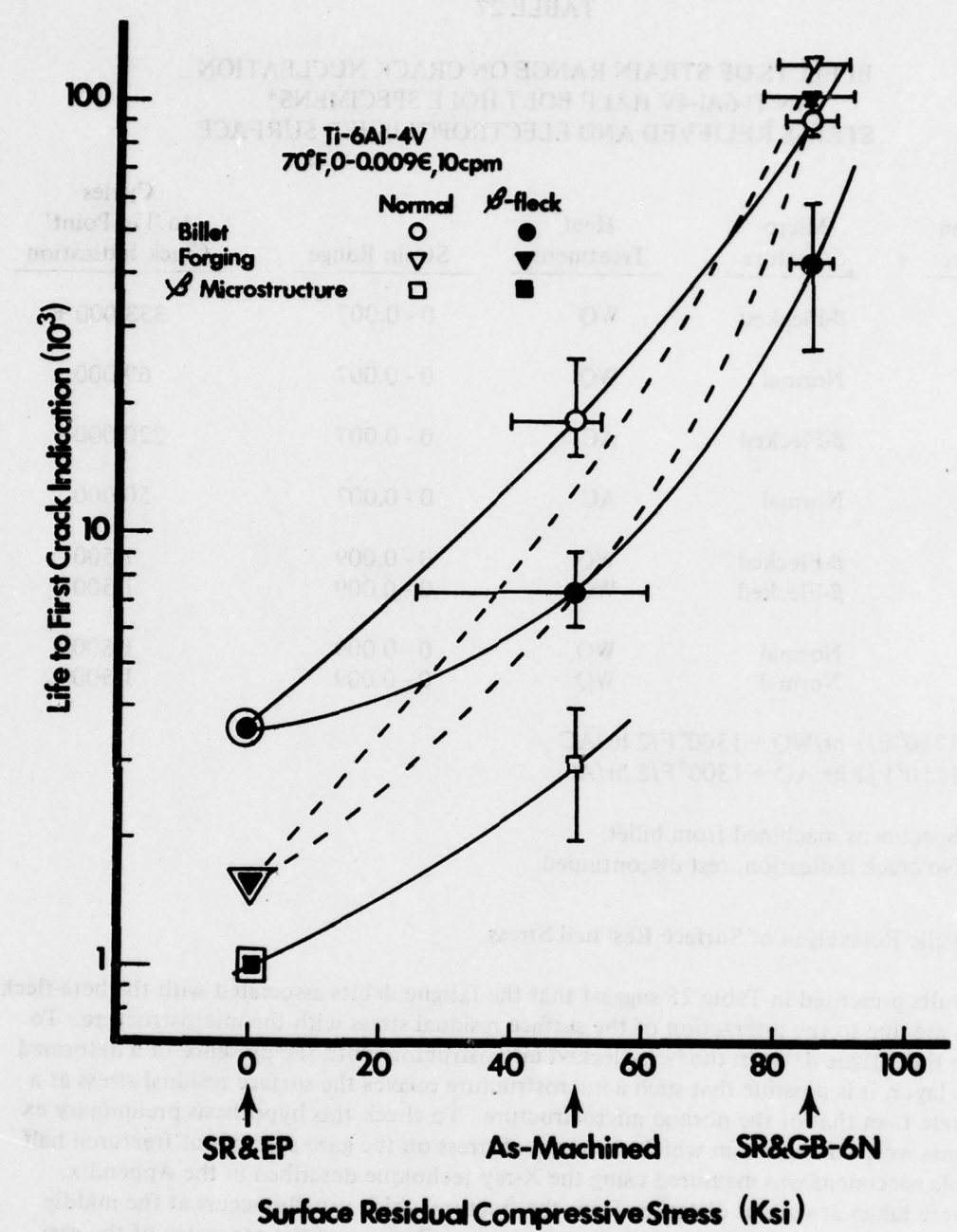


**Figure 62** Fatigue Crack Initiation Lives of Normal and Beta-flecked Ti-6Al-4V as a Function of Surface Preparation. The specimens were tested in strain-controlled LCF at 0.9% $\epsilon$ .

TABLE 27

EFFECTS OF STRAIN RANGE ON CRACK NUCLEATION  
IN Ti-6Al-4V HALF BOLT HOLE SPECIMENS\*  
STRESS RELIEVED AND ELECTROPOOLISHED SURFACE

Specimen Number	Micro-Structure	Heat Treatment	Strain Range	Cycles to 'Pin-Point' Crack Indication
C-1	$\beta$ -Flecked	WQ	0 - 0.007	333,000 +
C-4	Normal	WQ	0 - 0.007	69,000
E-1	$\beta$ -Flecked	AC	0 - 0.007	220,000
E-4	Normal	AC	0 - 0.007	50,000
A-1	$\beta$ -Flecked	WQ	0 - 0.009	1,500
A-2	$\beta$ -Flecked	WQ	0 - 0.009	1,500
A-4	Normal	WQ	0 - 0.009	1,500
B-3	Normal	WQ	0 - 0.009	1,500

WQ: 1750°F/1 hr/WQ + 1300°F/2 hr/AC

AC: 1750°F/1 hr/AC + 1300°F/2 hr/AC

\* Specimens machined from billet.

+ No crack indication, test discontinued.

## (c) Cyclic Relaxation of Surface Residual Stress

The results presented in Table 25 suggest that the fatigue debits associated with the beta-fleck defects are due to the interaction of the surface residual stress with the microstructure. To explain the fatigue debit in the beta-flecked microstructure with the presence of a deformed surface layer, it is possible that such a microstructure relaxes the surface residual stress at a faster rate than that of the normal microstructure. To check this hypothesis preliminary experiments were conducted in which the residual stress on the gage surfaces of fractured half bolt hole specimens was measured using the X-ray technique described in the Appendix. Data were taken at various distances from the fracture which usually occurs at the middle of the gage section where the strain is the maximum. Because of the geometry of the gage section, these measurements in effect yield information on the cyclic relaxation of surface residual stress as a function of strain amplitude. Results from these preliminary experiments are given in Table 28 and illustrated in Figure 63. For each specimen measurements were taken at locations A, B and C in the order of proximity to the fracture, location C being the closest to the fracture. As anticipated, the residual stress decreases toward the fracture. The important difference between the beta-flecked and normal microstructures is that residual tensile stress was measured near the fracture in the former while the residual stress remained compressive in the latter.

TABLE 28

**SURFACE RESIDUAL STRESSES IN AS-MACHINED Ti-6Al-4V  
HALF BOLT HOLE SPECIMENS AFTER TESTING**

Micro- Structure (S/N) <sup>+</sup>	No. of Cycles to First Crack Initiation	Stresses (Ksi) at Location*		
		A	B	C
$\beta$ -Flecked (9A)	6,000	- 2.0	+ 1.5	+ 3.0
$\beta$ -Flecked (15B)	7,000	- 48.0	- 40.0	+ 12.0
Normal (6A)	19,000	- 32.0	- 24.0	- 17.0
Normal (7A)	25,000	- 16.7	- 14.5	- 1.7

\* See Figure 63

+ Specimen Number

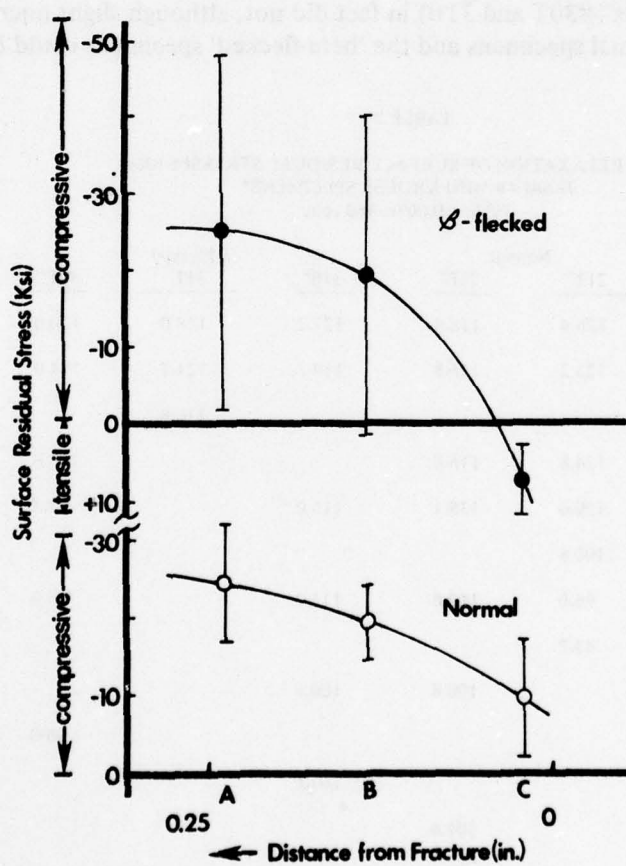


Figure 63 Surface Residual Stresses at Various Distances From the Fracture Surface of Half Bolt Hole Specimens With and Without Beta-Fleck Defects

The results described above led to two series of tests designed to obtain data on cyclic relaxation of surface residual stress after various numbers of cycles. One series involves stress-controlled LCF testing which will be described in Section III.2.b.(3), the other series involves strain-controlled testing using sheet-type mini-Krouse bend specimens shown in Figure 56. These specimens were tested at room temperature with stress-relieved and glass-bead peened (6N) surface condition in reversed bending at a maximum strain of 0.009 and a frequency of 460 cycles per minute. Results from mini-Krouse specimens are presented in Table 29 and illustrated in Figure 64 in which the stresses are normalized to the initial value of 100 ksi. Figure 64 shows that in the normal microstructure the surface residual stress decreases very slowly until about  $5 \times 10^4$  cycles. Thereafter, a precipitous drop is observed. The beta-flecked microstructure behaves in a similar manner except that it relaxes the surface residual stress more rapidly in the first one thousand cycles. 'Pinpoint' cracks were detected after the onset of the rapid stress relaxation. The number of cycles to 'pinpoint' crack indications are  $5.2 \times 10^4$ ,  $6.8 \times 10^4$  and  $7.4 \times 10^4$  for specimens # 21T, 21B, and 31B, respectively. Specimens # 31T and 30T fractured in the grip area after  $3.95 \times 10^4$  and  $7.2 \times 10^4$  cycles, respectively. No 'pinpoint' crack was observed in these two specimens prior to fracture. Thus the anticipated fatigue debit of the beta-flecked microstructure failed to materialize in this series of tests. Detailed post-test analysis revealed that the specimens that were assumed to contain beta-flecks (#30T and 31B) in fact did not, although slight microstructural difference between the normal specimens and the 'beta-flecked' specimens could be detected.

TABLE 29

CYCLIC RELAXATION OF SURFACE RESIDUAL STRESSES (-Ksi)  
Ti-6Al-4V MINI-KROUSE SPECIMENS\*  
 $70^\circ\text{F}$ ,  $\pm 0.009\epsilon$ , 460 cpm

Cycles	Normal		$\beta$ -Flecked		$30^\circ\text{T}$
	$21T^\circ$	$21B^\circ$	$31B^\circ$	$31T^\circ$	
0	126.4	118.4	127.2	128.0	120.0
$1 \times 10^3$	123.2	116.8	119.2	121.7	114.0
$3.95 \times 10^4$				116.8	
$5 \times 10^3$	124.8	116.8			113.6
$5 \times 10^4$	120.0	115.1	116.0		97.3
$5.2 \times 10^4$	100.8				
$5.4 \times 10^4$	96.0	109.6	111.2		96.0
$5.6 \times 10^4$	83.2				
$5.8 \times 10^4$		100.8	100.8		
$6 \times 10^4$					96.0
$6.2 \times 10^4$			101.6		
$6.4 \times 10^4$		101.6			

\* Machined from  $\alpha$  -  $\beta$  forged pancake.  
° Specimen Number

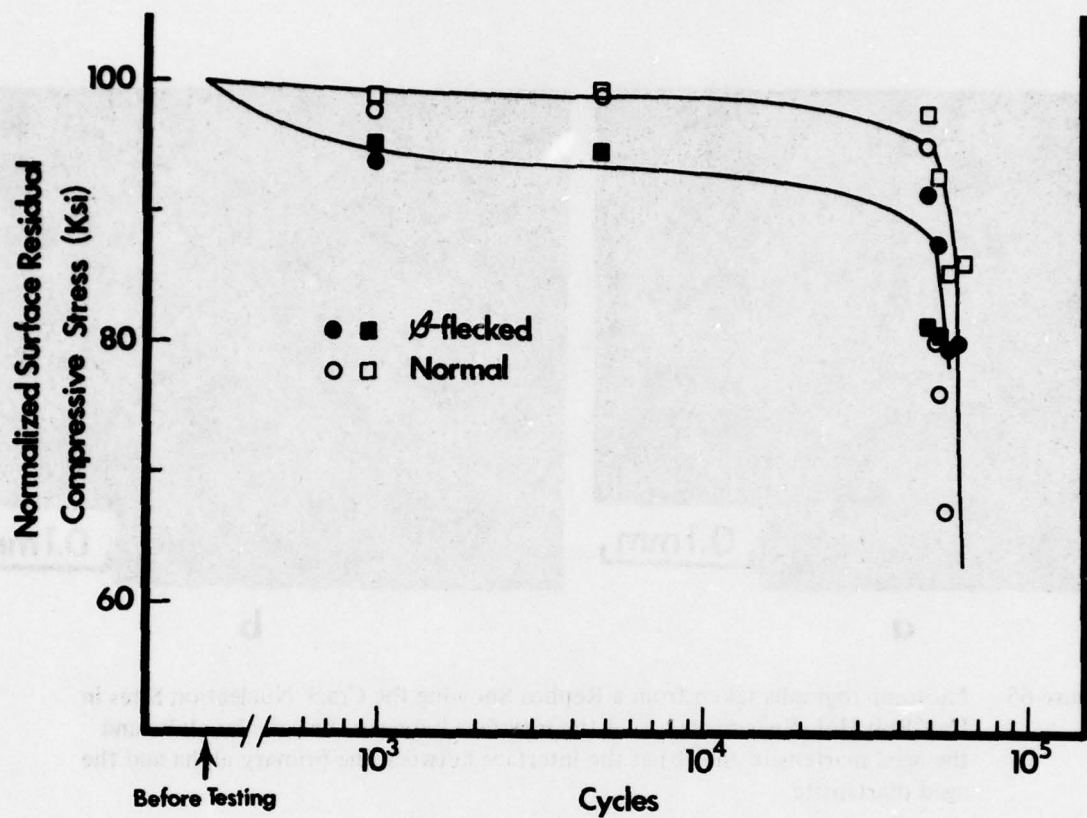


Figure 64 Cyclic Relaxation of Surface Residual Stress in Mini Krouse Specimens

#### (d) Crack Nucleation

The crack initiation sites were determined from replicas periodically taken on the gage surfaces of the half bolt hole specimens. In specimens water quenched from the solution treatment temperature (See footnote in Table 25), cracks nucleated at the interface between either the acicular (Figure 65a) or primary alpha (Figure 65b) and the aged martensite. In the case of the AC heat treatment, cracks again nucleated at the interfaces between either the primary alpha or the acicular alpha and the beta phase. In both cases, beta-fleck defects did not act as preferential crack nucleation sites. Cracks were observed to nucleate in the normal areas rather than in the adjacent beta-fleck defects as shown in Figure 66. In the case of beta heat treatment, cracks nucleated at slip bands normal to the longitudinal axis of the acicular alpha phase and also at the alpha:beta interface. With increasing amounts of cyclic deformation, cracks also nucleated at the prior beta boundaries (Figure 67). However, these are not preferential crack nucleation sites in any one of the three microstructures studied.

To summarize, the strain-controlled testing shows that beta-fleck defects result in fatigue debit only in the presence of surface residual stress without which the beta-flecked microstructure has crack nucleation resistance equal to or better than that of the normal microstructure. Further, beta-fleck defects are not preferential sites for crack nucleation. Phenomenologically, the relaxation of surface residual stress can be correlated with the fatigue debits in the beta-flecked microstructures.

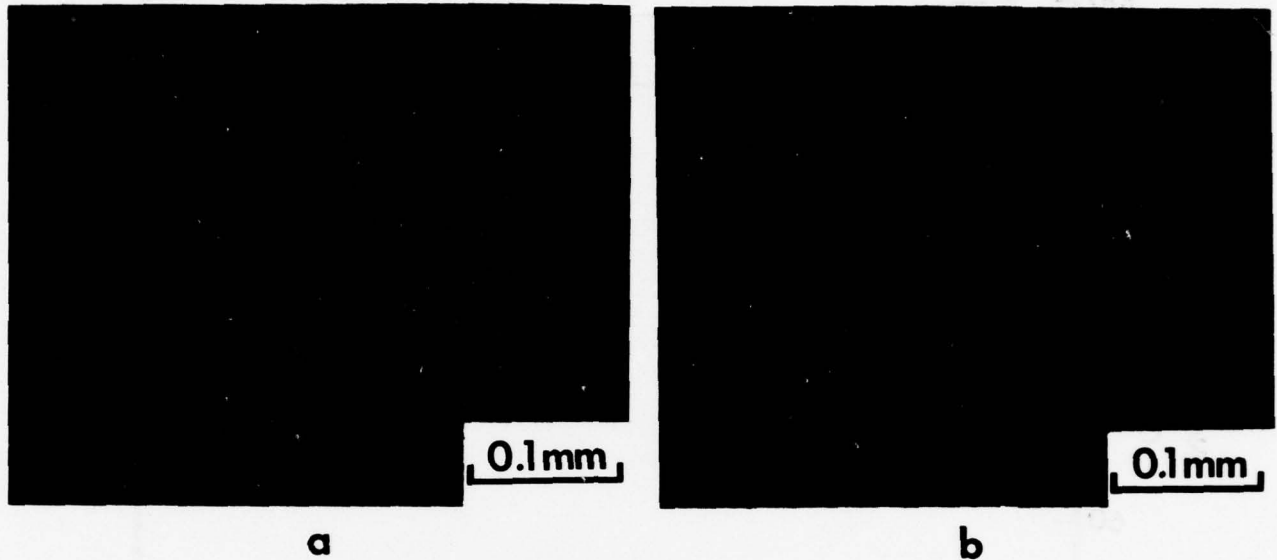


Figure 65 Photomicrographs taken from a Replica Showing the Crack Nucleation Sites in Half Bolt Hole Specimens, (a) at the interface between the acicular alpha and the aged martensite and (b) at the interface between the primary alpha and the aged martensite.

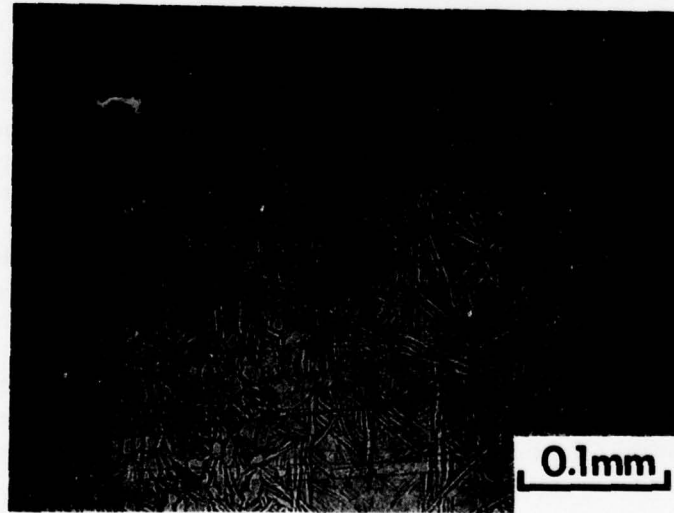


Figure 66 Photomicrographs taken from a Replica Showing a Crack Nucleated in a Normal Region Rather than at the Adjacent Beta-Fleck Defect.

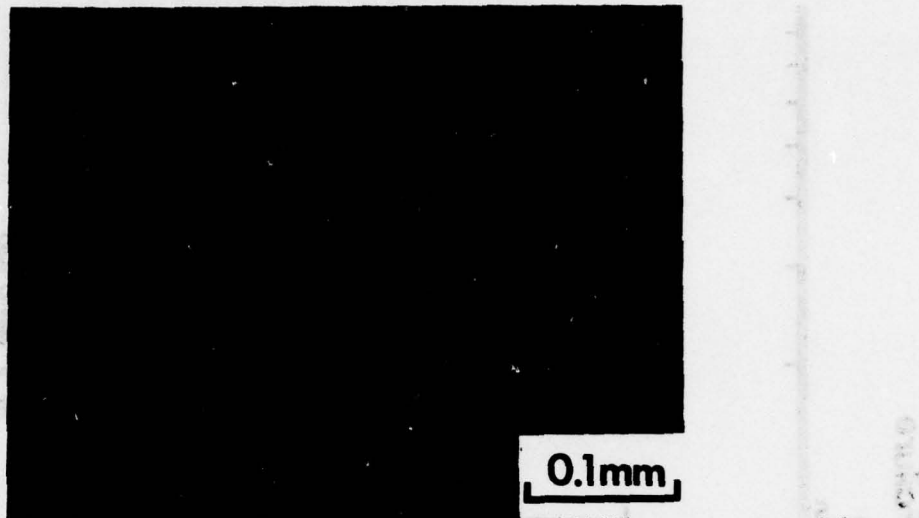


Figure 67 Photomicrograph Taken from a Replica Showing Crack Nucleation at Slip Bands Normal to the Acicular Alpha Phase, at a Prior Beta-Boundary and at Alpha-Beta Interfaces

Some of these observations are rather unexpected and therefore, questions arise whether similar observations can be made in stress-controlled LCF tests. These questions will be addressed by the LCF experiments and results presented below.

### (3) Stress-Controlled LCF Properties

The smooth LCF specimens shown in Figure 60e were tested to failure at room temperature using maximum stresses of 80 to 120 ksi and a stress ratio of either 0.1 or -0.6. A frequency of 30 Hz was used. The specimen surface preparation procedures were similar to those described previously. Results are as follows:

#### (a) Effect of Surface Preparation

Figure 68 shows the results from stress-controlled LCF tests at a maximum stress of 110 ksi as a function of the same three surface preparations described in Section III.2.b(2). The large circles in Figure 68 represent the average lives while the results of individual tests are given by small circles. Scatter in residual stress values and LCF lives is evident for the as-machined condition. However, the same trend as in the strain-controlled tests is observed.

Again, fatigue debits in the beta-flecked material occur only in conjunction with the presence of compressive surface residual stress. In the stress-relieved surface condition the beta-flecked microstructure has better LCF capability than the normal microstructure. This observation will be illustrated more clearly in the next section.

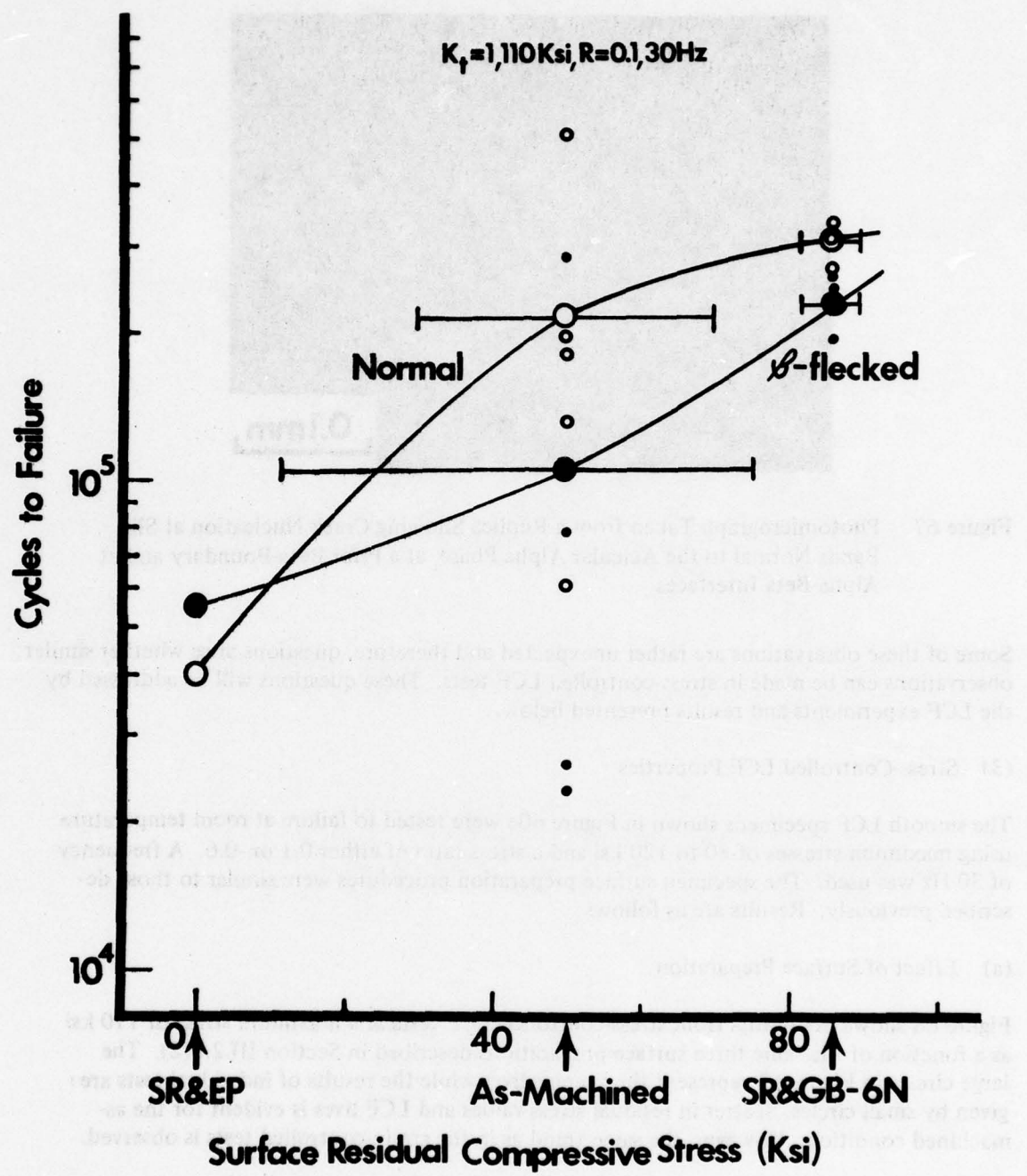


**Figure 68** Effect of Surface Preparation on Fracture Life of Normal and Beta-Flecked Specimens in Stress-Controlled LCF Tests

(b) Effect of Stress Amplitude

The S-N curves of the beta-flecked and normal materials tested in a stress-relieved and electro-polished condition are illustrated in Figure 69. The symbols used in this Figure have the same meanings as those in Figure 68. At all the three stress levels tested, the beta-flecked specimens had longer lives than the normal specimens, this difference is larger at lower stress levels. The latter observation is in good agreement with that in the strain-controlled tests (See Table 27).

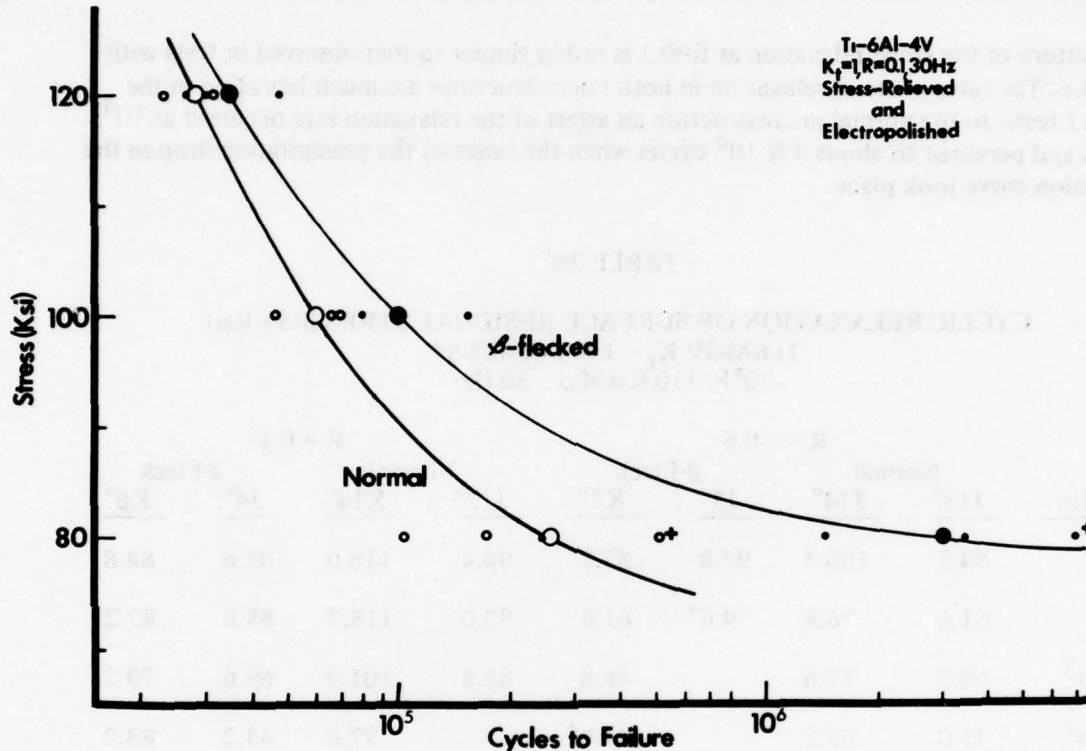


Figure 69 S-N Curves for Normal and Beta-Flecked Specimens With Stress-Relieved Surfaces

(c) Cyclic Relaxation of Surface Residual Stress

For this series of tests, specimens with stress-relieved and glass-bead peened (6N) surface were tested with a stress ratio ( $R$ ) of either -0.6 or 0.1, all at a maximum stress of 110 ksi and a frequency of 30 Hz. The variations of residual stress with number of cycles are given in Table 30 and illustrated in Figures 70 and 71 for the stress ratios of -0.6 and 0.1, respectively. All stresses have been normalized to an initial value of 100 ksi. It is obvious from these results that the beta-flecked microstructure relaxed the surface residual stress at more rapid rates than the normal microstructure in either test conditions. An exception to this behavior pattern is observed from a beta-flecked specimen (#K6, data not plotted in Figure 71) which apparently relaxed the residual stress at an equivalent rate as that from specimens with normal microstructure. Note, however that the life of this specimen was lower than that observed in the specimens with normal structure. The reason for this exception is not clear; it is possible that the residual stress measurements were made in this case on a region with normal microstructure.

At R=-0.6, both the normal and the beta-flecked microstructures relaxed the stresses rapidly upon cycling. Important differences occurrences occurred after about 1000 cycles when the relaxation rates in the normal microstructure were arrested, no significant relaxation took place thereafter until about  $10^4$  cycles, after which the relaxation rates increased rapidly. In contrast, there was no discernible arrest of the relaxation rate in the beta-flecked microstructure, the surface residual stress decreasing at a rapid rate throughout the test.

The pattern of the stress relaxation at R=0.1 is rather similar to that observed in tests with R = -0.6. The rates of stress relaxation in both microstructures are much less rapid in the R = 0.1 tests. In the normal microstructure an arrest of the relaxation rate occurred at  $10^4$  cycles and persisted to about  $3 \times 10^4$  cycles when the onset of the precipitation drop in the relaxation curve took place.

TABLE 30

CYCLIC RELAXATION OF SURFACE RESIDUAL STRESSES (-Ksi)

Ti-6Al-4V K<sub>t</sub> = 1 SPECIMENS\*

70°F, 110 ksi Max., 30 Hz

Cycles	R = -0.6				R = 0.1			
	Normal J13°	Normal J14°	β-Fleck J3°	β-Fleck K7°	Normal J12°	Normal K14°	J4°	β-Fleck K6°
0	84.8	106.4	92.8	87.2	94.4	116.0	85.6	84.8
10 <sup>3</sup>	61.6	76.8	9.6 <sup>+</sup>	61.6	92.0	118.2	85.6	87.2
5 x 10 <sup>3</sup>	59.2	77.6		48.8	84.8	101.4	69.6	79.2
1 x 10 <sup>4</sup>	45.0	65.2		44.0 <sup>+</sup>	—	97.6	43.2	83.2
1.4 x 10 <sup>4</sup>	38.4 <sup>+</sup>	52.8			—	98.5	38.4	—
1.7 x 10 <sup>4</sup>		38.4 <sup>+</sup>			—	—	—	—
3.2 x 10 <sup>4</sup>					—	—	35.2 <sup>+</sup>	—
3.4 x 10 <sup>4</sup>					66.4	—		83.2 <sup>+</sup>
4.6 x 10 <sup>4</sup>					—	93.6		
4.9 x 10 <sup>4</sup>					—	59.2 <sup>+</sup>		
5.4 x 10 <sup>4</sup>					53.6 <sup>+</sup>	—		

\* Machined from the billet.

° Specimen Number

— No Determination

+ Last determination before failure

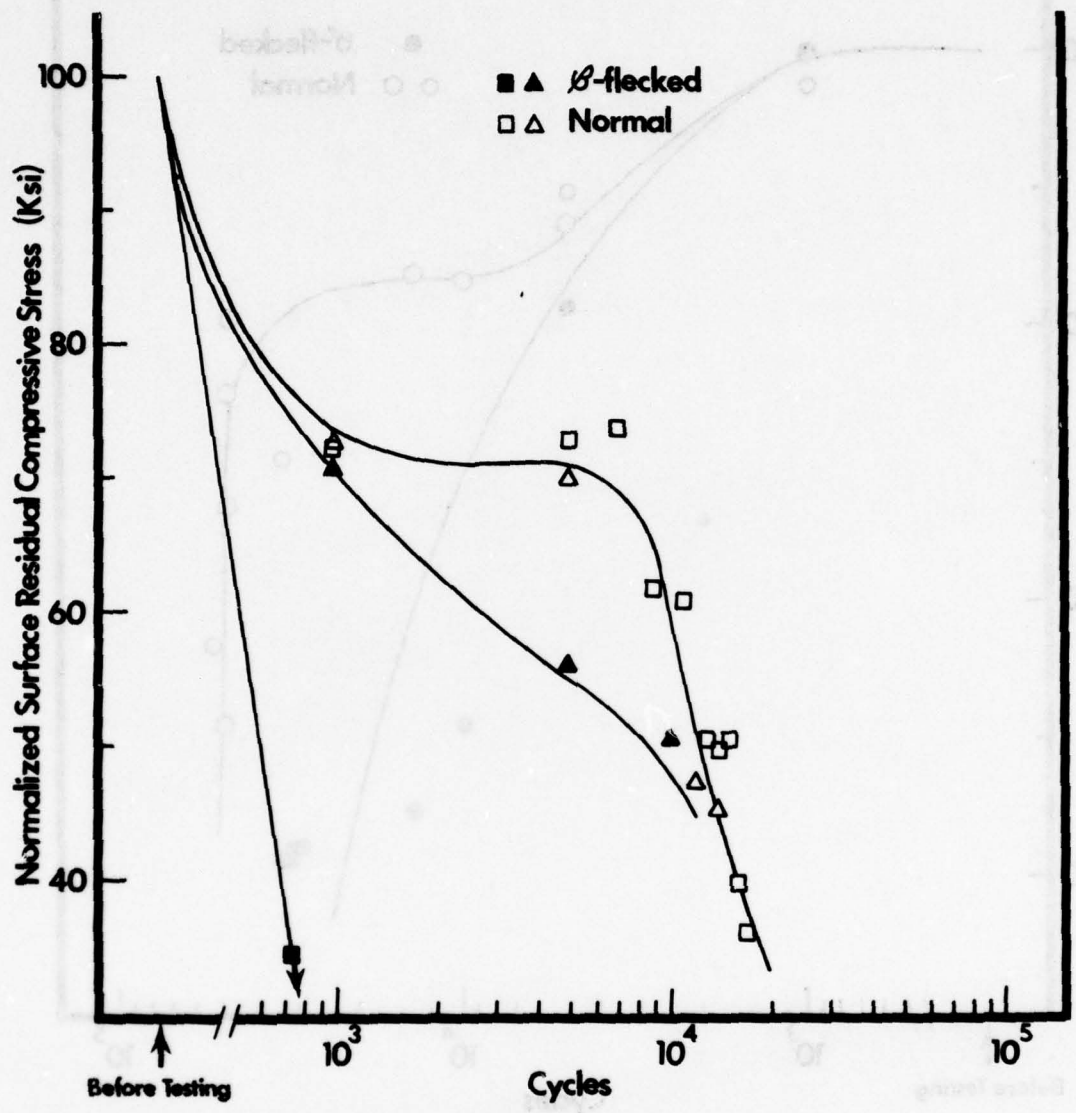


Figure 70 Cyclic Relaxation of Surface Residual Stress in Normal and Beta Flecked Specimens at  $R = -0.6$ .

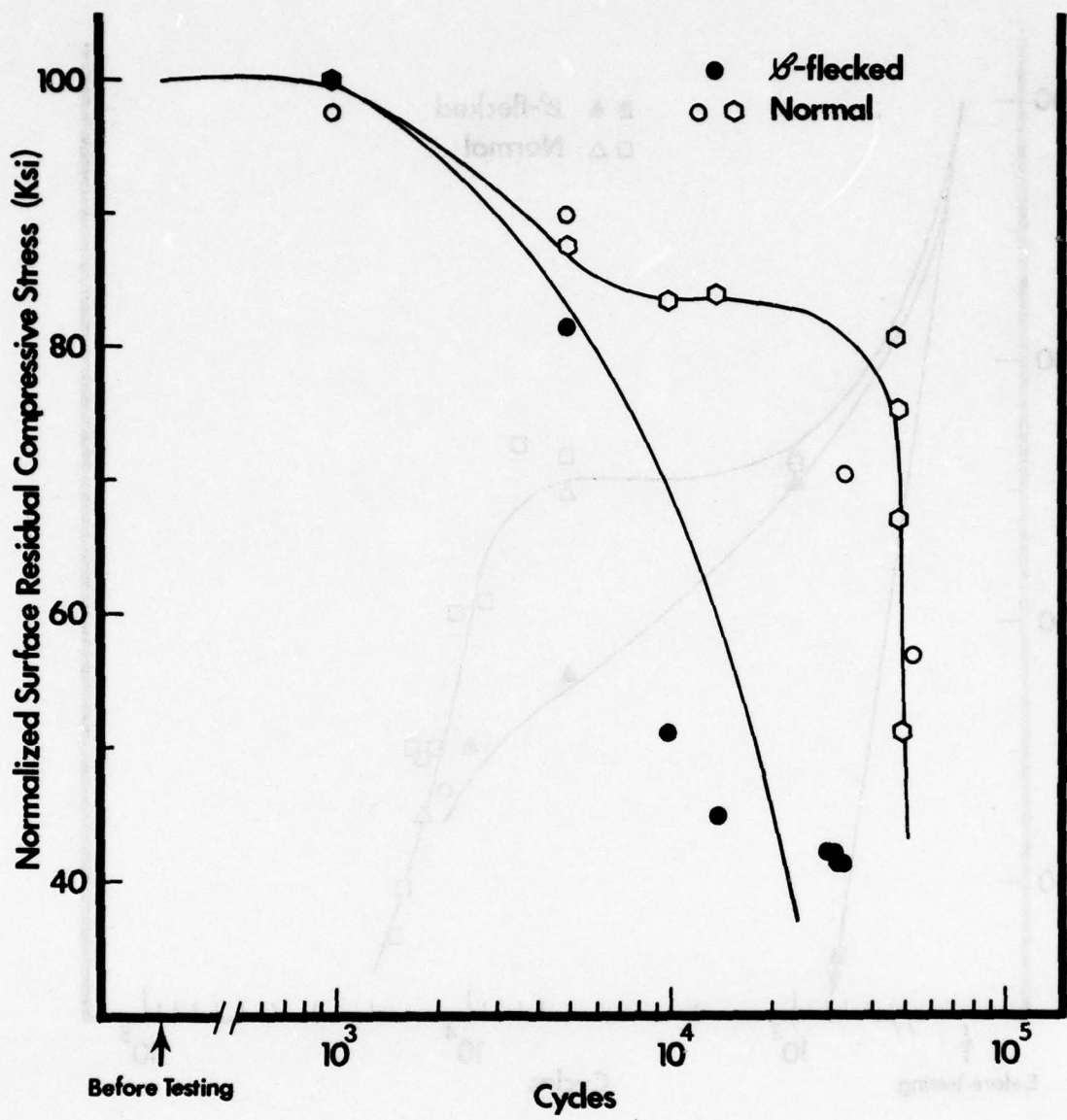
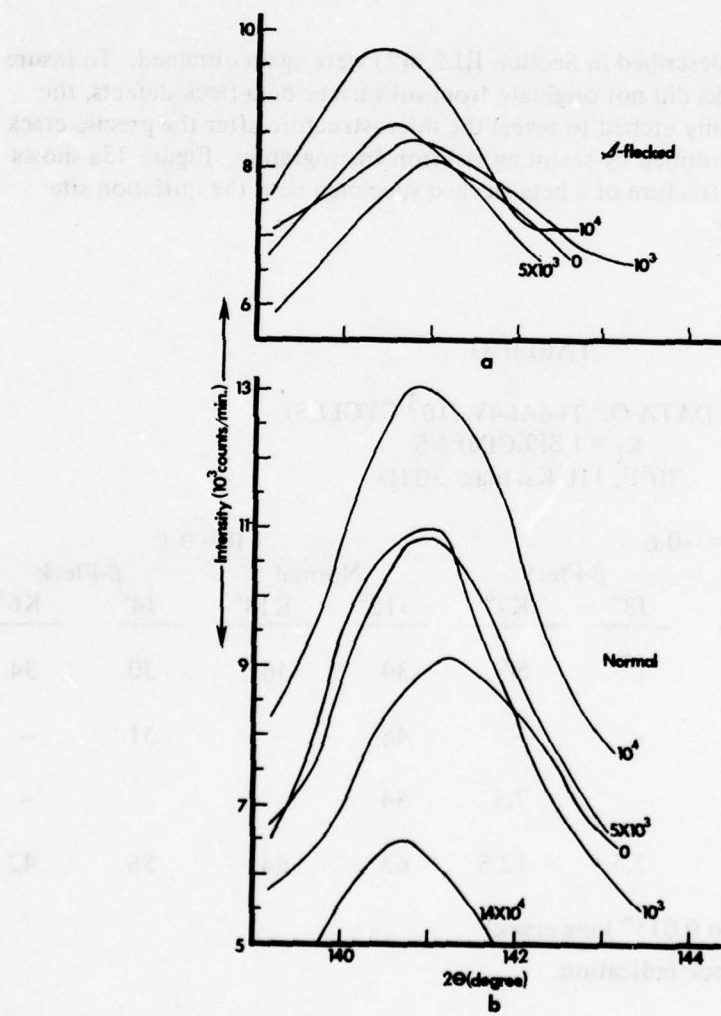


Figure 71 Cyclic Relaxation of Surface Residual Stress in Normal and Beta Flecked Specimens at  $R = 0.1$ .

Other differences between the beta-flecked microstructure and the normal microstructure are evident from the X-ray diffraction peak profiles which are reproduced in Figure 72 for the R=-0.6 tests. As shown in the Figure, the initial diffraction peak from a beta-flecked specimen is broader and lower in intensity than that from a normal specimen. Although the diffraction peaks sharpen and increase in intensity with increasing number of cycles in both microstructures, the changes in the beta-flecked microstructure occur much more slowly than those obtained from the normal microstructure. The rate of change in the diffraction peak profiles can be correlated with those of the residual surface stress. For example, Figure 70 shows that the change in residual surface stress between  $10^3$  cycles and  $5 \times 10^3$  cycles in the normal microstructure is small, correspondingly small changes in the diffraction peak profiles and intensity can be observed in Figure 72b. The implications of these observations on mechanisms of cyclic relaxation will be discussed later.



**Figure 72** X-Ray Diffraction Peak Profiles of (a) Beta-Flecked Specimen (b) Normal Specimen After Various Numbers of Stress Cycles at R = -0.6.

The results of the surface crack inspection during the tests are given in Table 31. At R=-0.6, 'pinpoint' cracks were observed in both microstructures much sooner than in the R=0.1 tests. In the specimens with normal microstructure (Specimens J13 and J14) the number of cycles to 'pinpoint' cracks are  $1.1 \times 10^4$  and  $1.3 \times 10^4$  which correspond closely with the onset of the final stage of surface stress relaxation (Figure 70). A fatigue debit of about one order of magnitude is observed in the beta-flecked microstructure under these test conditions.

At R=0.1, 'pinpoint' cracks were observed in the specimens with normal microstructure after  $3.4 \times 10^5$  and  $4.6 \times 10^5$  cycles which again are located near the onset of the precipitous drop in the relaxation curve. The beta-flecked specimens developed 'pinpoint' cracks after  $3.0 \times 10^5$  and  $3.4 \times 10^5$  cycles which led to fracture at  $5.6 \times 10^5$  and  $4.2 \times 10^5$  cycles. Thus the fatigue debit of the beta-fleck defects is rather small in the R=0.1 tests.

#### (d) Crack Nucleation

Observations similar to those described in Section III.2.b(2) were again obtained. To insure that the apparent surface cracks did not originate from subsurface beta-fleck defects, the fracture surfaces were chemically etched to reveal the microstructure after the precise crack nucleation sites had been determined by scanning electron fractography. Figure 73a shows the general appearance of the fracture of a beta-flecked specimen near the initiation site which is indicated by an arrow.

TABLE 31

LCF DATA OF Ti-6Al-4V ( $10^3$  CYCLES)  
 $K_t = 1$  SPECIMENS  
 70°F, 110 ksi max. 30 Hz

Cycles To	R = -0.6				R = 0.1			
	Normal J13°	Normal J14°	β-Fleck J3°	β-Fleck K7°	Normal J12°	Normal K14°	β-Fleck J4°	β-Fleck K6°
PP*	11	13	1+	5+	34	46	30	34
1/64"	12	15	-	-	48	-	31	-
1/32"	13	-	-	7.5	54	-	-	-
Failure	16	20	2.5	12.5	63	64	56	42

\* 'Pin-point' crack (0.005" to 0.015" long crack)

+ Last inspection with no crack indication.

° Specimen Number

- No determination

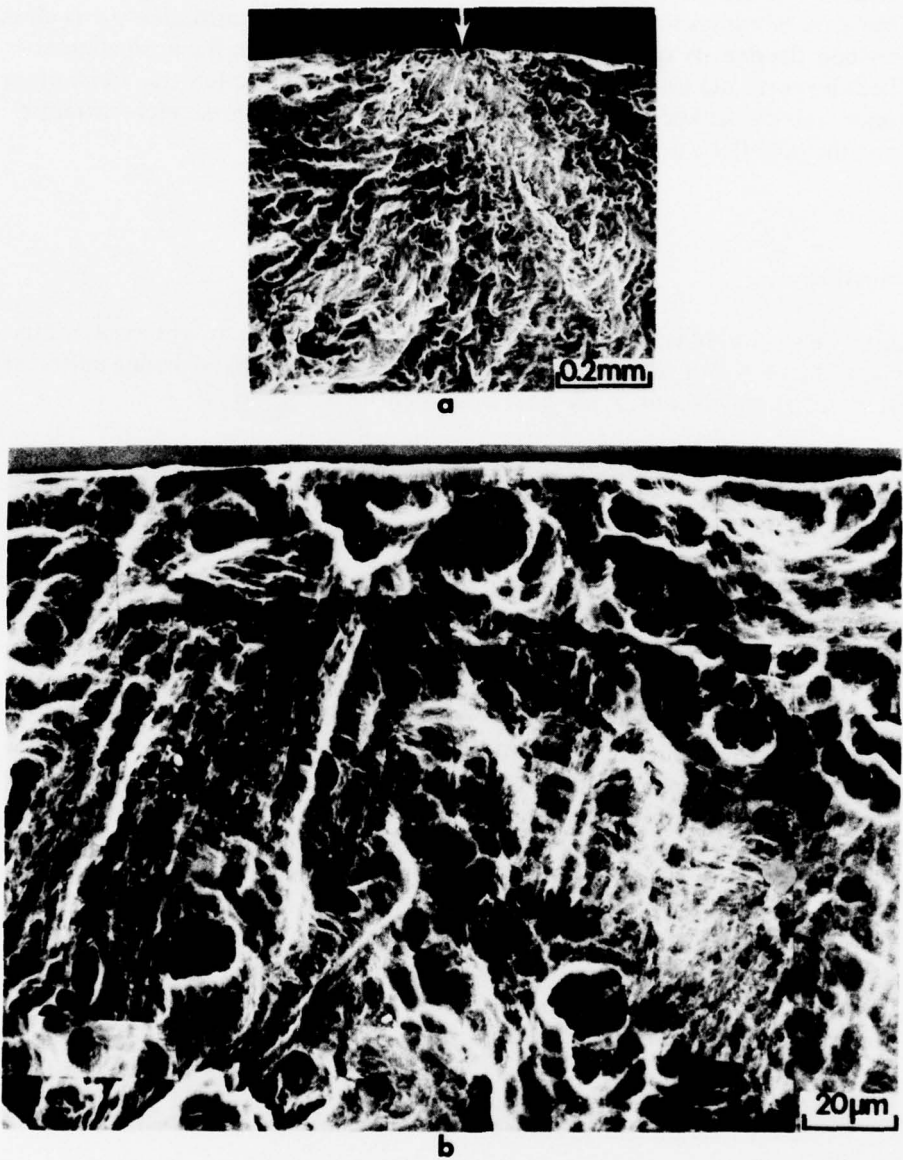


**Figure 73** Crack Nucleation Site in a Beta-Flecked Specimen  
(a) General Appearances of the Fracture Surface, Arrow Indicates the Crack Origin.  
(b) Microstructure at the Fracture Origin.

The microstructure at the crack initiation site on the fracture surface is illustrated in Figure 73b. The presence of equiaxed primary alpha particles at the crack initiation site is clearly evident. Further, the density of those particles is the same as that in the normal microstructure, i.e., the crack did not nucleate preferentially at beta-fleck defects. In all other cases examined, the cracks were also observed to nucleate at the normal microstructure rather than at the beta-fleck defects.

### 3. Discussion

#### A. Introduction

In this section we shall summarize the rather complex behavior pattern observed in this investigation and then attempt to account for this pattern. In the fatigue testing performed three major variables which control life have been identified as follows:

- 1) Microstructure
- 2) Residual Stress
- 3) Test Conditions

A complete experimental test matrix covering all possible combinations of these variables has not been performed, so in order to fill in certain parts of the matrix we will draw on results of other investigations. Care has to be exercised in making such comparisons, for all details of the material used in a study, the surface condition of specimens and the test parameters, must be known in detail. To give one example, it has been reported that texture has a major effect on the influence of beta-flecks,<sup>(26)</sup> this is not a major variable in the present study but could be of great importance in measuring and comparing the cyclic behavior of plate material. Another useful comparative exercise could be to view the beta-fleck condition as a hybrid of equiaxed alpha:beta structure and beta processed structure. Then by using observations on both base conditions it should be possible to bound the fatigue capability of flecked material and perhaps obtain insight into reasons for the behavior pattern. Although we shall use this approach in several cases it should be remembered that we have shown that cracks do not nucleate preferentially in the acicular structural regions of a flecked structure. As the transformed beta structures are usually considered the 'weak link' the comparison cannot be completely valid.

In the following sections we shall discuss the several aspects of fatigue behavior, attempting to clearly separate the phenomenology (fact) from the mechanistics (speculation).

#### Microstructure

The compositional fluctuations responsible for the presence of flecks has been clearly established in this study. Re-forging of the flecked material indicates that flecks do not arise from processing factors such as adiabatic heating and shows that the compositional heterogeneities are persistent. The only factor that cannot be explained quantitatively at the present time is the magnitude of the depression of the beta transus. If we compute the expected depression using the measured compositional differences of aluminum, vanadium and iron coupled with the effect of these elements on the transus in binary systems a value of -25°F is obtained. The observed difference is of the order of 50°F. It is possible that in this multicomponent system the above calculation is an over simplification.

The microstructural differences between the forging and billet material can be related to the processing histories. It appears that in the billet material insufficient reduction was accomplished in the last stages of processing to produce complete recrystallization. Thus the prior beta grain size can be clearly delineated and a generally coarse macrostructure is present. The forging received sufficient alpha:beta work to produce complete recrystallization and little or no trace of prior beta grain could be observed.

### Crack Nucleation

The predominant mode of crack nucleation in both 'normal' and beta-flecked material was separation along alpha:beta interfaces. Several other modes of cracking have been reported for Ti-6Al-4V<sup>(27)</sup> such as separation along shear bands in acicular regions and transgranular fracture of coarse alpha plates. The latter failure locations are favored in high stress (or strain range) tests and in specific microstructures and therefore the present observations, at least in normal equiaxed microstructures, are not unexpected. Nucleation in the beta-flecked microstructure could have been anticipated to occur preferentially in the acicular structure regions. In the stress-relieved specimens, as no difference in fatigue capability was observed, perhaps no difference in location should have been expected. For as-machined surfaces preferential nucleation would have provided a straightforward explanation of the observed fatigue debit in flecked material. As observation of as-machined surfaces are difficult several specimen fracture surfaces were etched lightly to examine the nucleation site in more detail, in all cases it was found that nucleation occurred in normal or equiaxed structural regions. Two factors could contribute to this observation. Firstly, it has been shown that the composition of the flecked region differs from the general composition of the material. The fatigue capability of these regions could conceivably be superior to acicular Ti-6Al-4V. Secondly the LCF properties of acicular structures are often stated to be inferior to equiaxed alpha:beta material. This is too broad a generalization. The properties of coarse colony type structures are in general inferior, however, water quenching from the beta phase field to form a martensitic structure (and subsequent tempering) can give a material with superior fatigue properties<sup>(20)</sup>. Widmanstatten alpha:beta plate structures lie between these extremes and Figure 66 shows that this is the usual structure present in flecks in the forging. One or both of these factors could explain why fatigue cracks do not nucleate in the beta-flecked regions.

### Fatigue Results

The same general pattern holds for results for both the smooth ( $K_t = 1$ ) specimens tested under stress-controlled and the notched ( $K_t = 2$ ) strain-controlled tests. When comparing the results of both types of tests, under conditions which give roughly equivalent life, the relative magnitude of the various effects can be different. The major points are summarized in the following section.

#### 1) Stress-Relieved Specimens

Material with the normal and beta-flecked microstructures exhibit the same cyclic capability if the surface of the material is stress-free and tests are conducted at high stress or strain levels. In the half bolt hole tests, differences in the crack nucleation life between the billet and forged materials were observed which could be attributed to the coarser macrostructure in the former

material. The fatigue properties of both materials can be further reduced by beta heat treatment to produce a colony-type acicular microstructure; again no difference between originally flecked and normal microstructure is observed. Further, this heat treatment also eliminated the LCF difference between the two product forms since microstructural differences arising from variation in processing are removed by this heat treatment.

Under lower stress or strain conditions the beta-flecked material exhibits superior fatigue properties with respect to normal material. This is a surprising result but, as we shall see later, a similar result has been obtained in a comparative testing on beta and alpha:beta microstructures. The half bolt hole tests also demonstrate that water quenching from the solution treatment temperature results in improved properties compared with material air cooled from the same temperature. This observation applies to both product forms.

## 2) As-Machined Specimens

In both stress-or strain-controlled tests, the beta-flecked material has lower life than normal material by about a factor or two. Machined surfaces introduce two new variables into the experimental test matrix; surface roughness and residual stress. The surface roughness was not explicitly characterized in the present study but the depth of surface marks was on the order of 10 micro inches. Residual stress measurements indicated that large variations were presently, especially on flecked specimens. A similar variation in fatigue life was also observed. The half bolt hole tests also first indicated differences in residual stress pattern after testing. These results, Figure 63, show that the stresses decline to lower values in flecked material than found in specimens with a normal microstructure. At first it was assumed that the coarser beta-flecked microstructure may be unable to retain as high a level of initial residual stress as normal material. Several measurements failed to confirm this, although companion experiments on beta treated specimens did reveal lower values. (There are problems with interpreting these latter results in that a calibrated standard was not used).

Results from an earlier investigation<sup>(25)</sup> on beta processed material are included in Figure 62 which show that the improvement of fatigue properties produced by machining are lower than that in normal material. The results from the flecked-microstructure lie between these two extremes.

Because of the large scatter in both residual stress and fatigue results most of the additional study was performed on electropolished and peened samples. An interim treatment that was attempted, was to peen over a machined surface. The four tests performed indicated that although scatter could have been reduced average properties remained constant.

## 3) Stress-Relieved and Peened Specimens

Using this specimen surface preparation technique both the scatter in the residual stress and fatigue results were reduced. In either test type the superiority of the normal microstructure with respect to flecked material is maintained. The one surprising result is that the fatigue capability of the billet material is slightly greater than the forged material.

It can be noted that by using these surface conditions the nucleation life in half bolt hole specimens had been increased by a factor of fifty over the stress-relieved baseline while the

maximum structural effect is about a factor of two. A similar trend can be noted in the stress-controlled test although the surface effects factor is about seven and that of the structure remains at about two. The life debit in beta-flecked specimens can be changed by increasing the cyclic stress amplitude which is the same as changing the R value. Under an R of -0.6 the debit associated with beta flecks is nearly an order of magnitude.

The final group of Krouse specimen tests were performed for the following reasons. By selecting fully reversed bending (R=1.0) and a high strain range it was assumed that the debit associated with beta-flecks would be maximized. The larger surface area of this specimen would allow more accurate residual stress measurements and also post-test analysis of the deformation structure by transmission electron microscopy. As noted in the results section this specimen did not contain beta-flecks and thus these expectations were not realized. The limited TEM work performed on these specimens failed to provide any additional insight into the specific relaxation mechanisms.

The detailed residual stress measurements performed on the stress-controlled test specimens have been described in Section III.2.b(3). These will be discussed in more detail below. Before that however, we will compare the overall behavior pattern observed in this study with the results of previous investigations.

#### Comparison With Other Studies

Beck<sup>(28)</sup> examined the behavior of Ti-6Al-4V forgings processed to give an equiaxed alpha:beta and beta (colony) structure. Among the large number of variables studied were residual stress and R value. Figure 74 taken from Beck's report summarizes, as S-N curves, the effect of surface condition and microstructure. In the chemically milled condition in the low-life region the equiaxed microstructure is slightly superior to the acicular microstructure, this effect reverses in the high-life region. The effect of compressive residual stress, especially peening, are much more pronounced in the equiaxed structure at intermediate lives than in the beta microstructure. If, as stated in the introduction, beta-fleck could be considered an intermediate condition between these two limits then the parallels between these results and the present investigation are quite striking. A further result of Beck's study was the observation that for machined specimens the differences between the two structures were accentuated at negative R values. At positive R values differences between the two structures were slight but an R value of -1.0 produced a large debit for the beta processed structure.

The results of the present investigation only parallel in part the results obtained on Ti-6Al-6V-2Sn containing beta flecks<sup>(20)</sup>. All specimens in the latter study were tested in the as-machined condition and tests were conducted at an R value of 0 or 0.1. Comparable half bolt hole tests gave somewhat larger debits than in the present study. Smooth bar axial testing also indicated lower capability for the flecked specimens over the life range  $10^4$  to  $10^7$  cycles. In cases where cracking was examined it was observed to occur preferentially in the beta-flecked regions. One may conclude that the magnitude of the debits associated with beta-flecks depend on the specific alloy.

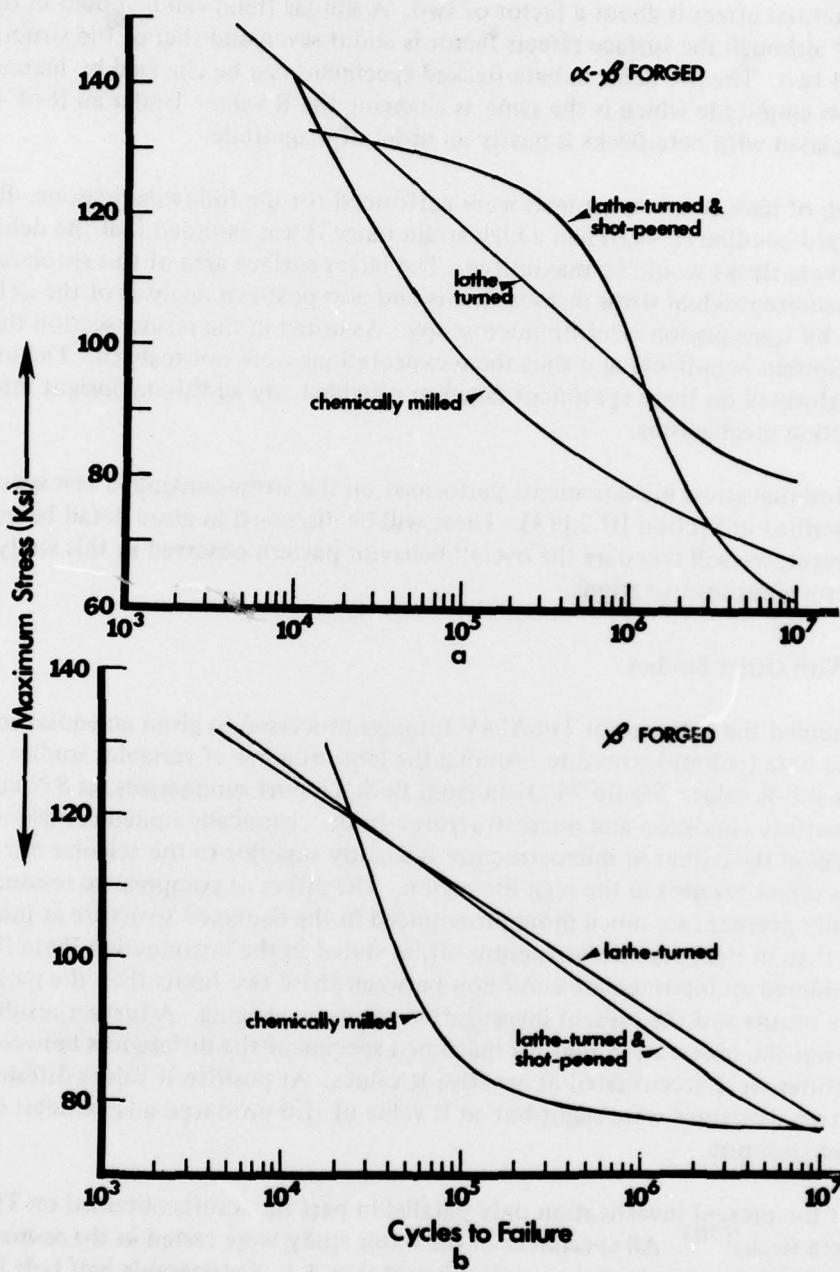


Figure 74 S-N Curves of (a) Alpha-Beta Finish Forged, (b) Beta Finish Forged Ti-6Al-4V With Various Surface Finishes (Ref. 28).

### Surface Residual Stress Relaxation

The importance of surface conditions on the fatigue properties of titanium alloys has long been recognized, but controversy exists over the magnitude and extent of these effects. For example Metcut<sup>(29)</sup> has investigated the influence of a variety of finishing operations on fatigue properties of Ti-6Al-4V in a beta processed condition and concluded that in the  $10^7$  cycle life range no correlation with surface roughness or residual stress could be obtained. Fatigue life could be correlated with the subsurface peak residual stress. In the present study we have observed that the fatigue capability of either the beta-flecked or the normal Ti-6Al-4V increases with increasing surface residual stress. It is possible that for the types of surfaces that we have studied (as-machined, stress-relieved and peened) the magnitudes of the peak residual stress are directly proportional to the surface residual stress. Our observation is therefore not necessarily different from those of Metcut.

Further, the present work has demonstrated, in a self-consistent manner, a good correlation of cyclic relaxation behavior with the LCF crack nucleation as follows:

- 1) For a given maximum stress, the test condition which relaxed the surface residual stress at a faster rate also resulted in shorter crack nucleation life.
- 2) For a given test condition, the beta-flecked microstructure which relaxed the surface residual stress at a faster rate compared with the normal microstructure resulted in a fatigue debit.
- 3) Cracks nucleated at the onset of the precipitous stress relaxation.

Residual stress:depth profiles, and changes thereof on cyclic loading, have not been measured in the present investigation. Earlier studies at P&WA on equiaxed alpha:beta Ti-6Al-4V have shown that using a GB12N shot peening treatment a maximum stress occurs at a distance of 0.0015" below the surface about 10 ksi higher than the surface stress. The compressive stress falls to zero at a depth of 0.008". It could be noted that in normal alpha:beta material the compressive stress field extends over several secondary beta grains. As the structural size increases, assuming the profile remains constant, the number of grains encompassed decreases. It is possible that the mean free slip path or slip length may contribute to the stability of the residual stress and thus contribute to the behavior pattern observed in this investigation.

Mechanistically, cyclic relaxation of the surface residual stress results from irreversible motion of mobile dislocations, and possibly twinning, which are either present in the deformed surface layer and/or generated during the cycling. The amount of relaxation would therefore be determined by dislocation parameters such as the mobile dislocation density, the stability of the dislocation substructure and the dislocation obstacle spacing.

The test condition is also important as the magnitude of the imposed stress or strain during LCF testing determine not only the excursion distance of the mobile dislocations but also whether dislocations are generated. While increasing the excursion distance generally leads to more cyclic relaxation, since bypassing of obstacle becomes more probable, generation of new dislocations may or may not lead to cyclic relaxation depending on their mobility in subsequent cycles. Thus if the generated dislocations are rendered immobile by mechanisms

such as solute pinning, dislocation reactions, formation of a stable dislocation group, cyclic hardening rather than softening will occur. In fact, it has been reported that in reversed bending of annealed steels, a residual compressive stress is produced near the surface of a specimen<sup>(30)</sup>. Further the higher the carbon content the larger the residual stress produced. Thus it is difficult to predict the effects of test conditions on cyclic relaxation behavior from a basic point of view. This type of effect may be responsible for the much slower relaxation rates observed in the Krouse specimens tested in bending at an R of -1.0 compared with Sonntag specimens tested in tension at an R of -0.6.

X-ray diffraction peak profiles should provide some information regarding the mechanisms since important differences have been observed, see Figure 72 between the normal and the beta-flecked microstructures. The initial diffraction peak in the beta-flecked microstructure are broader and lower in intensity than that in the normal microstructure. Although in both microstructures the diffraction peaks sharpen and increase in intensity with number of cycles, those in the beta-flecked microstructure change much more slowly than that in the normal microstructure. According to the X-ray diffraction theories the width and intensity of the diffraction peaks are related to the microstrain, crystallite size and stacking faults<sup>(31)</sup>. A crystallite is a region within a crystal or grain which diffracts X-ray coherently. This region is one of a given orientation bounded by a low angle grain boundary, dislocations, a twin boundary etc. <sup>(31)</sup>. The microstrain, arising from dislocations within the crystallite, causes broadening of diffraction peaks. Peak broadening is also caused by small crystallite size which also reduces the diffraction intensity. Thus the broader and lower intensity of the initial diffraction peak in the beta-flecked microstructure suggest that the dislocation substructure sizes are smaller and that the microstrain within the substructures are higher than those in the normal structure. These features change slowly with cycling, as evidenced by the correspondingly small changes in the diffraction peak profiles. Therefore the cyclic relaxation of the surface residual stress in the beta-flecked microstructure may have involved the generation of more mobile dislocations than in the normal microstructure. The cyclic relaxation in the latter involves more dislocation movement and rearrangement which results in larger dislocation substructural size and less microstrain, as suggested by the more rapid sharpening and increase in intensity of the diffraction peaks. These inferred relaxation mechanisms if real, must be related to the microstructures. It is therefore interesting to compare the bulk cyclic relaxation in a beta heat treated microstructure with that in an equiaxed alpha-beta microstructure. Recent work by Wojcik and Koss<sup>(32)</sup> indicates that, in fact, the beta annealed structure does relax faster than the equiaxed microstructure. Further, the work of Wells and Sullivan<sup>(27)</sup>, Steele and McEvily<sup>(33)</sup> suggest that the difference in relaxation rates between these two microstructure increases rapidly as the imposed stress or strain range increases. Is the correlation of the bulk relaxation behavior with the surface relaxation behavior coincidental? This question has been critically examined by Finney et al.<sup>(34)</sup>, using the existing information and data from a carefully conducted series of experiments. They came to the conclusion that deformation near the surface is very similar to that in the interior.

In summary, if we view the beta-flecked structure as intermediate between equiaxed and acicular alpha-beta condition, the more rapid relaxation of surface residual stress can be accounted for. The exact details of how surface stress is stored and subsequently changed under cycling has been speculated upon but further work is required to elucidate specific mechanisms. Further, how the relaxation translates into the nucleation of a crack or cracks is now known. The results suggest that such processes could be usefully studied in stress relieved specimens as the residual stresses decline precipitously during crack nucleation.

#### 4. CONCLUSIONS

The following conclusions may be drawn from this investigation:

- 1) Beta-flecks are produced by local and persistent concentration of the elements V, Fe and inverse segregation of Al.
- 2) Comparative fatigue debits associated with beta-flecks are only observed in specimens with compressive residual surface stress. Specimens from beta-flecked material with stress-free surfaces show equivalent or superior fatigue lives when compared with normal equiaxed alpha:beta microstructure.
- 3) In either surface conditions cracks do not nucleate preferentially at beta-flecks. Thus a flecked condition is only a symptom rather than the cause for changes in fatigue properties.
- 4) The fatigue debits in machined or peened surfaces are accentuated by increasing the cyclic stress amplitude thus reducing the R value. It is possible that by combining these test conditions with poor surface preparation, debits of over an order of magnitude could be produced.
- 5) The rate of cyclic relaxation of surface residual stress depends on test condition. For a given LCF test, the beta-flecked microstructure relaxes the surface residual stress at a faster rate than the normal microstructure and results in a shorter crack nucleation life.
- 6) In the normal microstructure crack initiation occurs at the onset of the precipitous decline in surface residual stress.

## APPENDIX

### SURFACE RESIDUAL STRESS DETERMINATION

The residual stress was measured by the two-exposure X-ray diffraction method<sup>(35)</sup> using Cu K<sub>α</sub> radiation usually at a setting of 40 KV, 20mA. The angular positions  $2\theta$  of the diffracted beams from (2133) planes were measured at  $\psi$  angles ( $\psi = 0$  and  $= \pi/4$ ) using a diffractometer which scanned at a constant rate of  $2\theta = 0.1^\circ$  per minute. The angular  $2\theta$  shift in the lines upon angular  $\psi$  rotation of the sample with respect to the primary beam was determined by Ogilvie's parabolic fitting method in which five data points are obtained at equal  $2\theta$  intervals about the diffraction peak, and the parabolic curve is fitted by the method of least squares. The residual surface stress is then obtained as a product of the angular  $2\theta$  shift and the stress factor which for Ti-6Al-4V was determined experimentally to be 860 psi per  $2\theta = 0.01^\circ$ .

No correction due to Lorenz polarization and absorption was made since it had been observed that the resulting stress levels were within 1% of those obtained with these correction factors<sup>(36)</sup>. Beam penetration correction was not made since such correction required the shape of the stress gradient below the surface be known. Without this correction, the calculated stresses appear to be larger and the peak residual stress shifted toward the surface. However, meaningful comparison of results can still be made on a relative basis.

Residual stress was measured on stress-controlled LCF specimens and strain-controlled mini-Krouse specimens using a beam size of 0.016" wide and 0.2" long. The beam was oriented parallel to the longitudinal axis and to the width direction of the specimens respectively. Measurements were taken near the center of the gage section before testing and after a certain number of cycles, always at the same location in a given specimen.

In the case of the half bolt hole specimen, the measurement by two-exposure techniques could only be made after the specimen had fractured because of the obstruction of the beam by the specimen. A beam 0.125" wide, 0.5" long was used, the latter is parallel to the width of the specimen. The measurements were made as a function of distance from the fractured end which is usually located at the bottom of the bolt hole. Because of the strain gradient on the half bolt hole gage section the measurements, in effect, yielded information on relaxation of residual stress as a function of cyclic strain amplitude.

## REFERENCES

1. Rolls Royce presentation at the AFML Seminar on Defects in Titanium Alloys, Wright-Patterson Air Force Base, Ohio, 1973.
2. P&WA, Component Test, 1972.
3. D. F. Neal and P. A. Blankinsop, *Acta Met.*, 24, 59 (1976).
4. R. Steel and A. J. McEvily, Univ. Conn., Storrs, Conn., unpublished work, 1974.
5. E. Eylon and J. A. Hall, *Met. Trans.*, 8A, 981 (1977).
6. Yuen et. al., *Met Trans.* 5, 1833-1842 (1974).
7. M. J. Blackburn et. al. in "Stress Corrosion Cracking in Titanium Alloys," Advances in Corrosion Science ed. M. G. Fontana and R. W. Staehle, Vol. 3., Plenum Press, N.Y. 1973.
8. Metcut Report No. 1069-19640-2, February 1975, Cincinnati, Ohio.
9. F. Erdogan and G. C. Sih, *J. Bas. Engrg.*, 85 519 (1963).
10. D. F. Neal in "Forging and Properties of Aerospace Materials", Paper No. 10, University of Leeds Report, Jan. 1977.
11. F. W. Smith in "The Surface Crack: Physical Problems and Computational Solutions", ed. J. L. Swedlow, ASME 1972, p. 128.
12. G. R. Yoder, L. A. Cooley and T. W. Crooker, NRL Report 8048, Nov. 1976.
13. B. C. Odegard and A. W. Thompson, *Met. Trans.*, 5, 1207-1213 (1974).
14. R. M. Gilmore and N. A. Imam, to be published in *Met. Trans.*
15. D. N. Williams, *Met. Trans.*, 5, 2351-2358 (1974).
16. D. A. Meyn, *Met. Trans.*, 5, 2405-2414 (1974).
17. H. G. Nelson, A. S. Tetlman and D. P. Williams in "Corrosion Fatigue: Chemistry, Mechanics and Microstructure", National Association of Corrosion Engineers Vol. 2, 1971, p. 359.
18. Dell P. Williams and H. G. Nelson, *Met. Trans.*, 3, 2107-2113 (1972).
19. C. Hammond "Thin Foil Microscopy of Hydride - Titanium Alloys", Paper 38.1, TMS-AIME Fall Meeting, Niagara Falls, N.Y., Sept. 1976.

#### REFERENCES (Cont'd)

20. R. B. Sparks and J. R. Long, Report AFML-TR-301, 1974.
21. M. P. Smith, Pratt & Whitney Aircraft Report, February 1974.
22. Private Communication, Wyman-Gordon Co., 1974.
23. J. A. Hall, et. al., Mat. Sci. & Engr. 9, pp 197-210 (1972).
24. P. L. Reynolds, Evaluation of the Effects of Beta Flecks on LCF Life in PWA 1215, P&WA Report, April 1975.
25. S. Satta et. al., LCF of Ti-6Al-4V Forging, ASM Report D8-244, October 1968.
26. R. H. Jeal, Private Communication, 1976.
27. C. H. Wells and C. P. Sullivan, Trans. ASM, 62, 263-270 (1969).
28. E. Beck, Report AFML-TR-69-108, 1969.
29. W. P. Koster, N. Field and L. J. Fritz, Report AFML-TR-70-11, Matcut Research Associates, Inc., Cincinnati, Ohio (March, 1970).
30. S. Taira and Y. Murakani, Japan Soc. Mech. Engr. Bulletin, 4 (13), 41 (1961).
31. W. P. Evans and R. W. Buenacker, Trans AIME, 227, 447 (1965).
32. C. C. Wojcik and D. A. Koss, Materials Sci. Engr. 27, 97 (1977).
33. R. K. Steele and A. J. McEvily, Engr. Fract. Mech., 8, 31 (1976).
34. J. M. Finney, C. Laird and R. de la Vaux, Materials Sci. Engr. 24, 19 (1976).
35. Residual Stress Measurement by X-ray Diffraction - SAE J78A Second Edition, August 1971, Published by Society of Automotive Engineers, Inc., New York, N.Y.
36. B. Langer, PhD Thesis (1975) University of Connecticut, Storrs, Connecticut.

## REFERENCES

1. Rolls Royce presentation at the AFML Seminar on Defects in Titanium Alloys, Wright-Patterson Air Force Base, Ohio, 1973.
2. P&WA, Component Test, 1972.
3. D. F. Neal and P. A. Blankinsop, *Acta Met.*, 24, 59 (1976).
4. R. Steel and A. J. McEvily, Univ. Conn., Storrs, Conn., unpublished work, 1974.
5. E. Eylon and J. A. Hall, *Met. Trans.*, 8A, 981 (1977).
6. Yuen et. al., *Met Trans.* 5, 1833-1842 (1974).
7. M. J. Blackburn et. al. in "Stress Corrosion Cracking in Titanium Alloys," Advances in Corrosion Science ed. M. G. Fontana and R. W. Staehle, Vol. 3., Plenum Press, N.Y. 1973.
8. Metcut Report No. 1069-19640-2, February 1975, Cincinnati, Ohio.
9. F. Erdogan and G. C. Sih, *J. Bas. Engrg.*, 85 519 (1963).
10. D. F. Neal in "Forging and Properties of Aerospace Materials", Paper No. 10, University of Leeds Report, Jan. 1977.
11. F. W. Smith in "The Surface Crack: Physical Problems and Computational Solutions", ed. J. L. Swedlow, ASME 1972, p. 128.
12. G. R. Yoder, L. A. Cooley and T. W. Crooker, NRL Report 8048, Nov. 1976.
13. B. C. Odegard and A. W. Thompson, *Met. Trans.*, 5, 1207-1213 (1974).
14. R. M. Gilmore and N. A. Imam, to be published in *Met. Trans.*
15. D. N. Williams, *Met. Trans.*, 5, 2351-2358 (1974).
16. D. A. Meyn, *Met. Trans.*, 5, 2405-2414 (1974).
17. H. G. Nelson, A. S. Tetlman and D. P. Williams in "Corrosion Fatigue: Chemistry, Mechanics and Microstructure", National Association of Corrosion Engineers Vol. 2, 1971, p. 359.
18. Dell P. Williams and H. G. Nelson, *Met. Trans.*, 3, 2107-2113 (1972).
19. C. Hammond "Thin Foil Microscopy of Hydride - Titanium Alloys", Paper 38.1, TMS-AIME Fall Meeting, Niagara Falls, N.Y., Sept. 1976.

#### REFERENCES (Cont'd)

20. R. B. Sparks and J. R. Long, Report AFML-TR-301, 1974.
21. M. P. Smith, Pratt & Whitney Aircraft Report, February 1974.
22. Private Communication, Wyman-Gordon Co., 1974.
23. J. A. Hall, et. al., Mat. Sci. & Engr. 9, pp 197-210 (1972).
24. P. L. Reynolds, Evaluation of the Effects of Beta Flecks on LCF Life in PWA 1215, P&WA Report, April 1975.
25. S. Satta et. al., LCF of Ti-6Al-4V Forging, ASM Report D8-244, October 1968.
26. R. H. Jeal, Private Communication, 1976.
27. C. H. Wells and C. P. Sullivan, Trans. ASM, 62, 263-270 (1969).
28. E. Beck, Report AFML-TR-69-108, 1969.
29. W. P. Koster, N. Field and L. J. Fritz, Report AFML-TR-70-11, Matcut Research Associates, Inc., Cincinnati, Ohio (March, 1970).
30. S. Taira and Y. Murakani, Japan Soc. Mech. Engr. Bulletin, 4 (13), 41 (1961).
31. W. P. Evans and R. W. Buenacker, Trans AIME, 227, 447 (1965).
32. C. C. Wojcik and D. A. Koss, Materials Sci. Engr. 27, 97 (1977).
33. R. K. Steele and A. J. McEvily, Engr. Fract. Mech., 8, 31 (1976).
34. J. M. Finney, C. Laird and R. de la Vaux, Materials Sci. Engr. 24, 19 (1976).
35. Residual Stress Measurement by X-ray Diffraction - SAE J78A Second Edition, August 1971, Published by Society of Automotive Engineers, Inc., New York, N.Y.
36. B. Langer, PhD Thesis (1975) University of Connecticut, Storrs, Connecticut.